

**UCSF**

**UC San Francisco Electronic Theses and Dissertations**

**Title**

Mechanisms of Lysosome Mediated Immune Evasion and Regulatory Mechanisms of MHC-I in Pancreatic Ductal Adenocarcinoma

**Permalink**

<https://escholarship.org/uc/item/0mb76355>

**Author**

Venida, Anthony

**Publication Date**

2021

Peer reviewed|Thesis/dissertation

Mechanisms of Lysosome Mediated Immune Evasion and Regulatory Mechanisms of Major Histocompatibility Complex I in Pancreatic Ductal Adenocarcinoma

by  
Anthony Venida

DISSERTATION

Submitted in partial satisfaction of the requirements for degree of  
DOCTOR OF PHILOSOPHY

in

Biomedical Sciences

in the

GRADUATE DIVISION

of the

UNIVERSITY OF CALIFORNIA, SAN FRANCISCO

Approved:

DocuSigned by:

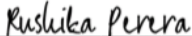


51C29AC261CD4F0...

Jayanta Debnath

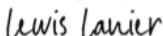
Chair

DocuSigned by:



Rushika Perera

DocuSigned by:



C111345FC07E42F...

Lewis Lanier

Committee Members

**Copyright 2021**

by

Anthony Venida

## Dedication

“If I have seen further, it is by standing on the shoulders of Giants.”

I dedicate this dissertation  
to all the Giants in my life  
that have illuminated a path forward  
in my journey towards Enlightenment.

This is for my mother, Maria Luisa Climacosa Venida,  
and father, Valentino Filler Venida,  
who sacrificed so much to get me here.

You gave me everything.

## Acknowledgements

It takes a village. I wouldn't be here without the support and guidance of all those that invested their time in my successes – and for that I am eternally grateful. If I have seen further than others, it is by standing upon the shoulders of giants. Completing a PhD became a dream once I started believing in my ability to overcome such a monumental challenge. It most certainly did not happen overnight. But rather, it was a gradual process brimmed with numerous failures and learned experiences guided by the giants in my life.

First and foremost, I would like to thank my thesis advisor, Rushika Perera, for her unwavering support throughout this PhD journey. It's not often you find an advisor that is wholly committed in the scientific and personal successes of her trainees that approaches her job as a mentor *and* friend with such fiery passion. I couldn't have asked for a better advisor to take me on this journey of becoming a competent scientist. She took a chance on a student that was interested in immunology and fully committed to learning a new field outside of her own expertise. Because of her guidance throughout these last five years, I have greater confidence in my ability to approach scientific questions with rigor and fearlessness and importantly, stronger belief in my capability to succeed as an academic. She believed in me when I struggled to see the potential in myself – and for that, I am filled with gratitude. I strive to be half the scientist and human being she is.

As junior members starting at UCSF, we both have seen each other grow as scientists and leaders. This transformative process has taught us to learn from our past experiences and adapt our expectations to become more inclusive mentors. Rushika has truly cultivated a dynamic and engaging group of scientists in her research group that I have been lucky to work with these last five years. I am especially thankful for Christina

Adams and Aprilgate Wang for welcoming me into the lab as a new graduate student and showing me the molecular biology ropes surrounding House Perera. Julian Yano deserves the next shoutout for being instrumental in driving our project forward and working countless hours as we went through the submission and revision process of our paper. To Grace Hernandez who has been a joy to work with from her time as a rotation student to now grad student extraordinaire, your dedication to science has reignited my excitement in tackling new questions in the field and reinforced my love for mentoring younger trainees. A huge kudos to the other research technicians that ran, currently run this lab: April, Julian, Denna Kwang, Jingjie Hu, and Alex Li – you all have such bright futures ahead of you and I cannot wait to follow you on your scientific and medical journeys. And of course, thank you to all Perera lab members for your continued support and help during graduate school: Suprit Gupta, Miru Ravichandran, Gilles Rademaker, Yang Yang, Jairo Barreto, Tom Ituarte, Zeynep Cakir, Annelot Staes, and Erica Sanchez.

I would like to thank members of the UCSF community outside of my lab home base for their continued support. To members of my thesis committee, Jayantha Debnath and Lewis Lanier; and additionally to members of my qualifying exam committee, Jeroen Roose, Jeoung-Sook Shin, and Matthew Spitzer – thank you for the valuable feedback and different perspectives offered during our one-on-one and group meetings as I navigated my research project. Thank you, Jay, for also serving as my academic advisor during my first two years and putting Rushika on my radar as I brainstormed ideas of which labs to rotate in as a first year. On top of breaking the news to me that I was accepted into the BMS program after I interviewed with you in 2016, you also brought Rushika and her work into my life. Thank you to the co-directors, program administrators,

managers, and financial analysts who make the BMS program run smoothly, especially Demian Sainz and Mark Ansel. Thank you to Erica Sanchez, Joseph Lin, and Leslie King who invited me to give research seminars and guest lectures at San Francisco State University, University of San Francisco, and Sonoma State University. These experiences were invaluable and reinforced my commitment to teaching the next generation of scientists. And of course, thank you to my BMS cohort for advice, venting sessions, listening to my practice talks, fantastic company, and unforgettable memories. I especially want to thank Alexis Krup, Austin Hsu, Kimberly Hoi, Kamir Hiam-Galvez, Didi Zhu, Elma Frias, Camille Simoneau, Katya Popova, Johnny Yu, Karen Wong, and Parinaz Fozouni.

Thank you to the teachers and advisors that believed in me from the start and provided me with invaluable opportunities to grow as a student and budding scientist. You believed in me when I did not believe in myself and gave me the confidence to reach outside my comfort zone. To my high school advisors, Marco Clark, Victor Shin, Richard Middleton, and Clare Treichel; to the Meyerhoff Scholars Program at the University of Maryland, Baltimore County (UMBC), Freeman Hrabowski, Keith Harmon, Lamont Toliver, Mitsue Wiggs, Erwin Cabrera, and Lydia Grmai; to my research advisors pre-graduate school Michael Lenardo, Kevin Hybiske, Alessio Fasano, and Andrea Meredith – thank you for giving me the tools, investing time in my success, and helping me navigate a career in academia as a first-generation student. You helped cultivate a mindset of beginning with the end in mind. Thank you to the Lenardo lab members at the NIH who continue to support my scientific endeavors, especially Carrie Lucas, Giulia Notarangelo, Heardley Moses Murdock, Sonia Majri, Tim Gilpatrick, Drew Comrie, and Jill Fritz. Without all of these wonderful individuals, I wouldn't be where I am today.

People think I am joking when I acknowledge my bikes getting me through graduate school, but it truly has been a godsend that has gotten me through dark and difficult times. My definition of what is possible in this world has expanded simply through the act of riding a bike. I learned how to channel grit, passion, and courage not just in racing and endurance events, but in many aspects of my life. And because of a life on two wheels, I met a wonderful community that continually supports me in all of my adventures. A special shoutout to the UCSF triathlon group, Fatcake Club, and the 4K for Cancer. First-year graduate student Anthony would have never believed he could complete double-centuries, swims from Alcatraz Island, ultramarathons, and Ironman-distanced races. They helped me reach outside of my comfort zone and expanded my definition of what is possible. My two bikes and two legs were the therapists I needed during graduate school that have opened the world up for me.

Most importantly, I have my family to thank for their steadfast support in all the ambitious goals and aspirations I strive toward. They are my biggest cheerleaders that have showered me with love indefinitely and my forever support system I can always rely on. Thank you to my grandparents for taking the leap of faith and immigrating to the United States, navigating a foreign world in order to provide opportunities for your children and grandchildren. I learned how to be a fighter from the two of you. Thank you to my aunts, uncles, and cousins, especially Myra, John, Veronica, Sunny, Mae, Bobby, and Caresse. I learned how to be a champion for others because of my time with you. To the ones that I am inextricably bound to by past, present, and future – I thank my parents for the greatest gifts I never asked for, but one that I hold dear to my existence: my sisters, Valerie and Marylou. I appreciate having the two of you as role models I can infallibly



count on. I learned how to love others and what I do because of you. And last but not least, to my mom and dad for the countless sacrifices and outpouring of love you have shown me these last three decades – words cannot describe how much gratitude I have for the two biggest role models of my life. I am incredibly grateful for having them in my life and am indebted to them for having such an impactful influence. I learned diligence, perseverance, and how to be selfless because of you.

It takes a village, and I've nothing else to say but thank you. I stand on the shoulders of Giants because of you, and I hope to be the shoulder for others as I continue on with this scientific journey. Your love and support mean the world to me.

## CONTRIBUTIONS

Yamamoto, K.\* , **Venida, A.\***, Yano, J., Biancur, D.E., Kakiuchi, M., Gupta, S., Sohn, A.P., Mukhopadhyay, S., Lin, E., Parker, S.J., Banh, R. S., Paulo, J.A., Wen, K. W., Debnath, J., Kim, G. E., Mancias, J.D., Fearon, D.T., Perera, R.#, Kimmelman, A.C.# Autophagy Facilitates Immune Evasion of Pancreatic Cancer by Downregulating MHC Class I. *Nature* **581**, 101-105 (2020).

Yamamoto, K.\* , **Venida, A.\***, Perera, R. M., Kimmelman, A. C. Selective Autophagy of MHC-I Promotes Immune Evasion in Pancreatic Cancer. *Autophagy* **16**(8), 1524-1525 (2020).

Allen, B. M., Hiam, K. J., Burnett, C. E., **Venida, A.**, DeBarge, R., Tenvooren, I., Marquez, D. M., Cho, N. W., Carmi, Y., Spitzer, M. H. Systemic dysfunction and plasticity of the immune macroenvironment in cancer models. *Nature Medicine* **26**(7): 1125-1134 (2020).

**Venida, A.** & Perera, R. Host Control of Tumor Feeding: Autophagy Holds the Key. *Cell Metabolism* **29**, 236- 238 (2019). PMID: 30726755.

The scientific and experimental ideas presented in this dissertation have been developed and written solely by me (Anthony Venida). The hypotheses and conclusions are based on extensive literature search and valuable discussions with Dr. Perera. During the past two and a half years in the Perera lab, initial experiments were designed and conducted independently by me. The experimental design for the dissertation project was discussed

and critically evaluated by my dissertation committee (Dr. Jayanta Debnath [Chair], Dr. Lewis Lanier, and Dr. Rushika Perera [thesis advisor]). In chapter two, I received additional mentorship and guidance through bi-monthly meetings with Alec Kimmelman and Keisuke Yamamoto at New York University Langone Health. In chapter three, I received scientific direction and help from Luke Gilbert and Thomas O'Loughlin at the UCSF Helen Diller Cancer Center. I wrote the preliminary drafts of the dissertation independently and received valuable feedback from Drs. Perera, Debnath, and Lanier as to the relevance of ideas and completeness of scientific rationale.

I performed all experiments and analysis of data that is described in this proposal. I was responsible for interpreting results and conclusions and importantly, wrote the first drafts of the second follow-up manuscript to my co-first author *Nature* paper. Dr. Perera will make final manuscript edits with input from collaborators. My dissertation committee and Dr. Perera were a beneficial source of feedback and constructive criticism as the project progressed.

Hold fast to dreams  
For if dreams die  
Life is a broken-winged bird  
That cannot fly.

Hold fast to dreams  
For when dreams go  
Life is a barren field  
Frozen with snow.

Langston Hughes

*Focus. Focus. Focus.*

**Mechanisms of Lysosome Mediated Immune Evasion and Regulatory  
Mechanisms of Major Histocompatibility Complex Class I in Pancreatic Ductal**

**Adenocarcinoma**

Anthony Venida

**ABSTRACT**

Pancreatic ductal adenocarcinoma (PDAC), a malignancy refractory to most therapies including immune checkpoint blockade (ICB) therapy, utilizes diverse mechanisms to evade immune clearance. One mechanism involves reduced presentation of tumor specific antigens by Major Histocompatibility Complex Class I (MHC-I) to immune cells. Many cancers alter MHC-I expression via genetic or epigenetic silencing; however, changes in MHC-I trafficking can also profoundly influence antigen presentation at the cell surface and is a previously underappreciated mechanism of MHC-I regulation in cancer.

My dissertation uncovers a role for enhanced autophagy and lysosome function in immune evasion through selective targeting of MHC-I molecules for degradation. Prior studies have shown that highly aggressive PDAC cells and tumors upregulate autophagy, an evolutionarily conserved self-recycling pathway that is hijacked by cancer cells to sustain metabolic fitness. In addition to the metabolic benefits tumor cells receive, autophagy and lysosomal activity have utilized these processes to gain a growth advantage by facilitating degradation and recycling of diverse intracellular materials. My data demonstrate that MHC-I molecules are selectively targeted for lysosomal degradation through an autophagy-dependent mechanism that involves the autophagy cargo receptor NBR1. PDAC cells display reduced MHC-I cell surface expression and

instead demonstrate predominant localization within autophagosomes and lysosomes. Notably, autophagy inhibition restores cell surface MHC-I expression, enhances anti-tumor CD8<sup>+</sup> T cell responses *in vitro* and *in vivo*, and importantly, sensitizes PDAC tumors to dual immune checkpoint blockade (ICB). Our data on immune evasion add to the growing list of cell-autonomous functions of the autophagy and lysosome system in supporting PDAC tumorigenesis.

To identify the distinct molecular mechanisms of MHC-I regulation in PDAC, we combined a whole-genome CRISPRi screen and Turbo-ID proximity-dependent proteomics to determine regulators and interactors of MHC-I, respectively. From these two datasets, 101 overlapping candidates were identified, many of which were related to post-translational modification (PTM), trafficking machinery, and kinase regulation. The gene candidates likely control MHC-I by diverting plasma membrane localization to degradative organelles. Several gene candidates associated with E3 ubiquitin ligase and kinase signaling were validated and show increased plasma membrane when knocked down or pharmacologically inhibited. Using these two datasets as a resource of MHC-I regulation can help identify PDAC-specific mechanisms that facilitate altered trafficking of MHC-I. Findings from this study will lead to a better understanding of PDA pathophysiology and have the potential to inform the development of rational combination therapies that restore MHC-I cell surface localization, thereby rendering PDA cells more susceptible to immunotherapy. In particular, results from this research project will help to determine the causes of aberrant intracellular localization of MHC-I and can help explain how MHC-I is unable to traffic normally. These studies also lay the foundation for mechanisms of immune evasion in other aggressive cancers.

## Table of Contents

|   |    |
|---|----|
| <b>Chapter 1: Introduction</b> .....  | 1  |
| Classical Features of Pancreatic Ductal Adenocarcinoma .....                | 2  |
| Cellular Metabolism: Autophagy and Lysosome function in PDAC .....          | 5  |
| Overview of the Autophagy Process .....                                     | 5  |
| The Role of Autophagy in in PDAC Metabolism: Host and Tumor Cell            |    |
| Autophagy Influence Tumor Growth.....                                       | 7  |
| The Importance of Lysosomal Catabolism in PDAC .....                        | 9  |
| Increased Lysosomal Biogenesis and Activation in PDAC .....                 | 9  |
| Targeted Protein Degradation in PDAC Lysosomes.....                         | 11 |
| Immunosuppressive Mechanisms and Tumor Microenvironment in PDAC .....       | 12 |
| General Mechanisms of Immune Evasion in Cancer .....                        | 12 |
| Cell intrinsic and tumor microenvironmental mechanisms that lead to an      |    |
| immunosuppressive PDAC landscape .....                                      | 13 |
| The Effect of Autophagy on Tumor Immunity .....                             | 15 |
| Focus of Dissertation: Mechanisms of Lysosome Mediated Immune Evasion       |    |
| and Regulatory Mechanisms of MHC-I in PDAC .....                            | 17 |
| Figures .....   | 18 |
| <b>Chapter 2: Autophagy Promotes Immune Evasion by Downregulating MHC-I</b> |    |
| <b>in Pancreatic Cancer</b> .....   | 35 |
| Abstract.....   | 36 |

|  |            |
|--|------------|
| Background .....   | 37         |
| Results .....  | 38         |
| MHC-I is enriched in lysosomes of PDAC cells and displays reduced<br>cell surface expression .....                               | 38         |
| Autophagy inhibition increases the levels and plasma localization of MHC-I .....   | 39         |
| NBR1 mediates selective autophagy of MHC-I .....   | 40         |
| Autophagy inhibition enhances anti-tumor immunity .....  | 41         |
| Basal autophagy flux levels determine immunogenicity of PDAC cells .....   | 45         |
| Autophagy inhibition sensitizes PDAC to dual ICB .....   | 46         |
| Discussion .....   | 48         |
| Figures .....  | 51         |
| Materials and Methods .....  | 77         |
| References .....   | 95         |
| <b>Chapter 3: Identifying Novel Regulators of MHC-I in Pancreatic Cancer .....</b>   | <b>104</b> |
| Abstract .....   | 105        |
| Background .....   | 106        |
| Results .....  | 108        |
| Whole genome CRISPRi screen identifies novel regulators of MHC-I<br>in PDAC .....  | 108        |
| Discovery of novel regulators of MHC-I in PDAC using proximity dependent<br>biotinylation proteomics and CRISPRi screening ..... | 110        |
| E3 ubiquitin ligase HERC4 mediates MHC-I plasma membrane expression .....  | 112        |



|                            |     |
|----------------------------|-----|
| Discussion.....            | 114 |
| Figures .....              | 119 |
| Materials and Methods..... | 125 |
| References.....            | 132 |

## List of Figures

|  |    |
|--|----|
| Figure 1.1. Characteristic features and the tumor evolution of pancreatic ductal adenocarcinoma .....                                    | 19 |
| Figure 1.2. Lysosomal degradation pathways and reliance on the MiT/TFE factors for PDAC tumor growth .....                               | 20 |
| Figure 1.3. Effects of autophagy inhibition in host-tumor cell interactions.....   | 21 |
| Figure 2.1. MHC-I is enriched in lysosomes of PDAC cells and displays reduced cell surface expression.....                               | 51 |
| Figure 2.2. NBR1 promotes MHC-I trafficking to the lysosome through an autophagy-dependent pathway .....                                 | 52 |
| Figure 2.3. Autophagy inhibition enhances anti-tumor T cell response.....  | 54 |
| Figure 2.4. Autophagy inhibition sensitizes PDAC to dual ICB .....   | 56 |
| Extended Data Figure 2.1e. Heterogeneous distribution of MHC-I in KRAS-mutant cancers .....  | 58 |
| Extended Data Figure 2.2e. Inhibition of autophagy and lysosomes restores MHC-I levels and plasma membrane localization.....             | 61 |
| Extended Data Figure 2.3e. Inhibition of macroautophagy, but not LAP/LANDO, restores MHC-I levels .....                                  | 62 |
| Extended Data Figure 2.4e. The UBA domain of NBR1 is required for interaction with MHC-I.....  | 63 |
| Extended Data Figure 2.5e. Autophagy inhibition restores MHC-I expression, leading to enhanced anti-tumor T cell response in vitro ..... | 65 |
| Extended Data Figure 2.6e. Autophagy inhibition modulates anti-tumor immunity  |    |

|   |     |
|---|-----|
| in both orthotopic and liver metastasis .....   | 68  |
| Extended Data Figure 2.7e. Tumor regression after autophagy inhibition is rescued<br>by depletion of CD8+ T cells or ablation of cell surface MHC-I ..... | 70  |
| Extended Data Figure 2.8e. Separation of PDAC cells with distinct autophagy flux<br>using the GFP-LC3-RFP reporter.....                                   | 71  |
| Extended Data Figure 2.9e. Basal autophagy flux determines immunogenicity of<br>PDAC cells .....  | 73  |
| Extended Data Figure 2.10e. Autophagy inhibition synergizes with dual ICB.....  | 76  |
| Figure 3.1. Whole genome CRISPRi screen to identify novel regulators of MHC-I<br>in PDAC.....   | 120 |
| Figure 3.2. Proximity dependent biotinylation proteomics combined with CRISPRi<br>screening to identify novel regulators of MHC-I in PDAC.....            | 121 |
| Figure 3.3. Inhibition of the MAPK signaling pathway restores surface expression<br>of MHC-I 24 hours post-treatment.....                                 | 122 |
| Figure 3.4. E3 ubiquitin ligase HERC4 is overexpressed in PDAC and mediates<br>plasma membrane expression of MHC-I.....                                   | 123 |
| Extended Figure 3.1e. Cell sorting procedure and layout for whole genome<br>CRISPRi screen in dCas8902 PDAC cells.....                                    | 124 |

## **Chapter 1: Introduction**

## **Pancreatic Ductal Adenocarcinoma**

Pancreatic ductal adenocarcinoma (PDAC), the most common cancer of the pancreas, is among the most lethal of cancers with approximately 60,000 patients diagnosed yearly. Despite significant progress understanding the initiation, disease progression, and pathology of this disease, the 5-year survival remains at 10% (Siegel et al., 2021; Rahib et al., 2021). Several unique features of PDAC, including near universal activating mutations in the Kras oncogene, rewired cellular metabolism, and a tumor suppressive microenvironment, contribute to its aggressive nature and reduced response to chemotherapy and immunotherapy (O'Reilly et al., 2019; Ying et al., 2016; Jones et al., 2008; Bardeesy et al., 2002). A better understanding of PDAC pathophysiology and the underlying molecular properties that make this an aggressive cancer is necessary to inform the development of therapeutics and new treatments.

### **Classical Features of Pancreatic Ductal Adenocarcinoma**

A three-tier classification of well-defined microscopic precursor lesions termed pancreatic intraepithelial neoplasia (PanIN) characterizes the evolution of normal pancreatic epithelium to fully transformed PDAC (Figure 1.1a). This step-wise development of low-grade PanIN-1 and PanIN-2 to high grade PanIN-3 are associated with genetic and histologic progression (Ryan et al., 2014). In postmortem examinations of PDAC patients, low-grade PanIN-1 are readily detectable in non-diseased pancreas, whereas higher grade PanIN lesions are characteristically detected next to established adenocarcinomas or in regions of non-tumor bearing pancreas from patients that have familial predisposition to the disease (Canto et al., 2012). Greater than 90% of patients acquire activating mutations in the KRAS oncogene that drive malignant transformation and progression

from PanIN to PDAC and eventual metastasis (Figure 1.1b). As tumor formation progresses, deletion and mutational inactivation of TP53, CDKN2A, and SMAD family member 4 (SMAD4) tumor suppressors are detected with greater incidence in PanIN-2 and PanIN-3 lesions, supporting a genetic progression of pancreatic oncogenesis driven by KRAS mutations (Yachida and Iacobuzio-Donahue, 2013). In both genetically engineered mouse (GEM) models and human PDAC cell lines, elimination of mutant KRAS results in arrested proliferation and cell death. Tumor regression in GEM models are observed, highlighting KRAS as the subject of many preclinical trials and investigations (Ying et al., 2012; Singh et al., 2009).

Developing a clinical drug targeting oncogenic KRAS has historically remained elusive, but novel approaches to drug discovery and advances in technology recently have been successful at blocking oncogenic signaling using small molecules. FDA approval of the first-in-class KRAS-G12C inhibitor for non-small-cell lung cancer (NSCLC) in 2021 marks a major milestone in targeted therapies for patients with KRAS mutations (Dafna Bar-Sagi et al., 2020; Ostrem et al., 2013). Though recent advances in the development of KRAS inhibitors have made their way to the clinic for lung cancer, therapies for PDAC patients remain overwhelmingly low since KRAS-G12C mutations are rare. 90% of PDAC patients primarily harbor KRAS G12D and KRAS G12V mutations that are difficult to target due to the chemical intractability of the protein, with chemistries much different than KRAS-G12C (Nagasaka et al., 2021). Uncovering additional targetable vulnerabilities of PDAC cells is necessary to address this unmet need.

Several studies that link rewiring of metabolic pathways downstream of oncogenic KRAS with increased tumor growth have led to new insights into PDAC cellular metabolism

(Kimmelman, 2015). Activation of these pathways may be linked to the complex tumor microenvironment characterized by a dense stromal compartment, low microvascular density, and intratumoral hypoxia (Neesse et al., 2011; Dias Carvalho et al., 2017; Encarnacion-Rosado and Kimmelman 2021) (Figure 1.1c). PDAC cells secrete a number of growth factors, such as fibroblast growth factor 2 and transforming growth factor beta 1 (TGF $\beta$ 1), that promote collagen synthesis and activation of cancer-associated fibroblasts, namely pancreatic stellate cells (PSC). The stroma consists of PSCs, extracellular matrix components, and hyaluronic acid that can positively and negatively contribute to the growth and survival of tumor cells (Neesse et al., 2013; Weniger et al., 2018).

Additionally, multiple types of inflammatory cells – including macrophages, plasma cells, mast cells, and lymphocytes – contribute to the anti-tumor immune landscape of pancreatic cancer (Figure 1.1c). The immunosuppressive inflammatory program from these immune cells support tumorigenesis through paracrine cross-talk with tumor cells (Vonderheide and Bayne, 2013). The heterogeneous infiltrate of stromal cells and inflammatory immune cells co-evolves with the reprogramming of pancreatic epithelial cells as they undergo transformation during Pan-IN formation and disease progression (Hingorani, 2014; Lee, Perera et al., 2014; Ozdemir et al., 2014; Rhim et al., 2014). For example, immunosuppressive regulatory T cells and Gr1+CD11b+ myeloid cells are recruited to the stroma during the early stages of tumor formation, blocking T-cell-mediated anti-tumor immunity. Tumor cells produce cytokines such as granulocyte-macrophage colony-stimulating factor to recruit these immunosuppressive cells (Pylyayeva-Gupta et al., 2012). The microenvironment of PDAC plays a complex role in

promoting tumor growth and metastasis and concurrently, can serve as a physical barrier to therapeutic delivery (Feig et al., 2012).

Rewiring of PDAC cell metabolism and the establishment of an immunosuppressive microenvironment throughout tumorigenesis contribute to the complex biology and therapeutic resistance of this deadly tumor. Understanding how these cancer cells function at a mechanistic level will provide insight into its pathogenesis and shed light on how it affects other cells in the tumor microenvironment. This dissertation aims to address tumor cell intrinsic properties of PDAC cells that allow them to evade an immune response, thrive in the tumor microenvironment, and become resistant to conventional therapies.

## **Cellular Metabolism: Autophagy and Lysosome function in PDAC**

### **Overview of the Autophagy Process**

Macroautophagy (herein referred to as autophagy) is an evolutionarily conserved mechanism used by cells to maintain homeostasis. This is a tightly regulated process that relies on cellular machinery (briefly reviewed below) to maintain normal proteostasis by turning over superfluous macromolecules, damaged organelles, and aged proteins that are targeted to the lysosome for degradation. In normal cell homeostasis, catabolism of cytoplasmic constituents via autophagy is important for proliferative, developmental, and inflammatory signals that can alter cell state (Kimmelman 2011). Additionally, products generated following degradation of these substrates can be recycled for use in energy production and other biosynthetic reactions important for tissue homeostasis and cellular quality control (Levine and Kroemer 2008; Mizushima et al., 2008). When it was first discovered over 50 years ago, autophagy was initially thought to be a nonspecific bulk



degradation process (De Duve and Wattiaux 1966), but recent work has shown that specificity of individual cargos via the engagement of autophagic cargo receptors is also possible (Zaffagnini and Martens 2016).

During the process of autophagy, a double-membrane vesicle, called the autophagosome, encapsulates cytoplasmic content, such as protein aggregates or damaged cellular organelles. Autophagosomes rely on trafficking machinery to fuse with lysosomes to degrade cargo material (He and Klionsky, 2009; Mizushima et al., 2008). Work done by many groups have established at least seven steps in the autophagic pathway, with conserved autophagy genes (ATG genes) promoting the first five steps, while other endosomal genes common to lysosomal pathways regulating the last two steps. In step one, the Unc-51-Like Kinase (ULK) protein kinase complex regulates initiation of autophagic vesicle (AV) formation (Kumar et al., 2019). Once the ULK complex is activated, the VPS34 lipid kinase complex prepares the membrane for curvature during step two by forming phosphatidylinositol 3-phosphate (PI3P) on membranes (Behrends C et al., 2010). During step three, the lipid phosphatidylethanolamine (PE) is conjugated to LC3 protein family members attached to AV membranes through a complex ubiquitin-like conjugation system (Walczak et al. 2013; Ichimura et al., 2000). In step four, docking sites on LC3 serve as regions where autophagy receptors can bring their cargo to the AVs. These cargo receptors help provide selectivity to the autophagic process by allowing substrates to preferentially bind to specific receptors (Gatica et al., 2018). Step five involves maturation of the AV followed by AV-lysosome fusion (Shibutani and Yoshimori, 2014; Nakamura and Yoshimori, 2017).

In the final step, autophagic cargo are degraded in the lysosome, with recycled contents exiting via transporters to fuel cell growth (Kimmelman and White, 2017).

In the context of cancer biology, autophagy has been shown to play dual roles in both tumor promotion and suppression, regulating proliferation and the development of cancer cells (Rao et al., 2014). Dysregulated expression of the autophagic machinery components and autophagy cargo receptors in both tumor and non-tumor cells have been linked to carcinogenesis and tumor maintenance (Amaravadi et al. 2019). Importantly, activation of cytoprotective autophagy has been observed after cancer therapy administration (Rebecca and Amaravadi 2016). Understanding the distinct molecular mechanisms of autophagy regulation in tumors will aid in the development of novel therapies and strategies to treat cancer patients.

### **The Role of Autophagy in in PDAC Metabolism: Host and Tumor Cell Autophagy Influence Tumor Growth**

PDAC cells are characterized by aberrant upregulation of several cellular trafficking pathways, such as macropinocytosis and autophagy, that help to sustain metabolic homeostasis and cellular fitness (Figure 1.2a). As discussed above, autophagy is a regulated catabolic pathway that degrades and recycles cellular organelles and macromolecules, whereas macropinocytosis is an endocytic pathway that non-specifically uptakes extracellular material. Both of these pathways converge on the lysosome, an acidic organelle in the cell that contains many digestive enzymes, which degrades incoming cargo material and facilitates recycling of digestion products back to the cytoplasm (Davidson and Vander Heiden, 2017; Perera and Zoncu, 2016). Several studies have established autophagy and lysosome activity as essential for maintenance

of metabolic homeostasis and tumor growth in PDAC cells (Yang et al., 2011, 2014; Perera et al., 2015).

During the earliest stages of tumorigenesis, autophagy has been shown to limit growth (Qu et al., 2003; Yang et al., 2011; Kimmelman 2011); however, several groups have established that the process of autophagy favors tumor progression by allowing the cells to cope with environmental and intracellular stresses, such as nutrient shortage and hypoxia (Amaravadi et al., 2019). In the latter context, autophagy inhibition has been shown to improve therapeutic outcomes for advanced cancer patients. In a *Kras*-driven *Trp53*<sup>+/-</sup> pancreatic cancer model, autophagy inhibition via *Atg5* deletion impaired premalignant lesion progression to invasive cancer. In the context of wild-type *Kras* mice, *Atg5* deletion in the pancreas did not lead to tumorigenesis (Yang et al., 2014).

More recent studies focusing on the effects of genetic autophagy inhibition in both host and tumor cells have been investigated using more complex mouse models. Acute, systemic deletion of mouse *Atg7* in both host and tumor cells of RAS-driven cancers induced greater regression than autophagy deleted only in tumor cells (Yang et al., 2018; Karsli-Uzunbas et al., 2014). Results of these studies suggest a role for host autophagy in promoting tumor growth. Consistent with this idea, in a model of mutant *Kras*-driven PDAC, pancreatic cancer relies on support from the stromal compartment to support tumor growth. Pancreatic stellate cells utilize autophagy to secrete alanine, a non-essential amino acid, that is taken up by tumor cells and used to fuel mitochondrial metabolism (Sousa et al., 2016). Tumor dependence on exogenous alanine fuels the tricarboxylic acid (TCA) cycle and shifts dependency away from glucose and serum-derived nutrients, which are limited in the pancreatic tumor microenvironment. The

cooperative metabolic needs between pancreatic stellate cells and cancer cells highlights the essential role of metabolic scavenging in PDAC and reliance on tumor cell intrinsic and extrinsic autophagy.

Under acute inhibition, where autophagy can be regulated temporally and spatially in *Kras*-driven PDAC mouse models, tumor regression was significantly promoted (Yang et al., 2018). The Kimmelman lab developed a mouse model using a dominant negative *Atg4b* mutant under the control of a tetracycline-inducible promoter, allowing autophagy to be finely tuned in both host and tumor cells. Their model allows for the acute and reversible inhibition of autophagy, similar to drug therapy. In an autochthonous mouse model of PDAC, tumor regression was observed even under intermittent autophagy inhibition, suggesting that anti-autophagy therapies may not need to be continuously given in the clinic. This study emphasizes the contribution of autophagy in both tumor cell-intrinsic and host - tumor cell-extrinsic mechanisms that contribute to tumor maintenance. Importantly, results from these studies can direct ongoing clinical trials and aid in drug-development initiatives.

## **The Importance of Lysosomal Catabolism in PDAC**

### *Increased Lysosomal Biogenesis and Activation in PDAC*

Pancreatic tumors must deal with severe metabolic stress in a hypovascular and hypoxic microenvironment by upregulating endocytic and scavenging pathways that converge on the lysosome (Perera and Bardeesy, 2015; Bardeesy and DePinho, 2002). Induction of the MiT/TFE transcription factors (MITF, TFE3, and TFEB) coordinate nutrient scavenging, lysosome biogenesis, and lysosomal function to drive PDAC pathogenesis by recycling building blocks necessary for the production of new metabolites,

maintenance of energy homeostasis, and support of macromolecule synthesis (Perera et al., 2015). In human PDAC cells, the MiT/TFE proteins are constitutively localized to the nucleus, driving expression of lysosomal catabolic and autophagic genes that are essential for tumor growth. Inactivation of these transcription factors leads to defective lysosomal function, downregulation of lysosome and autophagy genes, and dysregulated autophagic flux and degradation of proteins via macropinocytosis. Importantly, knockdown of MiT/TFE factors *in vitro* and in *in vivo* PDAC mouse xenograft models impair cellular proliferation and tumor growth, respectively (Perera et al., 2015) (Figure 1.2c-d). Regulation of lysosomal function allows for the fine-tuning of metabolic processes that allow these tumor cells to survive in an austere tumor microenvironment.

Building on the discovery that lysosomes serve as a regulatory hub for cellular processes critical for the course of tumor progression (Perera and Zoncu, 2016), studying lysosomal biology and how this degradative organelle shapes tumor cell fitness will be important to identify tumor cell vulnerabilities. In addition to serving as an organelle critically important for macromolecular recycling, the lysosome functions as an important node for metabolic reprogramming, pro-growth signaling, and vesicle trafficking (Lawrence and Zoncu 2019). Transmission electron microscopy show a 12-fold increase in lysosomal biogenesis in treatment-naïve PDAC specimens compared to normal pancreatic tissue (Perera et al., 2015) (Figure 1.2b). The marked increase in autophagy function and lysosome number provides new metabolites and energy to support macromolecule synthesis necessary for cellular function. Metabolomic studies revealed that the use of lysosome inhibitors or knockdown of the MiT/TFE proteins – master transcriptional regulators of lysosome gene expression (Martina et al., 2014; Rocznik-Ferguson et al., 2012; Settembre et al., 2012,

2011; Haq et al., 2011; Sardiello et al., 2009) - displayed a significant decrease in intracellular levels of amino acids, indicating PDA-specific functions in maintaining amino acid stores via lysosome activation (Perera et al., 2015).

#### *Targeted Protein Degradation in PDAC Lysosomes*

An equally important adaptation cancer cells utilize is the selective removal of targeted proteins via lysosomal degradation pathways to remodel the cellular proteome. Recent studies have shown that specific cargo can be targeted for degradation via sequestration within autophagosomes in a process called selective autophagy (Mancias et al., 2014; Mathew et al., 2014; Amaravadi et al., 2019). Additionally, autophagy ensures improved tumor cell function and can influence malignant progression by clearance of misfolded proteins in response to ER stress and removal of damaged organelles (Tameire et al., 2015; Rao et al., 2014). Metabolically recycling building blocks and transforming the proteomic landscape contributes to the aberrant features of PDAC and confers a survival advantage to the tumor.

In addition to a significant increase in the number of lysosomes in PDAC cells, qualitative differences between non-transformed and tumor lysosomes endow pro-oncogenic properties to cancer cells at a functional and structural level (Yamamoto and Venida et al., 2020; Gupta et al., 2021). Recent work from the Perera lab utilized a method to rapidly purify intact lysosomes from cells utilizing lysosome specific membrane tags (Zoncu et al., 2011) to study the differences between lysosomes in non-transformed control cells versus PDAC cells. Profiling of immuno-isolated lysosomes captured from PDAC and non-PDAC cells via mass spectrometry-based proteomic analysis identified key differences in the lysosomal elutes between control and PDAC cells. Consistent with

increased rates of vesicular trafficking to the lysosome and increased rates of autophagy in PDAC, gene ontology enrichment analysis revealed metabolism, cell adhesion, vesicle-mediated trafficking, and endocytosis as enriched biological processes. Furthermore, autophagy-related proteins, such as LC3B and GABARAP2, and autophagy receptors, such as NBR1, SEC62, and SQSTM1, were enriched in lysosomal PDAC elutes (Gupta et al., 2021). This highlights the importance of studying lysosomes as it can inform the biology of pancreatic cancer.

## **Immunosuppressive Mechanisms and Tumor Microenvironment in PDAC**

### **General Mechanisms of Immune Evasion in Cancer**

One of the major hallmarks of cancer includes the role of the immune system as regulators of tumor development and progression (Hanahan and Weinberg, 2011). Tumor cells have evolved numerous strategies to avoid immune recognition, allowing these cells to bypass clearance and proliferate at an undivided rate. One such strategy includes downregulation of pathways involved in antigen presentation, such as dysregulation of the major histocompatibility complex-I (MHC-I) proteins and transporter associated with antigen processing protein (TAP) (Garrido et al., 1997; Hicklin et al., 1999; Johnsen et al., 1999). Loss of tumor antigen recognition by effector T-cells has also been observed as a result of genetic instability and constant cell division. Cells that have lost the ability to present neoantigens undergo positive selection in a process termed “cancer immunoediting” (Dunn et al., 2002). Another strategy utilized by tumor cells and cells of the tumor microenvironment to induce an immune privilege state includes secretion of immunosuppressive molecules and/or modulation of immunoregulatory molecule expression. The secretion of immunosuppressive cytokines, such as IL-6, IL-10, TGF $\beta$ ,

TNF $\alpha$ , or VEGF, have been linked to tumor development and progression (Lind et al., 2004; Lin et al., 2002; Fisher et al., 2014; Matsuda et al., 1994). Immunoregulatory molecules, such as immune checkpoint regulators of the B7 family (PD1, PDL1, B7-1, B7-2, CTLA4), are overexpressed in cancer to induce T cell anergy (Ribas and Wolchok 2018).

The establishment of an immunosuppressive tumor microenvironment is orchestrated by the two major mechanisms listed above – i) inhibition of anti-tumor immune cells such as CD4<sup>+</sup> cells, CD8<sup>+</sup> cells, natural killer (NK) cells; and ii) activation and recruitment of immunosuppressive cells such as regulatory T cells (Tregs), myeloid-derived suppressor cells (MDSCs), and anti-inflammatory macrophages (M2) (Gonzalez et al., 2018; Galon and Bruni 2020). While lysosomal function has been shown to contribute to PDAC cellular fitness, the poor antigenic and immunogenic landscape also plays a critical role in evading an immune response in pancreatic cancer.

### **Cell intrinsic and tumor microenvironmental mechanisms that lead to an immunosuppressive PDAC landscape**

PDAC remains one of the most immune-resistant tumor types, making this cancer incredibly difficult to treat. While surgery and adjuvant chemotherapy can achieve long-term survival, only a small minority of patients with resectable tumors respond (Conroy et al., 2018). Unfortunately, PDAC is almost completely refractory to FDA-approved immunotherapies, with the exception of microsatellite instability (MSI) high tumors that comprise <1% of patients. A large part of this insensitivity to therapy is evasion of host immunity via cell-intrinsic mechanisms and cell-extrinsic factors from the tumor microenvironment. There is increasing evidence that mutant KRAS drives



immunosuppressive mechanisms within the tumor microenvironment in addition to its canonical oncogenic role (Collins et al., 2012). Mutant KRAS prevents both innate and adaptive anti-tumor immune responses by several mechanisms such as regulating expression of checkpoint molecules, such as CD47 and PDL1, (Casey et al., 2016; Coelho et al., 2017) and establishing a desmoplastic microenvironment, activated stromal cells, and suppressive immune cells through a paracrine network (Dias Carvalho et al., 2018). In mouse models of pancreatic cancer, several groups have shown that tumor microenvironment evolution precedes invasive cancer formation. For example, PanIN lesions in  $Kras^{LSL.G12D/+}; Pdx-1-Cre$  (KC) mice are infiltrated by myeloid-derived suppressor cells (MDSCs), regulatory T cells (Treg), and immunosuppressive tumor-associated macrophages (TAMs) (Clark et al., 2007). Additionally, as PanINs progress to later stage and higher-grade lesions, type I conventional dendritic cells (cDC1) that are important for priming  $T_{effector}$  cells progressively become dysregulated and decrease in number (Hegde et al., 2020).

Another factor that has been shown to determine immune reactivity in cancer is overall antigenic strength. In the spontaneous  $Kras^{LSL.G12D/+}; Trp53^{R172H/+}; Pdx-1-Cre$  (KPC) mouse model, the features of immune editing and immunosurveillance are not observed in the absence of strong antigens expressed by tumor cells (Evans et al., 2016). This result can be reversed by engineering tumor cells to express a strong, foreign antigen leading to tumor rejection and T cell memory, even without the use of immune checkpoint blockade. In human PDAC tumors, several groups have shown that prediction of immunogenicity via neoantigen quality metrics correlate with patient survival (Richman et al., 2019; Balachandran et al., 2017). Several studies indicate that an immune response

in PDAC can be harnessed to generate functional anti-tumor T cells despite decreased antigenicity, suggesting other mechanisms that likely contribute to the non-immunogenic, “cold” tumor of pancreatic cancer (Schmitz-Winnenthal et al., 2005; Bear et al., 2020).

### **The Effect of Autophagy on Tumor Immunity**

Autophagy can either promote or suppress cancer development depending on the cell, tissue type, and stage of tumor. Several studies have shown that autophagy can modulate the functions of immune cells and production of cytokines (Guan-Min Jiang et al. Mol Cancer 2019). Evidence in favor of an anti-tumorigenic role of autophagy has been described in systemic immunity and hematopoiesis. In apoptotic tumor cells, autophagy has been reported to be necessary for immunogenic cell death and recognition by the immune system (Michaud et al., 2011). Additionally, autophagy has been shown to be important in priming tumor-specific CD8<sup>+</sup> T cells and essential in activation of effector and memory T-cells (Uhl et al., 2009; Xu et al., 2014). Finally, autophagy has been shown to support improved tumor immune responses by stimulating tumor antigen cross-presentation in highly context-dependent circumstances (Li et al., 2012).

However, activation of autophagy has also been associated with tumor-protective roles in cancer immunity (Figure 1.3). In melanoma, upregulation of autophagy in tumor cells due to a hypoxic tumor microenvironment limited cell death induced by immune cells. Upon treatment with hydroxychloroquine, a lysosomal inhibitor, T-cell killing was enhanced (Noman et al., 2011). Additionally, genetic or pharmacological inhibition of components of the autophagy cascade has been shown to augment antitumor immunity. Genetic inhibition of BECN1 in cancer enhances infiltration of T cells and NK cells into the immune microenvironment (Mgurditchian et al., 2017). Inhibiting autophagy in

pancreatic tumors in the dominant-negative *Atg4b* mouse model revealed an influx of antitumor macrophages (Yang et al., 2018). In support of the previous finding, the use of chloroquine derivatives to inhibit lysosomal function has been shown to enhance antitumor immunity by switching macrophage polarization from M2 to M1, enabling an effective cytotoxic T cell response in the tumor (Chen et al., 2018; Frazier et al., 2017).

In the context of the adaptive immune response, autophagy can attenuate the activity of CD8<sup>+</sup> T cells and NK cells. Lysosomal activity limited the anticancer effectiveness of CD8<sup>+</sup> T cells in melanoma (Khazen et al., 2016). Additionally, inactivation of T cell autophagy via *Atg5* or *Atg7* deletion resulted in enhanced tumor rejection in syngeneic mouse models of breast and prostate cancer (DeVorkin et al., 2019). In T-cell mediated immunity, elimination of target cells can only occur when they recognize tumor specific antigens present on MHC-I, the primary receptor for antigen presentation to CD8<sup>+</sup> T cells. Intriguingly, upregulation of tumor specific autophagy and lysosome gene signatures was found to correlate with reduced CD8<sup>+</sup> T cell infiltration (Balachandran et al., 2017; Li et al., 2018). Additionally, autophagy-related genes are enriched in a subset of liver metastases that have reduced expression of MHC-I (Pommier et al., 2018; Chang and Campoli, 2005). In PDAC, mutations causing MHC-I are rarely found despite the frequent downregulation of MHC-I expression. Therefore, tumor cells likely evolve different mechanisms to regulate MHC-I in order to reduce antigen presentation and promote immune evasion (Waddell et al., 2015; Pommier et al., 2018; Ryschich et al., 2005; Pandha et al., 2007).

## **Focus of Dissertation: Mechanisms of Lysosome Mediated Immune Evasion and Regulatory Mechanisms of MHC-I in PDAC**

My dissertation focuses on addressing a critical gap linking a direct role for autophagy and the lysosome in modulating MHC-I and antigen presentation as a way of facilitating immune evasion in pancreatic cancer. In chapter two, I present data that uncover a role for enhanced autophagy and lysosome function in anti-tumor immunity by selectively targeting MHC-I molecules for degradation. PDA cells display reduced MHC-I cell surface expression and instead, demonstrate predominant localization within autophagosomes and lysosomes. Notably, autophagy inhibition restores surface MHC-I levels, leading to improved antigen presentation, enhanced anti-tumor T cell response, and reduced tumor growth in syngeneic hosts. In chapter three, I present data investigating the distinct molecular mechanisms that govern MHC-I regulation in PDAC using a CRISPRi screen to identify regulators and a proximity biotinylation assay to identify MHC-I interactors. Throughout this dissertation, I will discuss the implications of this work and how results from these studies will lead to a detailed molecular understanding of the underlying properties of PDA cells and potentially other aggressive cancers that lead to reduced MHC-I mediated antigen presentation. This work can help identify combination therapy strategies that could be effective in PDAC.

# Figures

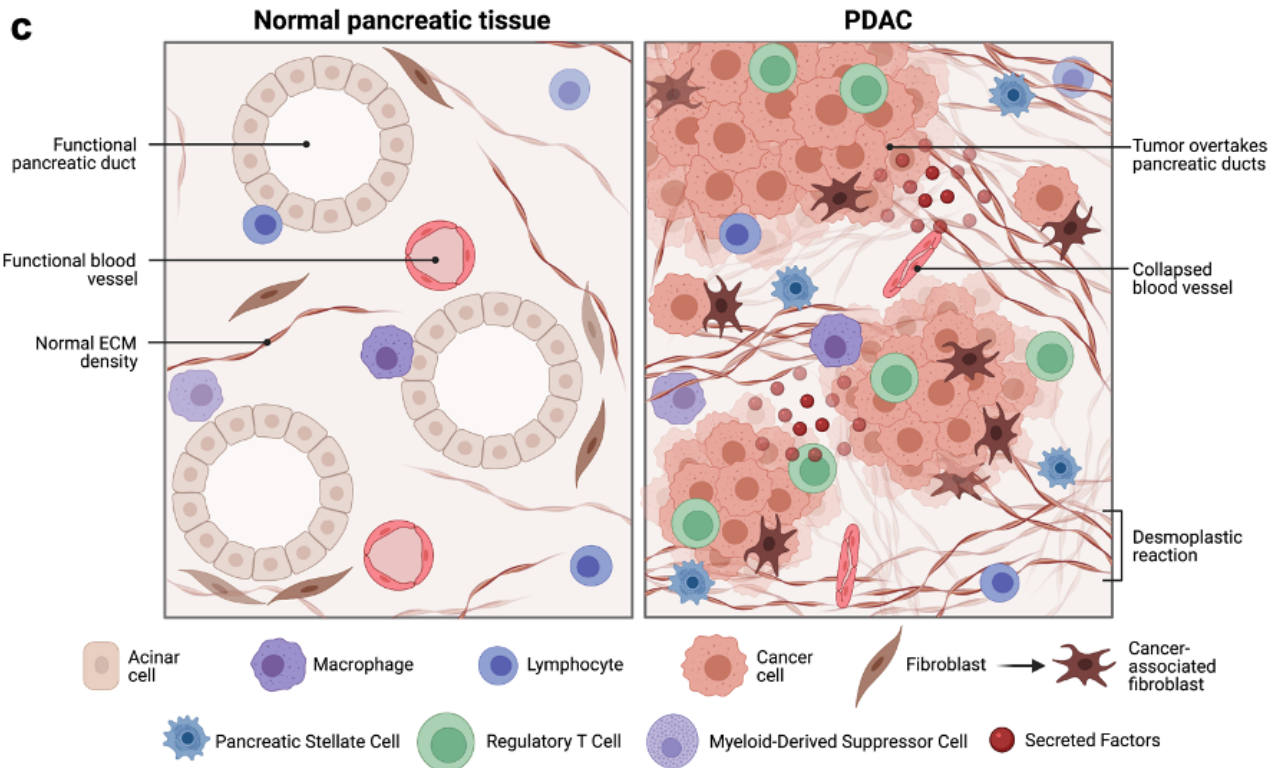
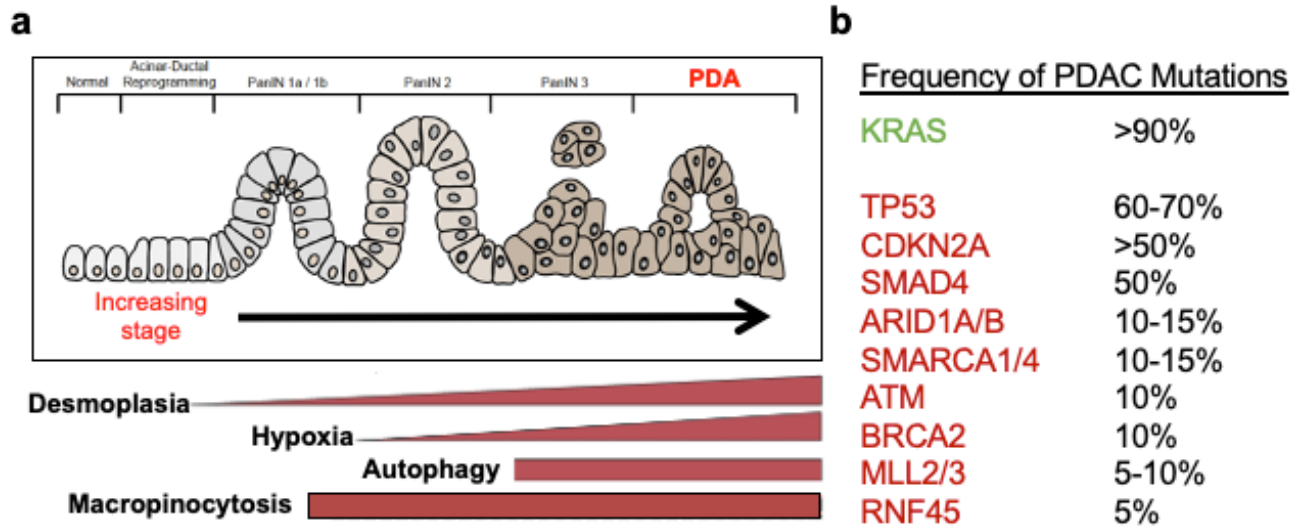


**Figure 1.1. Characteristic features and the tumor evolution of pancreatic ductal adenocarcinoma.** **A**, Step-wise, three-tier classification of tumor progression in PDAC from normal pancreatic epithelium to fully transformed cancer. This multi-stage progression is characterized by well-defined microscopic precursor lesions called pancreatic intraepithelial neoplasia (PanIN). With each increasing stage, the tumor upregulates a number cellular processes that contribute to the aggressiveness of the cancer and complexity of the microenvironment. (Figure re-printed from Perera and Bardeesy 2015). **B**, List of genetic mutations observed in PDAC. KRAS mutations early during tumorigenesis drive malignant transformation. As the tumor progresses, inactivation of tumor suppressors drives disease progression. Activating mutations in green and inactivating mutations in red. **C**, Normal pancreatic tissue versus PDAC. Overall composition of the hypoxic tumor microenvironment in PDAC characterized by desmoplasia and the recruitment of inflammatory and immune cells that contribute to anti-tumor immunity and tumorigenesis. Secreted factors, stromal cells, and a rich extracellular matrix composed of collagen and fibronectin affect the growth and survival of tumor cells (Figure made with BioRender).

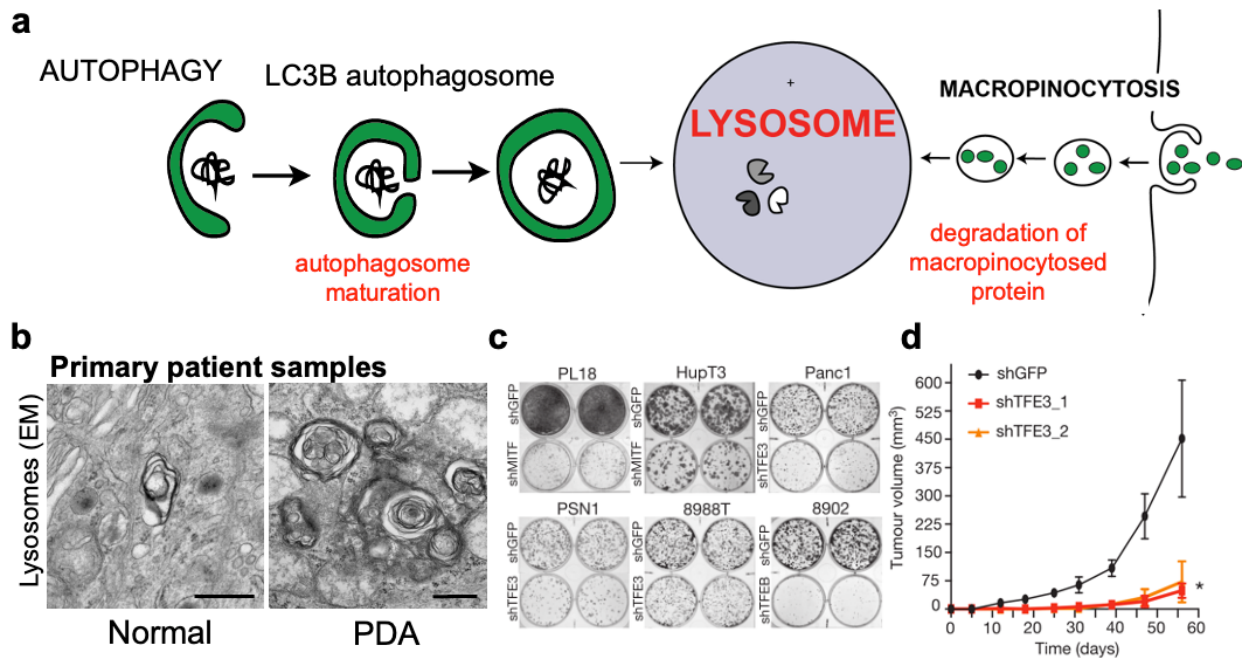


**Figure 1.2. Lysosomal degradation pathways and reliance on the MiT/TFE factors for PDAC tumor growth.** **A**, The processes of autophagy and macropinocytosis converge on the lysosome, an organelle that contains many digestive enzymes involved in waste removal and degradation of cellular substrates. Both autophagy and macropinocytosis are evolutionarily conserved mechanisms that degrade and recycle intracellular and extracellular material, respectively. **B-D**, data from Perera et al., 2015 investigating the transcriptional control of autophagy-lysosome function in pancreatic cancer metabolism. **B**, Transmission electron micrographs that compares lysosomal abundance and composition in normal pancreas versus treatment naïve PDAC primary patient samples. Data indicate 12 times more lysosome abundance in PDAC patients. **C**, Knockdown of indicated MiT/TFE transcription factors in a panel of PDAC cell lines decreases *in vitro* colony-formation. **D**, Knockdown of TFE3 in a *in vivo* subcutaneous xenograft mouse model impaired tumor growth in Panc1 cells.

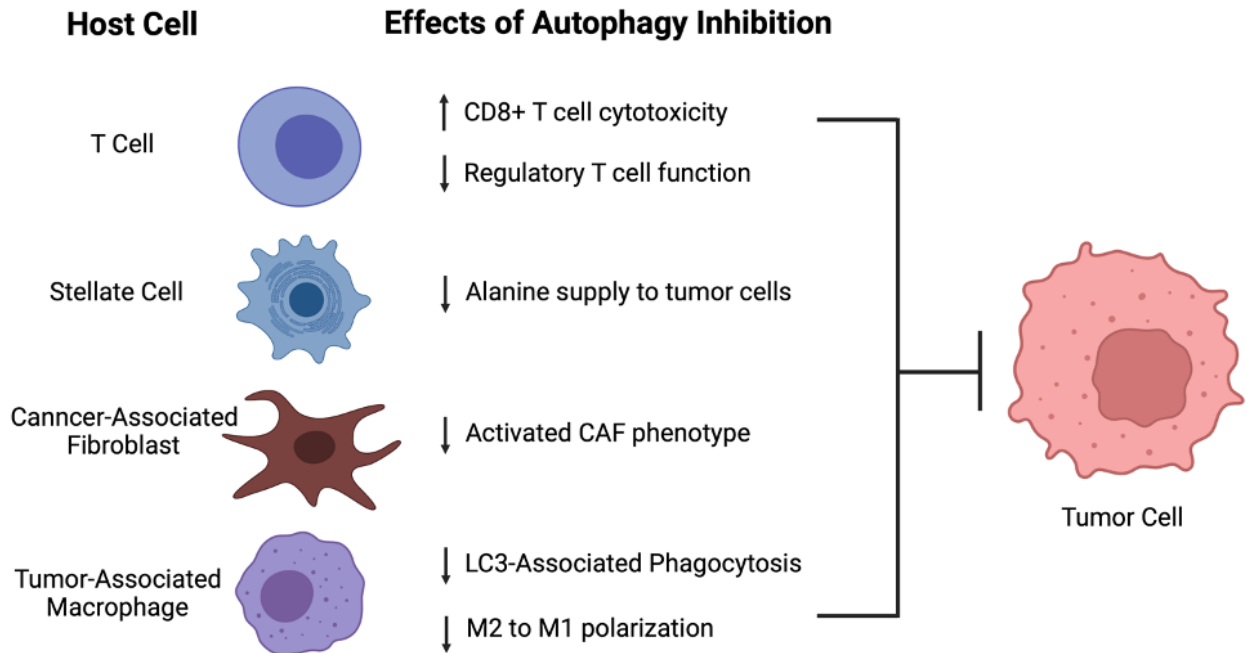


**Figure 1.3. Effects of autophagy inhibition in host-tumor cell interactions.** In addition to the modulatory effects autophagy inhibition has on tumor cells, non-cancer cells in the tumor microenvironment undergo extensive changes when systemic autophagy is inhibited. Several groups have described anti-tumor effects upon autophagy inhibition in immune and stromal cells independent of tumor cell inhibition. In addition to the tumor-protective roles of immune cells described in the text, inhibition of autophagy in the stromal compartment has been shown to decrease the nonessential amino acid alanine supply coming from pancreatic stellate cells (Sousa et al., 2016) and blunt the activation of the cancer-associated fibroblast phenotype (Valenica et al., 2014). (Figure adapted from Amaravadi et al., 2019).



## REFERENCES

Amaravadi, R. K. *et al.* Targeting Autophagy in Cancer: Recent Advances and Future Directions. *Cancer Discovery* **9**, 1167-81 (2019).

Balachandran, V. P. *et al.* Identification of unique neoantigen qualities in long-term survivors of pancreatic cancer. *Nature* **551**, 512-516 (2017).

Bar-Sagi, D. *et al.* A bright future for KRAS inhibitors. *Nature Cancer* **1**, 25-27 (2020).

Bardeesy, N. & DePinho, R. Pancreatic cancer biology and genetics. *Nat. Rev. Cancer* **2**, 897–909 (2002).

Bear, A. S. Challenges and Opportunities for Pancreatic Cancer Immunotherapy. *Cancer Cell* **38**(6), 788-802 (2020).

Behrends, C. *et al.* Network organization of the human autophagy system. *Nature* **466**(7302), 68-76 (2010).

Canto, M. I. *et al.* Frequent detection of pancreatic lesions in asymptomatic high-risk individuals. *Gastroenterology* **142**(4), 796-804 (2012).

Casey, S. C. *et al.* MYC regulates the antitumor immune response through CD47 and PD-L1. *Science* **352**(6282), 227-231 (2016).

Chang, C. & Campoli, M. Classical and Nonclassical HLA Class I Antigen and NK Cell-Activating Ligand Changes in Malignant Cells: Current Challenges and Future Directions. *Advances in Cancer Research*. **93**, 189-234 (2005).

- Chen D. *et al.* Chloroquine modulates antitumor immune response by resetting tumor-associated macrophages toward M1 phenotype. *Nature Communications* **9**, 873 (2018).
- Clark, C. E. *et al.* Dynamics of the immune reaction to pancreatic cancer from inception to invasion. *Cancer Res.* **67**(19), 9518-9527 (2007).
- Coelho, M. A. *et al.* Oncogenic RAS Signaling Promotes Tumor Immuno-resistance by Stabilizing PD-L1 mRNA. *Immunity* **47**(6), 1083-1099 (2017).
- Collins, M. A. *et al.* Oncogenic Kras is required for both the initiation and maintenance of pancreatic cancer in mice. *J Clin Invest.* **122**(2), 639-653 (2012).
- Conroy, T. *et al.* FOLFIRINOX or Gemcitabine as Adjuvant Therapy for Pancreatic Cancer. *N Engl J Med.* **379**(25), 2395-2406 (2018).
- Davidson, S. M. & Heiden, M. G. Vander. Critical Functions of the Lysosome in Cancer Biology. *Annu. Rev. Pharmacol. Toxicol.* **57**, 481–507 (2017).
- De Duve, C. and Wattiaux, R. Functions of lysosomes. *Annu Rev Physiol* **28**: 435-492 (1966).
- DeVorkin *et al.* Autophagy regulation of metabolism is required for CD8<sup>+</sup> T cell anti-tumor immunity. *Cell Reports* **27**, 502-513 (2019).
- Dias Carvalho, P. *et al.* KRAS Oncogenic Signaling Extends beyond Cancer Cells to Orchestrate the Microenvironment. *Cancer Res.* **78**(1): 7-14 (2018).

Dunn, G. P. *et al.* Cancer immunoediting: From immunosurveillance to tumor escape. *Nat. Immunol.* **3**, 991-998 (2002).

Encarnacion-Rosado, J. and Kimmelman, A. C. Harnessing metabolic dependencies in pancreatic cancers. *Nature Reviews Gastroenterology & Hepatology* **18**, 482-492 (2021).

Evans, R. A. *et al.* Lack of immunoediting in murine pancreatic cancer reversed with neoantigen. *JCI Insight* **1**(14), e88328 (2016).

Feig, C. *et al.* The pancreas cancer microenvironment. *Clin Cancer Res.* **18**(16), 4266-4276 (2012).

Fisher, D. T. *et al.* The two faces of IL-6 in the tumor microenvironment. *Semin. Immunol.* **26**, 38-47 (2014).

Frazier, J. *et al.* Multi-drug analyses in patients distinguish efficacious cancer agents based on both tumor cell killing and immunomodulation. *Cancer Research* **77**, 2869-2880 (2017).

Galon, J. and Bruni, D. Tumor Immunology and Tumor Evolution: Intertwined Histories. *Immunity* **52**, 55-81 (2020).

Garrido, F. *et al.* Implications for immunosurveillance of altered HLA class I phenotypes in human tumors. *Immunol. Today.* **18**, 89-95 (1997).

Gatica, D. *et al.* Cargo recognition and degradation by selective autophagy. *Nat Cell Biol.* **20**(3), 233-242 (2018).

Gonzalez, H. *et al.* Roles of the immune system in cancer: from tumor initiation to metastatic progression. *Genes Dev.* **32**(19-20), 1267-1284 (2018).

Gupta, S. *et al.* Lysosomal retargeting of Myoferlin mitigates membrane stress to enable pancreatic cancer growth. *Nat Cell Biol.* **23**(3), 232-242 (2021).

Hanahan, D. and Weinberg R. A. Hallmarks of Cancer: The Next Generation. *Cell* **144**, 646-674 (2011).

Haq, R. and Fisher, D. E. Biology and clinical relevance of the microphthalmia family of transcription factors in human cancer. *J Clin. Oncol.* **29**, 3474-3482 (2011).

He, C. and Klionsky, D. J. Regulation mechanisms and signaling pathways of autophagy. *Annu Rev Genet.* **43**, 67-93 (2009).

Hegde, S. *et al.* Dendritic Cell Paucity Leads to Dysfunctional Immune Surveillance in Pancreatic Cancer. *Cancer Cell* **37**(3), 289-307 (2020).

Hicklin, D. J. *et al.* HLA class I antigen downregulation in human cancers: T-cell immunotherapy revives an old story. *Mol. Med. Today.* **5**: 178-186 (1999).

Hingorani, S. R. Cellular and molecular conspirators in pancreas cancer. *Carcinogenesis* **35**(7), 1435 (2014).

- Ichimura, Y. *et al.* A ubiquitin-like system mediates protein lipidation. *Nature* **408**(6811), 488-492 (2000).
- Johnsen, A. K. *et al.* Deficiency of transporter for antigen presentation (TAP) in tumor cells allows evasion of immune surveillance and increase tumorigenesis. *J. Immunol.* **163**, 4224-4231 (1999).
- Karsli-Uzunbas, G. *et al.* Autophagy is required for glucose homeostasis and lung tumor maintenance. *Cancer Discovery* **4**(8), 914-927 (2014).
- Khazen, R. *et al.* Melanoma cell lysosome secretory burst neutralizes the CTL-mediated cytotoxicity at the lytic synapse. *Nature Communications* **7**, 10823 (2016).
- Kimmelman, A. C. The dynamic nature of autophagy in cancer. *Genes Dev.* **25**(19), 1999-2010 (2011).
- Kimmelman, A. C. Metabolic Dependencies in RAS-Driven Cancers. *Clin Cancer Res.* **21** (8), 1828-34 (2015).
- Kimmelman, A. C. and White, E. Autophagy and Tumor Metabolism. *Cell Metabolism* **25**(5), 1037-1043 (2017).
- Kumar, S. *et al.* Phosphorylation of Syntaxin 17 by TBK1 Controls Autophagy Initiation. *Dev Cell.* **49**(1), 130-144 (2019).

- Jones S, Zhang X, Parsons DW, Lin JC, Leary RJ, Angenendt P, Mankoo P, Carter H, Kamiyama H, Jimeno A, et al. Core signaling pathways in human pancreatic cancers revealed by global genomic analyses. *Science* **321**,1801–1806 (2008).
- Lawrence, R. E. and Zoncu, R. The lysosome as a cellular centre for signalling, metabolism, and quality control. *Nature Cell Biology* **21**, 133-142 (2019).
- Lee, J. J., Perera, R. M., et al. Stromal response to Hedgehog signaling restrains pancreatic cancer progression. *PNAS* **111**(30), E3091-E3100 (2014).
- Levine, B. and Kroemer G. Autophagy in the pathogenesis of disease. *Cell* **132**: 27-42 (2008).
- Li, J. et al. Tumor Cell-Intrinsic Factors Underlie Heterogeneity of Immune Cell Infiltration and Response to Immunotherapy. *Immunity* **49**, 178-193 e177 (2018).
- Li, Y. et al. The vitamin E analogue alpha-TEA stimulates tumor autophagy and enhances antigen cross-presentation. *Cancer Res.* **72**, 3535-3545 (2012).
- Lin, E. Y. et al. The macrophage growth factor CSF-1 in mammary gland development and tumor progression. *J Mammary Gland Biol. Neoplasia.* **7**, 147-162 (2002).
- Lind, M. H. et al. Tumor necrosis factor receptor 1-mediated signaling is required for skin cancer development induced by NF-kB inhibition. *Proc. Natl. Acad. Sci. USA.* **101**, 4972-4977 (2004).

Mancias, J. D. *et al.* Quantitative proteomics identifies NCOA4 as the cargo receptor mediating ferritinophagy. *Nature* **509**(7498), 105-9 (2014).

Martina, J. A. *et al.* The nutrient-responsive transcription factor TFE3 promotes autophagy, lysosomal biogenesis, and clearance of cellular debris. *Science Signaling* **7**, ra9 (2014).

Mathew, R. *et al.* Functional role of autophagy-mediated proteome remodeling in cell survival signaling and innate immunity. *Mol Cell*. **55**(6), 916-930 (2014).

Matsuda, M. *et al.* Interleukin 10 pretreatment protects target cells from tumor- and allo-specific cytotoxic T cells and downregulates HLA class I expression. *J. Exp. Med.* **180**, 2371-2376 (1994).

Mgrditchian, T. *et al.* Targeting autophagy inhibits melanoma growth by enhancing NK cells infiltration in a CCL5-dependent manner. *Proc Natl Acad Sci USA* **114**, E9271-9279 (2017).

Michaud, M. *et al.* Autophagy-dependent anticancer immune responses induced by chemotherapeutic agents in mice. *Science* **334**, 1573-1577 (2011).

Mizushima, N. *et al.* Autophagy fights disease through cellular self-digestion. *Nature* **451**(7182), 1069-1075 (2008).

Nagasaka, M. *et al.* KRAS Inhibitors – yes but what next? Direct targeting of KRAS – vaccines, adoptive T cell therapy and beyond. *Cancer Treatment Reviews* **101** (2021).

Nakamura, S. and Yoshimori, T. New insights into autophagosome-lysosome fusion. *J Cell Sci.* **130**(7), 1209-1216 (2017).

Neesse, A. *et al.* Stromal biology and therapy in pancreatic cancer. *Gut* **60**(6), 861-868 (2011).

Neessee, A. *et al.* CTGF antagonism with mAb FG-3019 enhances chemotherapy response without increasing drug delivery in murine ductal pancreas cancer. *Proc Natl Acad Sci USA* **110**(3), 12325-12330 (2013).

Noman, M. Z. *et al.* Blocking hypoxia-induced autophagy in tumors restores cytotoxic T-cell activity and promotes regression. *Cancer Research* **71**, 5976-5986 (2011).

O'Reilly, E. M. *et al.* Durvalumab With or Without Tremelimumab for Patients With Metastatic Pancreatic Ductal Adenocarcinoma: A Phase 2 Randomized Clinical Trial. *JAMA Oncol.* (2019).

Ostrem, J. M. *et al.* K-Ras(G12C) inhibitors allosterically control GTP affinity and effector interactions. *Nature* **503**(7477), 548-51 (2013).

Ozdemir, B. C. *et al.* Depletion of carcinoma-associated fibroblasts and fibrosis induces immunosuppression and accelerates pancreas cancer with reduced survival. *Cancer Cell* **25**(6), 719-734 (2014).



- Pandha, H., Rigg, A., John, J. & Lemoine, N. Loss of expression of antigen-presenting molecules in human pancreatic cancer and pancreatic cancer cell lines. *Clin Exp Immunol.* **148**, 127-135 (2007).
- Perera, R. M. *et al.* Transcriptional control of autophagy-lysosome function drives pancreatic cancer metabolism. *Nature* **524**, 361-365 (2015).
- Perera, R. M. & Zoncu, R. The Lysosome as a Regulatory Hub. *Annu. Rev. Cell Dev. Biol.* **32**, 223– 253 (2016).
- Pommier, A. *et al.* Unresolved endoplasmic reticulum stress engenders immune-resistant, latent pancreatic cancer metastases. *Science* **360** (2018).
- Pylayeva-Gupta, Y. *et al.* Oncogenic Kras-induced GM-CSF production promotes the development of pancreatic neoplasia. *Cancer Cell* **21**(6), 836-847 (2012).
- Qu, X. *et al.* Promotion of tumorigenesis by heterozygous disruption of the beclin 1 autophagy gene. *J Clin. Invest.* **112**(12), 1809-20 (2003).
- Rahib, L. *et al.* Estimated Projection of US Cancer Incidence and Death to 2040. *JAMA Network Open* **4**(4): e214708 (2021).
- Rao, S. *et al.* A dual role for autophagy in a murine model of lung cancer. *Nature Communications* **5**, 3056 (2014).
- Rebecca, V. W. and Amaravadi, R. K. Emerging strategies to effectively target autophagy in cancer. *Oncogene* **35**(1): 1-11 (2016).

- Rhim, A. D. *et al.* Stromal elements act to restrain, rather than support, pancreatic ductal adenocarcinoma. *Cancer Cell* **25**(6), 735-747 (2014).
- Ribas, A. and Wolchok, J. D. Cancer Immunotherapy Using Checkpoint Blockade. *Science* **359**(6382), 1350-1355 (2018).
- Richman, L. P. *et al.* Neoantigen Dissimilarity to the Self-Proteome Predicts Immunogenicity and Response to Immune Checkpoint Blockade. *Cell Syst.* **9**(4), 375-382.e4 (2019).
- Roczniak-Ferguson, A. *et al.* The transcription factor TFEB links mTORC1 signaling to transcriptional control of lysosome homeostasis. *Sci. Signal.* **5**, ra42 (2012).
- Ryan, D. P. *et al.* Pancreatic Adenocarcinoma. *N. Engl. J Med.* **371**, 1039-1049 (2014).
- Ryschich, E. *et al.* Control of T-cell-mediated immune response by HLA class I in human pancreatic carcinoma. *Clin Cancer Res.* **11**, 498-504 (2005).
- Sardiello, M. *et al.* A gene network regulating lysosomal biogenesis and function. *Science* **325**, 473-477 (2009).
- Schmitz-Winnenthal, F. *et al.* High frequencies of functional tumor-reactive T cells in bone marrow and blood of pancreatic cancer patients. *Cancer Res.* **65**(21), 10079-87 (2005).

- Settembre, C. *et al.* A lysosome-to-nucleus signalling mechanism senses and regulates the lysosome via mTOR and TFEB. *EMBO J.* **31**, 1095-1108 (2012).
- Settembre, C. *et al.* TFEB links autophagy to lysosomal biogenesis. *Science* **332**, 1429-1433 (2011).
- Shibutani, S. T. and Yoshimori, T. A current perspective of autophagosome biogenesis. *Cell Res.* **24**(1), 58-68 (2014).
- Siegel, R. L. *et al.* Cancer Statistics, 2021. *A Cancer Journal for Clinicians* **71**(1), 7-33 (2021).
- Singh, A. *et al.* A gene expression signature associated with “K-Ras addiction” reveals regulators of EMT and tumor cell survival. *Cancer Cell* **15**(6), 489-500 (2009).
- Sousa, C. M. *et al.* Pancreatic stellate cells support tumor metabolism through autophagic alanine secretion. *Nature* **536**(7617), 479-483 (2016).
- Tameire, F. *et al.* Cell intrinsic and extrinsic activators of the unfolded protein response in cancer: Mechanisms and targets for therapy. *Semin Cancer Biol.* **33**, 3-15 (2015).
- Uhl, M. *et al.* Autophagy within the antigen donor cell facilitates efficient antigen cross-priming of virus-specific CD8<sup>+</sup> T cells. *Cell Death Differentiation* **16**, 991-1005 (2009).

- Valencia, T. *et al.* Metabolic reprogramming of stromal fibroblasts through p62-mTORC1 signaling promotes inflammation and tumorigenesis. *Cancer Cell* **26**, 121-135 (2014).
- Vonderheide, R. H. and Bayne, L. J. Inflammatory networks and immune surveillance of pancreatic carcinoma. *Curr Opin Immunol.* **25**(2), 200-205 (2013).
- Waddell, N., Pajic, M., Patch, A. *et al.* Whole genomes redefine the mutational landscape of pancreatic cancer. *Nature* **518**, 495–501 (2015).
- Walczak, M. and Martens, S. Dissecting the role of the Atg12-Atg5-Atg16 complex during autophagosome formation. *Autophagy* **9**(3), 424-425 (2013).
- Weniger, M. *et al.* The Extracellular Matrix and Pancreatic Cancer: A Complex Relationship. *Cancers (Basel)* **10**(9): 316 (2018).
- Xu, X. *et al.* Autophagy is essential for effector CD8<sup>+</sup> T cell survival and memory formation. *Nature Immunology* **15**, 1152-1161 (2014).
- Yachida, S. and Iacobuzio-Donahue, C. A. Evolution and dynamics of pancreatic cancer progression. *Oncogene* **32**(45), 5253-60 (2013).
- Yang, S. *et al.* Pancreatic cancers require autophagy for tumor growth. *Genes Dev.* **25**, 717-729 (2011).
- Yang, A. *et al.* Autophagy is critical for pancreatic tumor growth and progression in tumors with p53 alterations. *Cancer Discov.* **4**, 905-913 (2014).

Yang, A. *et al.* Autophagy Sustains Pancreatic Cancer Growth through Both Cell-Autonomous and Nonautonomous Mechanisms. *Cancer Discovery* **8**(3), 276-287 (2018).

Yang, S. *et al.* Pancreatic cancers require autophagy for tumor growth. *Genes & Development* **25**, 717-729 (2011).

Ying, H. *et al.* Oncogenic Kras maintains pancreatic tumors through regulation of anabolic glucose metabolism. *Cell* **149** (3), 656-70 (2012).

Ying, H., Dey, P., Yao, W., Kimmelman, A. C., Draetta, G. F., Maitra, A., *et al.* Genetics and biology of pancreatic ductal adenocarcinoma. *Genes Dev.* **30**, 355–85 (2016).

Zaffagnini, G. and Martens, S. Mechanisms of Selective Autophagy. *J Mol Biol.* **428**(9): 1714-1724 (2016).

Zoncu, R. *et al.* mTORC1 Senses Lysosomal Amino Acids Through an Inside-Out Mechanism That Requires the Vacuolar H<sup>+</sup>-ATPase. *Science* **80**, 678–684 (2011).

**Chapter 2: Autophagy Promotes Immune Evasion by Downregulating MHC-I in  
Pancreatic Cancer**

## **Abstract**

Immune evasion is a major obstacle for cancer treatment. Common mechanisms of evasion include impaired antigen presentation caused by mutations or loss of heterozygosity of MHC-I, which has been implicated in resistance to immune checkpoint blockade (ICB) therapy (Rooney et al., 2015; McGranahan et al., 2017; Rodig et al., 2018). However, in PDAC, which is resistant to most therapies including ICB (O'Reilly et al., 2019), mutations that cause loss of MHC-I are rarely found (Waddell et al., 2015) despite the frequent downregulation of MHC-I expression (Ryschich et al. 2005; Pandha et al., 2007; Pommier et al., 2018). Here we show that, in PDAC, MHC-I molecules are selectively targeted for lysosomal degradation by an autophagy-dependent mechanism that involves the autophagy cargo receptor NBR1. PDAC cells display reduced expression of MHC-I at the cell surface and instead demonstrate predominant localization within autophagosomes and lysosomes. Notably, inhibition of autophagy restores surface levels of MHC-I and leads to improved antigen presentation, enhanced anti-tumor T cell responses and reduced tumor growth in syngeneic host mice. Accordingly, the anti-tumor effects of autophagy inhibition are reversed by depleting CD8<sup>+</sup> T cells or reducing surface expression of MHC-I. Inhibition of autophagy, either genetically or pharmacologically with chloroquine, synergizes with dual ICB therapy (anti-PD1 and anti-CTLA4 antibodies), and leads to an enhanced anti-tumor immune response. Our findings demonstrate a role for enhanced anti-tumor immune response. Our findings demonstrate a role for enhanced autophagy or lysosome function in immune evasion by selective targeting of MHC-I molecules for degradation, and provide a rationale for the combination of autophagy inhibition and dual ICB as a therapeutic strategy against PDAC.

## **Background**

The immune system displays the power to regulate tumor biology by eliciting an adaptive and innate immune response. While productive immunosurveillance allows leukocytes to recognize transformed cells and elicit anti-tumor immunity, cancers have developed sophisticated mechanisms to promote their growth in a process called “cancer immunoediting” (Schreiber et al., 2011). To evade immune detection, tumors undergo positive selection for cells that have either lost the ability to present neoantigens or are capable of inducing an immunosuppressive microenvironment (Beatty et al., 2015; Hanahan & Weinberg, 2011). Recent advances in immunotherapy have led to remarkable tumor remissions and revolutionized cancer treatment, but despite many successes, not all tumors respond equally (Spranger et al., 2016). The heterogeneous response of cancers to immuno-therapy regimens suggests the existence of multiple mechanisms for evasion of the immune system.

Several well-characterized mechanisms of immune evasion have been described, including alterations of signaling pathways that confer cancer-survival advantages, changes in tumor cell metabolism that impact tumor infiltrating lymphocytes, and importantly, altered regulation of cell surface proteins (Spranger et al., 2018). Downregulation of MHC-I proteins and mutation of HLA alleles can lead to loss of antigenicity, prohibiting malignant cells to present antigenic peptide and recruit tumor-specific T cells to elicit a cytotoxic response. HLA dysfunction allows for the selection of tumor cells that no longer present antigen and are therefore immune to cytotoxic T cell activity, thereby enabling subsequent tumor progression and metastasis. In approximately 20-60% of solid malignancies such as breast, lung, melanoma, and renal



cancers, downregulation of MHC-I proteins correlates with poor clinical prognosis (Chang & Campoli, 2005). Modification of MHC-I expression can occur through impaired epigenetic, transcriptional, and post-transcriptional levels of antigen presentation machinery in human tumors (Campoli & Ferrone, 2008). In the absence of genetic and epigenetic changes, altered trafficking can function as an alternative mechanism to downregulate MHC-I protein levels in cancer cells (Algarra et al., 2000). Thus, alterations in cellular trafficking may be a previously underappreciated mechanism of MHC-I regulation in cancer.

## **Results**

### **MHC-I is enriched in lysosomes of PDAC cells and displays reduced cell surface expression**

Human PDAC cell lines expressed heterogeneous levels of total MHC-I protein (Figure 1A), and notably, exhibited a punctate cytoplasmic distribution of MHC-I that co-localized with lysosomes (Figure 1B). By contrast, non-transformed human pancreatic ductal epithelial (HPDE) cells showed predominant localization of MHC-I on the plasma membrane (Figure 1B). Indeed, MHC-I molecules were highly enriched in PDAC lysosomes as compared to HPDE lysosomes (Figure 1C, Extended Data Figure 1A, B). Moreover, lysosomal inhibition resulted in accumulation of MHC-I within lysosomes, which confirms that MHC-I is actively routed to the lysosome for degradation (Figure 1D). A substantial fraction of the MHC-I puncta also co-localized with the increased autophagy levels in PDAC (Yang et al., 2011, 2014; Perera et al., 2015) (Figure 1E). Notably, similar phenotypes were observed in several non-small-cell lung cancer (NSCLC) cell lines. Non-transformed bronchial epithelial cells (BEAS-2B) show extensive membrane localization

of MHC-I. In contrast, H441 and A549 NSCLC lines show significant intracellular localization of MHC-I that co-localizes with autophagosomes and lysosomes, similar to PDAC (Extended Data Figure 1C, D). There is heterogeneity, as some lines show predominantly membrane localization (HCT116 and H358).

Flow cytometry-based analysis of total intracellular versus plasma membrane MHC-I confirmed a higher relative abundance of intracellular MHC-I in most PDAC cell lines (Figure 1F). Similarly, surface levels of MHC-I were lower in PDAC cells derived from a genetically engineered mouse model (GEMM) of PDAC (Yang et al., 2018) than in normal pancreas cells (Extended Data Figure 1E). Furthermore, immunofluorescence staining revealed that all human PDAC tumors analyzed contained considerable regions with intracellular MHC-I localization (Figure 1G, Extended Data Figure 1F), supporting our in vitro findings. To assess this, we have developed a sensitive immunofluorescence approach that can localize the expression of MHC-I selectively in tumor cells, which are co-stained with cytokeratin 19 to distinguish ductal structures. Tumors were more heterogeneous than the cell lines, with the extent of intracellular MHC-I staining in ductal structures ranging from 20% to 50%. Nonetheless, given that all tumors analyzed had significant regions of intracellular staining, we predict this would ultimately render them resistant to immune checkpoint blockade (which is what is observed in human patients). Together, these data suggest that MHC-I molecules are reduced at the cell surface and predominantly localized within autophagosomes and lysosomes in PDAC.

### **Autophagy inhibition increases the levels and plasma localization of MHC-I**

Autophagy inhibition by ATG3 and ATG7 knockdown as well as lysosomal inhibition with V-ATPase inhibitor bafilomycin A1 (BafA1) increased total and plasma membrane MHC-

I levels in PDAC cells (Figure 2A, B, Extended Data Figure 2 A-I). Notably, lysosomal inhibition with BafA1 or chloroquine increased levels of MHC-I proteins but did not affect those involved in antigen processing and presentation, which suggests that autophagy inhibition would not impair these steps. Quantitative proteomics analysis on human PDAC cells treated with CQ show consistent increase in MHC-I molecules upon lysosomal inhibition, while ERAP1, ERAP2, TAP1, TAP2, and TAPBP were not affected, which was confirmed by western blot analysis (Extended Data Figure 2K, L). Similar phenotypes were also observed in several NSCLC cell lines. Accordingly, H441 and A549 cells demonstrate MHC-I increases upon pharmacologic and genetic inhibition of autophagy (Extended Data Figure 2M-O).

Previous studies have revealed non-canonical functions for a subset of autophagy proteins in alternative trafficking pathways such as LC3-associated phagocytosis (LAP) (Cunha et al., 2018) and endocytosis (LANDO) (Heckmann et al., 2019). Knockdown of FIP200, which is required for autophagy but not for LAP or LANDO, led to an increase in MHC-I levels (Extended Data Figure 3A-C). Similarly, knockdown of ATG14, ATG13, or ULK1, all required for autophagy but dispensable for LAP, increased surface MHC-I levels (Extended Data Figure 3D-J). By contrast, no obvious increase in surface MHC-I was observed after knockdown of RUBICON, which is required for LAP and LANDO but not for autophagy (Extended Data Figure 3K, L). Collectively, these data suggest a specific role for macroautophagy in the trafficking of MHC-I to the lysosome.

### **NBR1 mediates selective autophagy of MHC-I**

Autophagy was originally discovered as a non-selective degradation pathway; however, autophagy can selectively degrade target molecules using autophagy cargo receptor

proteins such as p62/sequestosome 1, TAX1BP1, NDP52, optineurin (OPTN), NCOA4, and NBR1, that bind to and recruit substrates to autophagosomal membranes (Kirkin et al., 2009). To identify autophagy receptor protein(s) involved in MHC-I degradation in PDAC cells, we generated a proximity biotinylation assay in which the C terminus of HLA-A was fused to the biotin ligase TurboID (Branon et al., 2018) and Flag (HLA-A-TrID). After addition of biotin, HLA-A-TrID covalently tags endogenous proteins within a few nanometers of the ligase with biotin (Extended Data Figure 4A, B). Among the autophagy receptors tested, only NBR1 showed significant biotinylation, indicating that NBR1 interacts with MHC-I (Figure 2C). Furthermore, immunofluorescence revealed more frequent co-localization between NBR1 and MHC-I in PDAC cells relative to HPDE cells (Figure 2D). NBR1 has been shown to interact with and target ubiquitylated substrates for degradation (Kirkin et al., 2009). Indeed, MHC-I is poly-ubiquitylated in PDAC cells (Figure 2E, Extended Data Figure 4C), whereas LC3B is not ubiquitylated and EGFR is mono-ubiquitylated, as previously described (Mosesson et al., 2003). Accordingly, NBR1 lacking its ubiquitin-associated (UBA) domain was unable to co-localize with MHC-I, despite retaining localization with LC3B (Figure 2F, Extended Data Figure 4D). Finally, NBR1 knockdown increased total and plasma membrane MHC-I levels in PDAC cells (Figure 2G, H, Extended Data Figure 4E, F), confirming a role for NBR1 in MHC-I regulation. Together, these data demonstrate that surface MHC-I is decreased in PDAC via an NBR1-mediated autophagy-lysosomal pathway.

### **Autophagy inhibition enhances anti-tumor immunity**

CD8<sup>+</sup> cytotoxic T cells have crucial roles in anti-tumor immunity. We hypothesized that reduced surface levels of MHC-I on PDAC cells may facilitate their evasion from CD8<sup>+</sup> T

cells, which recognize tumor antigens presented by MHC-I. To test this, we used mouse PDAC cells derived from C57BL/6 mice and engineered them to express a doxycycline (Dox)-inducible dominant-negative mutant of ATG4B (ATG4B(C74A)), which potently inhibits autophagy (Yang et al., 2018; Fujita et al., 2008). Dox treatment efficiently inhibited autophagy and increased surface MHC-I levels (Extended Data Figure 5A, B). To address whether this mechanism is exclusive to MHC and/or other APC components, we assessed the change in levels of 9 proteins in the immunological synapse (highlighted with underlines) as well as a panel of other plasma membrane proteins upon autophagy inhibition in mouse PDAC cells expressing Dox-inducible mTurquoise2-tagged ATG4B(C74A). Only MHC-I proteins (H-2K<sup>b</sup>, H-2D<sup>b</sup>) increase their cell surface expression in response to autophagy inhibition, whereas immune inhibitory molecules that bind and suppress the function of tumor-infiltrating CD8<sup>+</sup> T cells, including PD-L1, Galectin-9, and CD155, showed insignificant changes upon dox treatment (Extended Data Figure 5C). These data support a specific mechanism that links surface MHC-I levels and autophagy.

To evaluate antigen presentation, the model neoantigen ovalbumin (OVA) was expressed in mouse PDAC cells carrying Dox-inducible ATG4B(C74A) (Extended Data Figure 5D). Dox treatment increased surface expression of both MHC-I and OVA-derived peptide SIINFEKL bound to H-2K<sup>b</sup>, confirming enhanced peptide presentation (Figure 3A, B, Extended Data Figure 5E, F). OVA-specific CD8<sup>+</sup> T cells (OT-I cells) co-cultured with PDAC cells pre-treated with Dox showed higher proliferation and expression of IFN- $\gamma$  and TNF than those co-cultured with non-pre-treated PDAC cells (Figure 3C, Extended Data Figure 5G, H). Accordingly, Dox-treated PDAC cells showed reduced viability after co-

culture with OT-I cells (Figure 3D), indicating enhanced T-cell-mediated tumor cell killing. Notably, these effects were MHC-I specific, as a H-2K<sup>b</sup>-SIINFEKL blocking antibody partially inhibited OT-I proliferation and rescued PDAC cell viability in the setting of autophagy inhibition (Figure 3C, D). Collectively, these results indicate that tumor-specific inhibition of autophagy leads to increased antigen presentation, which enhances CD8<sup>+</sup> T cell proliferation, activation, and tumor cell killing in vitro.

To test the effect of autophagy inhibition on anti-tumor immune responses in vivo, mouse PDAC cells expressing Dox-inducible mStrawberry (mSt) or mSt-ATG4B(C74A) (4B) (Extended Data Figure 6A) were orthotopically transplanted into syngeneic (C57BL/6) mice. Autophagy-inhibited cells (4b) formed smaller tumors with higher MHC-I expression than control cells (mSt), while PD-L1 expression was unchanged (Figure 3E-G, Extended Data Figures 6B-F, 7K). Moreover, autophagy-inhibited tumors (4B) exhibited a significant increase in infiltrating CD8<sup>+</sup> T cells and a decrease in myeloid-derived suppressor cells, a major immunosuppressive cell type in PDAC tumors (Li et al., 2018) (Figure 3H, Extended Data Figure 6G-J). Similarly, knockdown of ATG7 resulted in a significant reduction in tumor burden and an increase in tumor-infiltrating T cells (Extended Data Figure 6K-N). Notably, there was a significant correlation between smaller tumor sizes and increased CD8<sup>+</sup> T cell infiltration (Extended Data Figure 6O), supporting a role of T cell immunity in control of autophagy-deficient tumors. Similar results were obtained in liver metastasis model – mice injected with autophagy-inhibited cells (4B) exhibited lower metastatic burden, higher MHC-I expression on cancer cells, and more tumor-infiltrating CD8<sup>+</sup> T cells than mice injected with control cells (mSt) (Figure 3I-L, Extended Data Figure

6P-T). Together, these results confirm that autophagy-inhibition restores surface levels of MHC\_I on cancer cells and enhances anti-tumor T cell response in vivo.

Notably, antibody-mediated CD8<sup>+</sup> T cell depletion restored the growth of autophagy-inhibited tumors (4B) (Figure 3m, Extended Data Figure 7A-C), confirming the role of CD8<sup>+</sup> T cells in the tumor control. We also find that mice deficient for CD103<sup>+</sup> dendritic cells (*Batf3*<sup>-/-</sup>) (Hildner et al., 2008), which have pivotal roles in CD8<sup>+</sup> T cell priming (Broz et al., 2014) and recruitment into tumors (Li et al., 2018; Spranger et al., 2017), showed almost complete loss of tumor-infiltrating CD8<sup>+</sup> T cells (Figure 3N, Extended Data Figure 7D-F). Accordingly, growth of autophagy-inhibited tumors (4B) was restored in *Batf3*<sup>-/-</sup> mice (Figure 3O). These results indicate that the anti-tumor effects of tumor-specific autophagy inhibition are mediated, at least in part, by CD8<sup>+</sup> T cells, and this process requires CD103<sup>+</sup> dendritic cells.

Finally, to confirm the effect of increased MHC-I expression after autophagy inhibition on tumor growth in vivo, cell surface levels of MHC-I were depleted by knockdown of beta-2 microglobulin (B2M), a crucial component of the MHC-I complex (Extended Data Figure 7G). B2M knockdown led to MHC-I depletion in vivo, decreased the number of CD8<sup>+</sup> T cells in autophagy-inhibited tumors (4B), and rescued the growth of autophagy-inhibited tumors (4B) (Figure 3P-R, Extended Data Figure 7H-K). We also found that tumor-infiltrating CD103<sup>+</sup> DCs, which are increased in autophagy-inhibited tumors (4B), were decreased after B2M knockdown (Extended Data Figure 7F, J). This is in line with a recent study showing that MHC-I-restricted antigen-recognition by CD8<sup>+</sup> T cells can trigger activation of dendritic cells, which further augments recruitment of CD8<sup>+</sup> T cells into the tumor (Dangaj et al., 2019). Overall, these data indicate that increased surface expression

of MHC-I on PDAC cells after tumor-specific inhibition of autophagy is a prerequisite for increased CD8<sup>+</sup> T cell infiltration and tumor cell killing.

### **Basal autophagy flux levels determine immunogenicity of PDAC cells**

Our data led us to hypothesize that basal autophagy flux might determine the immunogenicity of PDAC cells. Mouse PDAC cells grown as organoids (Boj et al., 2015) exhibited considerable heterogeneity in autophagy flux (measured as the ratio of green to red fluorescent protein signal, GFP/RFP), which closely resembled that of orthotopic tumors (Extended Data Figure 8A-B). Taking advantage of this heterogeneity, PDAC cells with the lowest and highest 20% of GFP/RFP ratio were isolated as autophagy-high (AT<sub>hi</sub>) and autophagy-low (AT<sub>lo</sub>) cells (Extended Data Figure 8C). Transcriptome analysis confirmed upregulation of autophagy or lysosome related genes and the MiT/TFE transcription factors, master regulators of autophagy or lysosome gene expression (Perera et al., 2015), in the AT<sub>hi</sub> population (Extended Data Figure 8D-E). Notably, AT<sub>hi</sub> and AT<sub>lo</sub> cells derived from a clonal population showed a similar transcriptional profile (Extended Data Figure 8F), suggesting that diversities in basal autophagy flux arise not from genetic variations but instead from heterogeneous expression of the autophagy lysosome gene program (Perera et al., 2015).

Consistent with the cell-autonomous roles of autophagy in PDAC (Yang et al., 2011, 2014), AT<sub>lo</sub> cells exhibited reduced clonogenic capacity in vitro (Extended Data Figure 8G-H), which is a similar result to the decreased clonogenic growth of ATG4B(C74A)-expressing cells (Extended Data Figure 8L). After orthotopic transplantation into syngeneic mouse hosts, AT<sub>lo</sub> cells gave rise to smaller tumors than AT<sub>hi</sub> cells (Extended Data Figure 9A). Notably, this was reproduced using cells sorted from a clonal population



(Extended Data Figure 9B), which suggests that tumor-cell intrinsic factors account for the observed phenotypes rather than differences in retroviral-vector integration sites or copy numbers of the reporter. Furthermore, ATlo-derived tumors exhibited higher MHC-I expression and more tumor-infiltrating CD8<sup>+</sup> T cells, which inversely correlated with tumor weight, compared to AThi-derived tumors (Extended Data Figure 9C-F). This growth advantage of AThi-derived tumors was lost in nude mice (Extended Data Figure 9G), confirming a role of T cells in the suppression of ATlo-derived tumors. In the liver metastasis model, mice injected with ATlo cells in the spleen exhibited lower metastatic burden and higher MHC-I expression on PDAC cells than mice injected with AThi cells (Extended Data Figure 9H-J). CD8<sup>+</sup> T cells tended to accumulate around PDAC cells with low-autophagy flux, whereas CD8<sup>+</sup> T cells were scarce around PDAC cells with high-autophagy flux (Extended Data Figure 9K). These results, along with the data in autophagy inhibition models, indicate that autophagy is a crucial determinant of immunogenicity in PDAC cells.

### **Autophagy inhibition sensitizes PDAC to dual ICB**

PDAC is refractory to ICB (O'Reilly et al., 2019). To test whether inhibition of autophagy might sensitize PDAC to ICB, we treated established syngeneic orthotopic tumors with anti-PD-1 antibody alone or dual ICB (anti-PD-1 and anti-CTLA4 antibodies). Consistent with a recent clinical trial (O'Reilly et al., 2019), control tumors (mSt) did not respond to either treatment. By contrast, autophagy-inhibited tumors (4b) responded significantly to dual ICB (Figure 4A-C), but not to anti-PD1 antibody alone (Extended Data Figure 10A-C). To determine the activation status of these T cells, we measured the surface expression of Tim3 and PD1, markers indicative of T-cell exhaustion. Tumor-infiltrating

CD8<sup>+</sup> T cells were categorized into three groups: PD1<sup>+</sup>Tim3<sup>+</sup>, PD1<sup>+</sup>Tim3<sup>-</sup>, and PD1<sup>-</sup>Tim3<sup>-</sup>. It has been reported that PD1<sup>+</sup>Tim3<sup>+</sup> double positive cells represent the most severely exhausted or dysfunctional phenotype, while PD1<sup>+</sup>Tim3<sup>-</sup> single positive cells exhibit partial dysfunction (Sakuishi et al., 2010). CD8<sup>+</sup> T cells in autophagy-inhibited tumors displayed reduced double positive cells and an increase in single positive cells, suggesting that CD8<sup>+</sup> T cells in autophagy-inhibited tumors are less exhausted and retain greater function than severely dysfunctional PD1<sup>+</sup>TIM3<sup>+</sup> cells<sup>26</sup>. These results indicate that tumor-specific autophagy inhibition sensitizes PDAC tumors to dual ICB.

Finally, we assessed the translatability of our findings to systemic autophagy inhibition using chloroquine – a clinically available anti-malarial agent that inhibits acidification of the lysosome and has been used to inhibit autophagy in patients (Munster et al., 2002; Karasic et al., 2019; Zeh et al., 2020). Treatment with lysosomal inhibitors chloroquine or BafA1 increased surface levels of MHC-I in mouse PDAC cells in vitro (Extended Data Figure 10H). Chloroquine treatment also increased surface expression of MHC-I, but not PD-L1, in orthotopic tumors (Extended Data Figure 10L-K). However, chloroquine monotherapy failed to significantly reduce tumor weight or increase the infiltration of T cells (Extended Data Figure 10L, M), possibly due to the unfavorable pharmacokinetics of this drug in vivo (Munster et al., 2002). Notably, the combination of chloroquine and dual ICB exerted potent anti-tumor activity (Figure 4E-I) and a reduction in autophagy flux was confirmed in chloroquine-treated tumors (Figure 4J, Extended Data Figure 10N). Moreover, tumors treated with chloroquine plus ICB exhibited increased infiltrations of CD8<sup>+</sup> T cells (Figure 4K) and an increase in the number of functional PD<sup>+</sup>TIM3<sup>-</sup>CD8<sup>+</sup> T

cells (Extended Data Figure 10O). Overall, these data indicate that autophagy inhibition, either in cancer cells alone or systematically, sensitizes PDAC tumors to dual ICB therapy (Figure 4L).

## **Discussion**

Our results suggest that autophagy is a crucial regulator of immunogenicity in PDAC cells. This is in line with a recent study that showed that the lysosomal pathway is strongly correlated with reduced infiltration of CD8<sup>+</sup> T cells in human PDAC (Markosyan et al., 2019). In addition, autophagy-related genes are enriched in MHC-I negative PDAC cells that reside in liver metastasis (Pommier et al., 2018), also suggesting a role for autophagy as a negative regulator of MHC-I. Given the critical roles for the autophagy and lysosome system in supporting PDAC metabolism and growth (Yang et al., 2011; Perera et al., 2015), our data on immune evasion add to the growing list of cell-autonomous and non-cell-autonomous functions of the autophagy and lysosome system in PDAC pathogenesis (Yang et al., 2014, 2018).

We found that systemic autophagy inhibition by chloroquine, as well as tumor-specific autophagy inhibition, sensitizes PDAC to dual ICB. In addition, recent evidence accounts for the improved therapeutic effects of systemic autophagy inhibition. First, host autophagy supports tumor growth by providing nutrients (Sousa et al., 2016; Katheder et al., 2017; Poillet-Perez et al., 2018). Second, loss of autophagy proteins or chloroquine treatment increases surface levels of MHC-I in dendritic cells, leading to enhanced CD8<sup>+</sup> T cell response in models of virus infection (Loi et al., 2016). Also, autophagy inhibition directly enhances anti-tumor activity of CD8<sup>+</sup> T cells (DeVorkin et al., 2019). Finally, loss

of LAP, a process also inhibited by chloroquine, polarizes tumor-associated macrophages into a tumor-suppressive phenotype (M1), promoting anti-tumor T cell responses (Cunha et al, 2018). In line with these, clinical trials have shown that hydroxychloroquine, a derivative of chloroquine, has activity in patients with PDAC (Karasic et al., 2019; Zeh et al., 2020). Whether the addition of ICB would be synergistic remains to be determined.

In this study, we focused on CD8<sup>+</sup> T cells, given their direct interaction with MHC-I on cancer cells. However, we also observed changes in other immune cells such as myeloid-derived suppressor cells, CD4<sup>+</sup> T cells and CD103<sup>+</sup> dendritic cells after inhibition of autophagy. Investigating how these and changes in other immune cell types are mediated, such as the potential involvement of secreted proteins from PDAC cells after autophagy inhibition, will be important subjects of future work.

Despite the evidence mentioned above and previous work demonstrating that inhibition of autophagy does not impair anti-tumor adaptive immunity (Starobinetes et al., 2016), autophagy inhibition has been reported to affect some aspects of the immune system such as memory formation in virus-specific CD8<sup>+</sup> T cells and CD4<sup>+</sup> T cell priming by dendritic cells (Xu et al., 2014; Lee et al., 2010) and may impair chemotherapy-induced immunogenic cell death (Michaud et al., 2011). Therefore, further studies will be needed to define more subtle aspects of the immune response after autophagy inhibition and how to best combine autophagy or lysosome blockade with cytotoxic and immune-based therapies. For example, deeper insights into the potential effect of basal immunogenicity (Moral et al., 2020) on response to autophagy inhibition, the differences in mutational burden in mouse and human tumors (Ward et al., 2016), the effect of potential dominant antigens in experimental systems, and the heterogeneity described here in terms of MHC-

l expression in patients will probably contribute to the successful clinical translation of our findings. Importantly, the mechanistic insights described here about how autophagy can promote immune evasion, provide strong rationale to pursue these studies with the ultimate goal of developing new therapeutic approaches for patients with PDAC.

## Figures

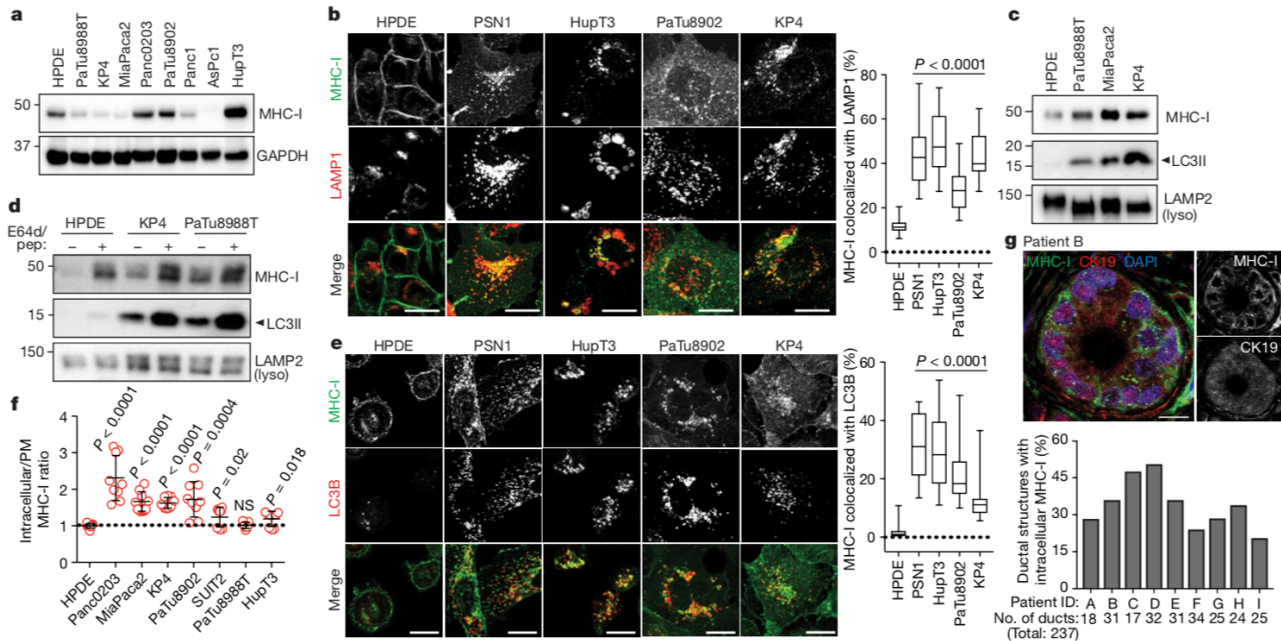


**Figure 2.1. MHC-I is enriched in lysosomes of PDAC cells and displays reduced cell surface expression.** **A**, Levels of MHC-I (HLA-A, -B, -C) in HPDE and human PDAC cell lines. **B**, Left, localization of MHC-I (green) relative to LAMP1-positive (red) lysosomes. Scale bars, 20  $\mu$ m. Right, the percentage co-localization ( $n = 14$ -20 fields). **C**, Presence of MHC-I in immune-isolated lysosomes. **D**, Accumulation of MHC-I in immune-isolated lysosomes after treatment with lysosome inhibitors E64d and pepstatin A (pep) for 6 h. **E**, Left, localization of MHC-I (green) relative to LC3B-positive (red) autophagosomes. Scale bars, 20  $\mu$ m. Right, the percentage co-localization ( $n = 14$ -20 fields). **F**, Flow cytometry-based analysis of intracellular versus plasma membrane (PM) MHC-I levels. Graph shows higher intracellular MHC-I relative to plasma membrane MHC-I in PDAC cells ( $n = 9$  replicates pooled from 3 independent experiments per cell line). Data are mean  $\pm$  s.d. **G**, Top, intracellular localization of MHC-I (green) in CK19-positive (red) ducts from a specimen from a patient with PDAC. Scale bars, 20  $\mu$ m. Bottom, the percentage of ducts showing intracellular MHC-I localization. A representative of at least two independent experiments is shown in **A**, **C**, **D**. For box-and-whisker plots (**B**, **E**), center lines indicate median values and whiskers represent minimum and maximum values.  $P$  values were determined by unpaired two-tailed  $t$ -tests. NS, not significant. See Supplementary Figure 1 for gel source data.

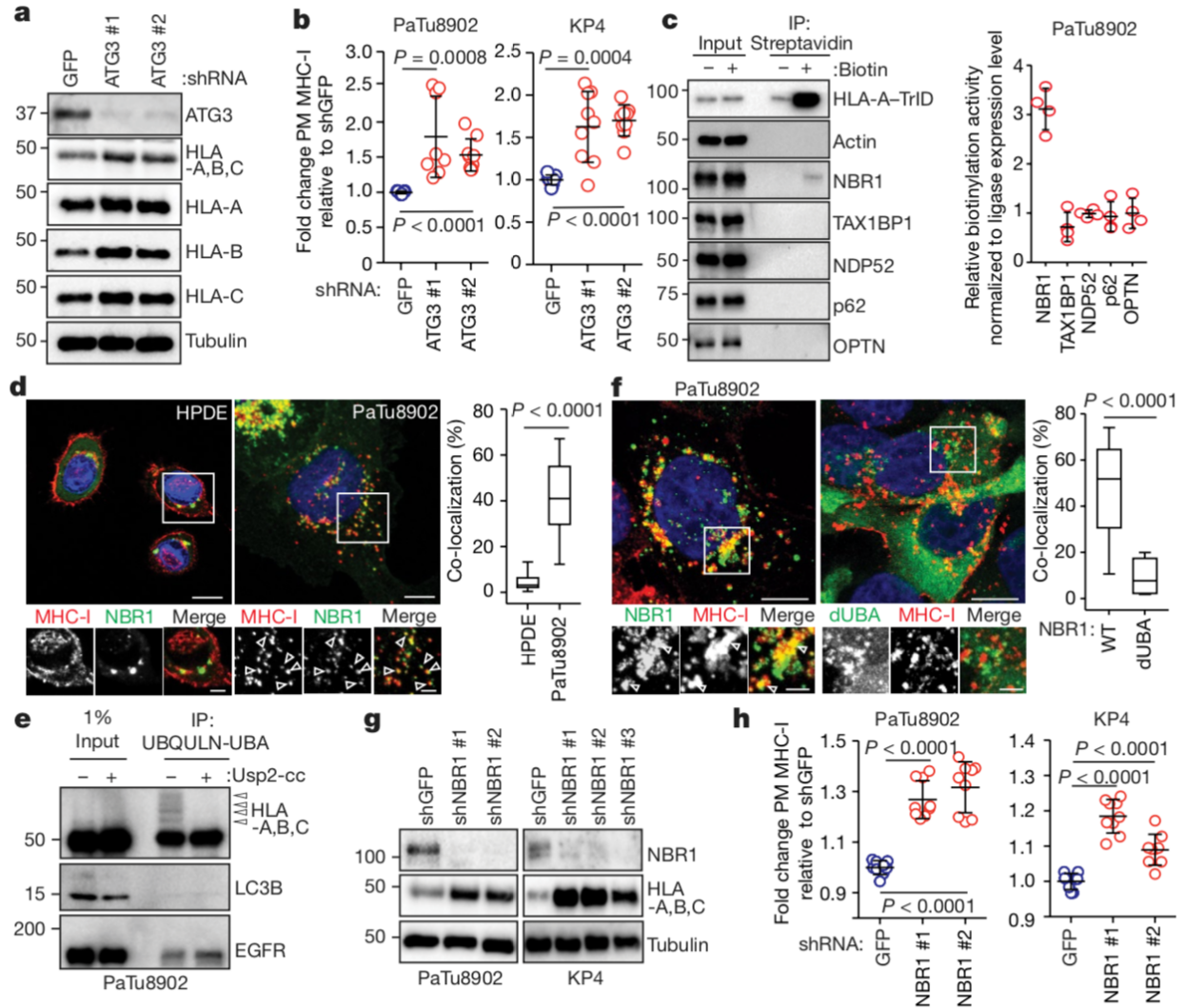


**Figure 2.2. NBR1 promotes MHC-I trafficking to the lysosome through an autophagy-dependent pathway.** **A**, Effect of short hairpin RNA (shRNA)-mediated ATG3 knockdown on levels of HLA-A, HLA-B, and HLA-C in human PaTu8902 cells. **B**, Flow cytometry-based quantification of plasma membrane levels of MHC-I (HLA-A, -B, -C) (PaTu8902,  $n = 9, 8, 9$ ; KP4,  $n = 9$  per group; data pooled from three independent experiments) after shRNA-mediated ATG3 knockdown. **C**, Left, KP4 cells expressing HLA-A-TrID were labelled with 10uM biotin for 30 min. Biotinylation of proteins was detected after streptavidin pull down. Asterisk denotes self-biotinylation of HLA-A-TrID. IP, immunoprecipitation. Right, enrichment for each receptor ( $n = 4$  independent experiments). **D**, Localization of MHC-I (red) relative to GFP-NBR1 (green) in HPDE and PaTu8902 cells. Arrowheads show examples of co-localization. Scale bars, 20  $\mu$ m. Graph shows quantification of co-localization (HPDE,  $n = 23$  fields; PaTu8902,  $n = 20$  fields). **E**,

Endogenous ubiquitylated proteins were affinity captured from PaTu8902 cells with UBQLN1-UBA-conjugated beads. Arrowheads indicate MHC-I polyubiquitylation. Treatment of affinity-captured samples for 1 h with purified deubiquitylating enzyme USp2-cc (+) to induce deubiquitylation leads to loss of MHC-I polyubiquitylation. Control proteins: LC3B (no ubiquitylation) and EGFR (mono-ubiquitylation). **F**, Left, endogenous MHC-I co-localizes with wild-type (WT) GFP-NBR1 but not GFP-NBR1 lacking its UBA domain (dUBA). Right, quantification of co-localization (GFP-NBR1;  $n = 17$  fields; GFP-NBR1 dUBA;  $n = 14$  fields). Scale bars, 20  $\mu\text{m}$  and 10  $\mu\text{m}$  (inset). **G**, Effect of shRNA-mediated NBR1 knockdown on levels of MHC-I. **H**, Flow cytometry-based quantification of plasma membrane MHC-I ( $n = 9$  replicates from three independent experiments) after NBR1 knockdown. A representative of at least two independent experiments is shown in A, E, G. Data are mean  $\pm$  s.d. (B, C, H). Box-and-whisker plots are as in Figure 1.  $P$  values were determined by unpaired two-tailed  $t$ -tests. See Supplementary Figure 1 for gel source data.



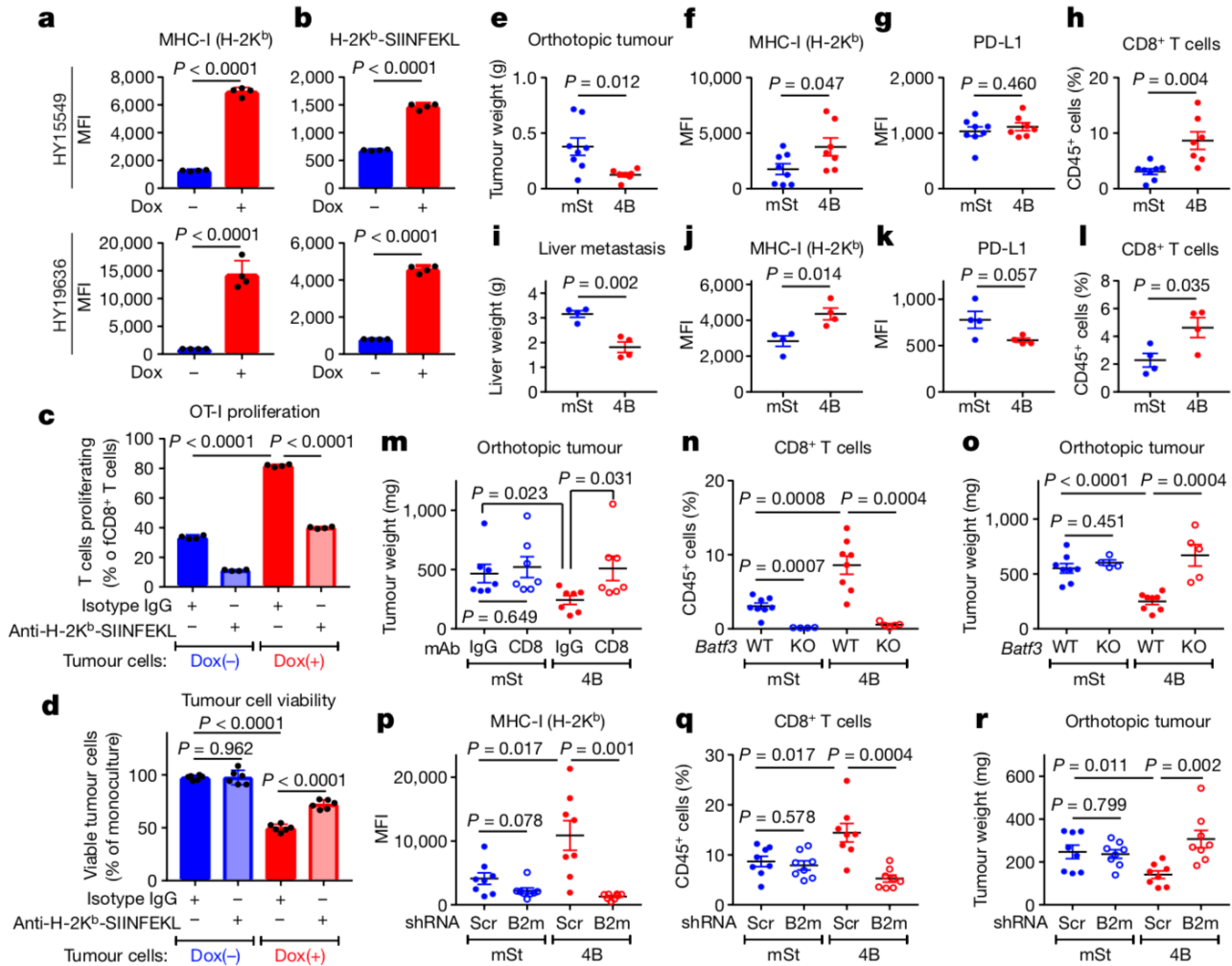


**Figure 2.3. Autophagy inhibition enhances anti-tumor T cell response.** **A, B**, Surface H-2K<sup>b</sup> (**A**) and H-2K<sup>b</sup>-SIINFEKL (**B**) measured by flow cytometry. Mouse PDAC cells expressing OVA and Dox-inducible mTurquoise2-ATG4B(C74A) were grown as organoids and treated with or without Dox (1  $\mu\text{g ml}^{-1}$ ) for 96 h ( $n = 4$  per group). MFI, mean fluorescent intensity. **C, D**, Co-culture of OT-I cells with HY19636 cells shown in **A** and **B**. After 48 h, OT-I proliferation was measured by CFSE dilution ( $n = 4$  per group) (**C**) and PDAC cell viability was measured by Cell-Titer Glo ( $n = 6$  per group) (**D**). **E-R**, HY15549 cells carrying Dox-inducible mStrawberry (mSt) or mSt-ATG4B(C74A) (4B) were orthotopically (**E-H, M-R**) or intrasplenically (**I-L**) injected into syngeneic mice (C57BL/6). The expression of MHC-I and PD-L1 on PDAC cells (**F, G, J, K, P**) and tumor-infiltrating CD8<sup>+</sup> T cells (**H, L, N, Q**) quantified by flow cytometry. **E-H**, Orthotopic tumors obtained on day 20 (mSt,  $n = 8$ ; 4B,  $n = 7$ ). **I-L**, Livers obtained on day 15 ( $n = 4$  per group). **E, I**, Weight of tumors (**E**) and livers (**I**). **F-H, J-L**, Flow cytometry analysis. **M**, Weight of tumors after treatment with isotype control IgG or neutralizing monoclonal antibody against CD8 ( $n = 7$  per group). **N, O**,

Tumors in wild-type or *Batf3*<sup>-/-</sup> knockout (KO) mice ( $n = 8, 4, 8$  and  $5$ ; left to right). **N**, Quantification of CD8<sup>+</sup> cells. **O**, Tumor weight. **P-R**, Tumors expressing control shRNA (Scr) or shRNA against B2m ( $n = 8$  per group), collected on day 20. **P**, **Q**, Flow cytometry analysis. **R**, Tumor weight. Data are mean  $\pm$  s.d. (A-D) or s.e.m. (E-R).  $n$  indicates biological replicates (A-D) or individual mice (E-R). For A-M, P-R, experiments were performed at least twice and representative data of one experiment are shown.  $P$  values were determined by unpaired two-tailed  $t$ -tests.

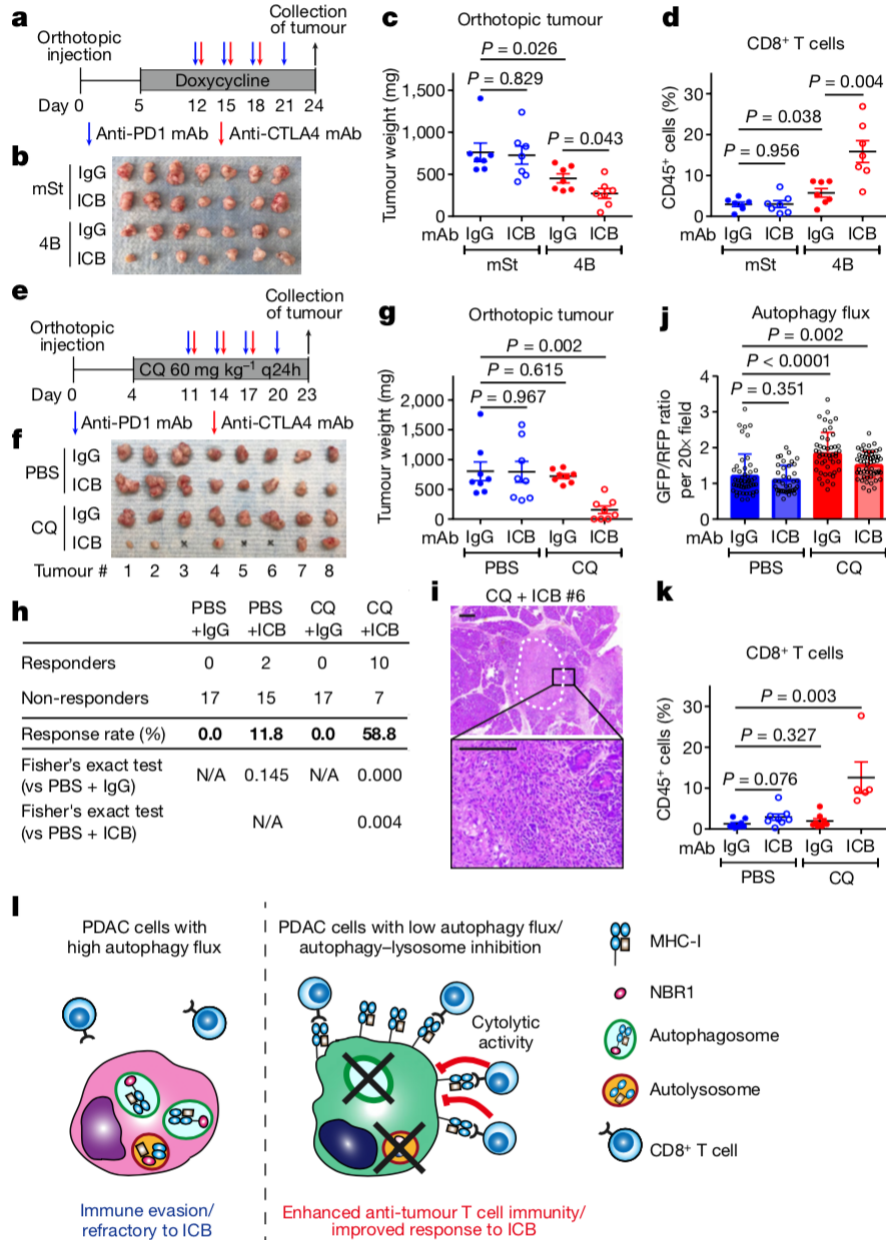
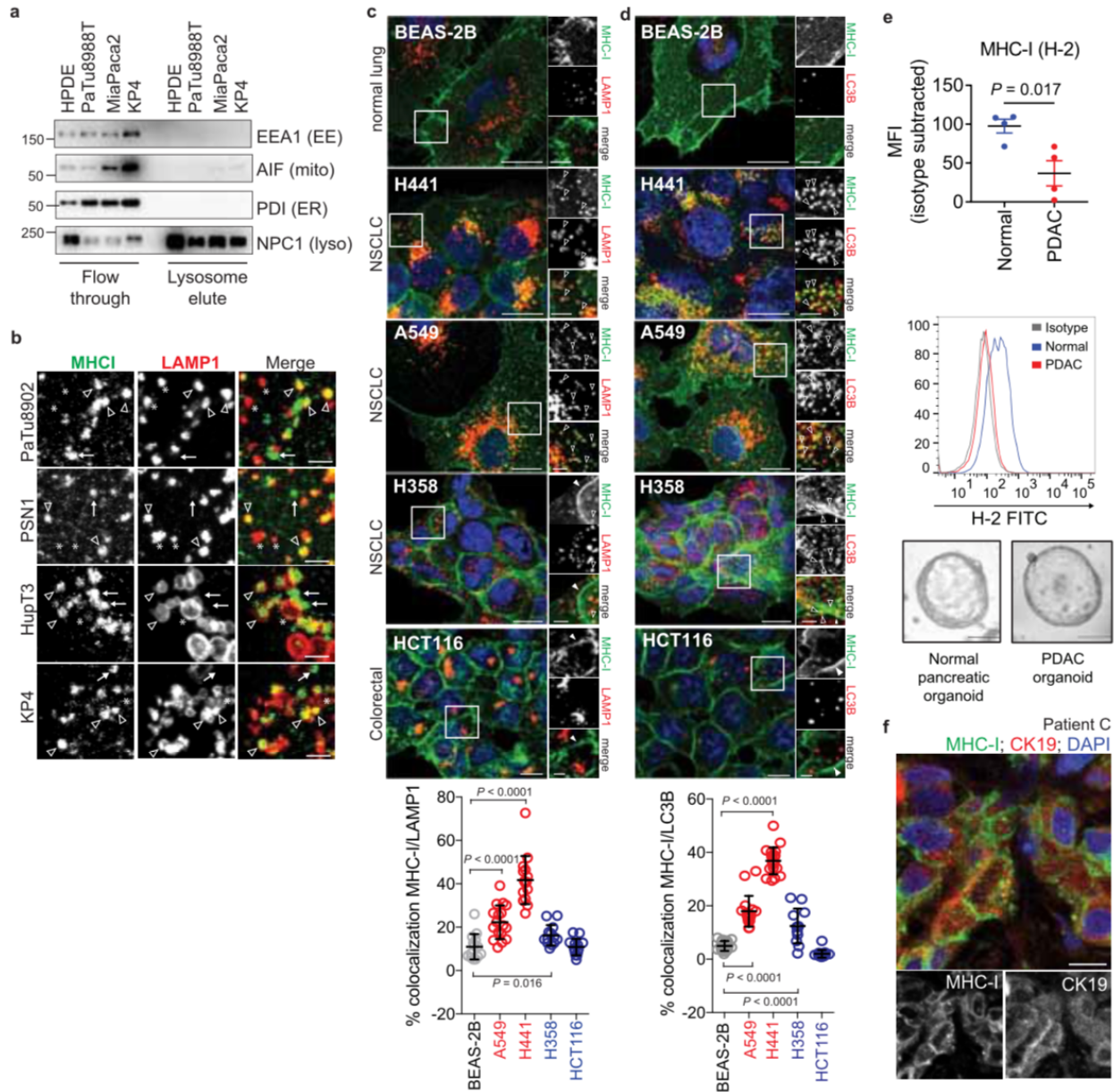


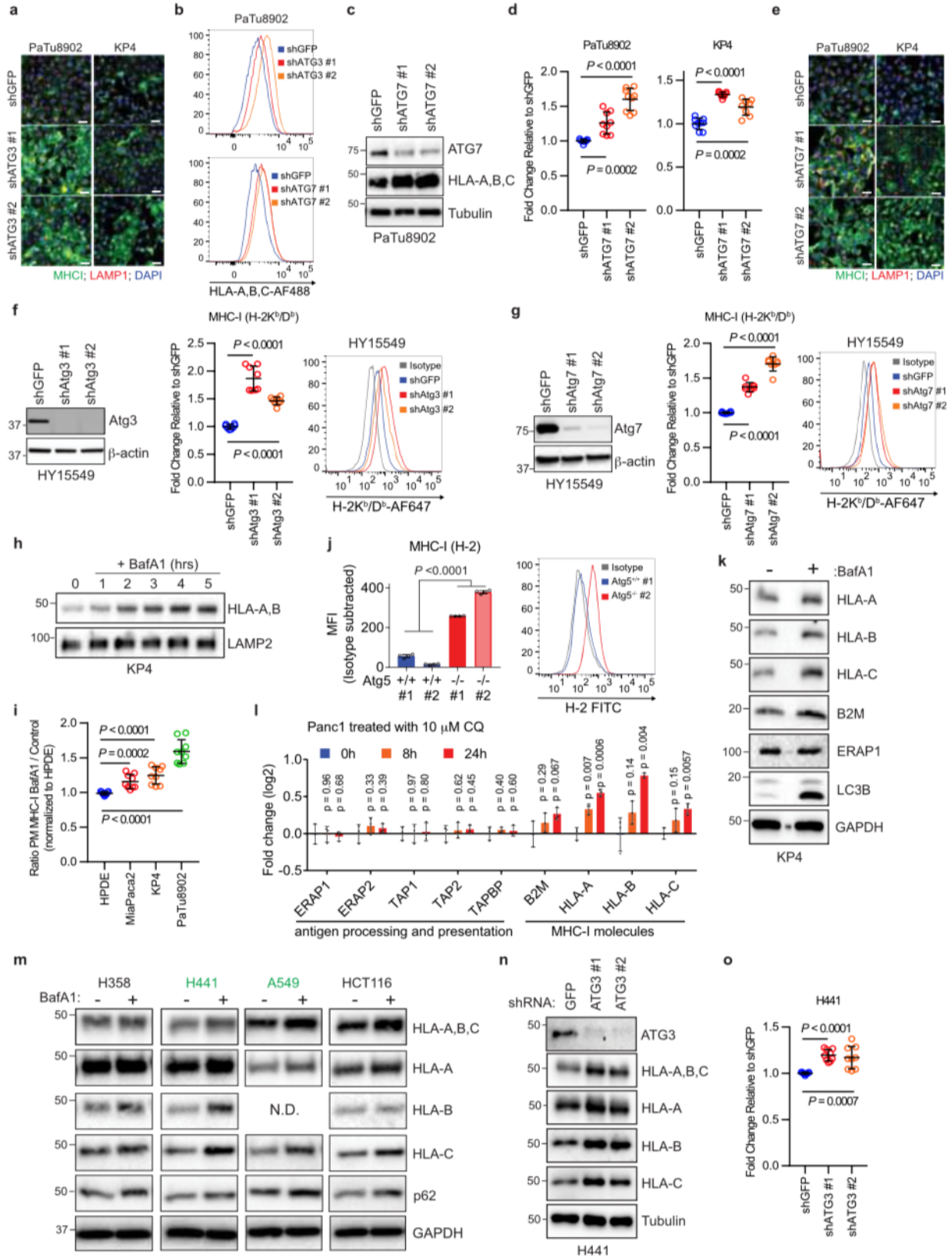
**Figure 2.4. Autophagy inhibition sensitizes PDAC to dual ICB.** **A-D**, Mice bearing orthotopic tumors (HY15549) expressing Dox-inducible mSt or 4B received isotype control IgG or dual ICB (anti-PD1 and CTLA4 monoclonal antibodies; mAb) ( $n = 7$  per group). **A**, Study design. **B**, **C** Images (**B**) and weight (**C**) of tumors. **D**, Quantification of tumor-infiltrating CD8<sup>+</sup> T cells by flow cytometry. **E-K**, Mice bearing orthotopic tumors (HY15549) expressing the GFP-LC3-RFP reporter received chloroquine (CQ) and ICB ( $n = 8$  per group). **E**, Study design. Q24h, every 24 hours. **F**, **G**, images (**F**) and (**G**) of tumors. No

macroscopic tumor was identified in three mice receiving chloroquine plus dual ICB (#3, 5, and 6). **H**, Response rates from two independent experiments. Response is defined as more than 80% reduction in tumor weights as compared with control tumors (PBS + IgG). N/A, not applicable. **I**, Representative hematoxylin and eosin (H&E) images of the pancreas undergoing tumor regression (#6). White dashed line indicates tumor remnants. Scale bars, 250 and 100  $\mu\text{m}$  (inset). **J**, Autophagy flux represented by GFP/RFP ratio per 20 x field ( $n = 49, 39, 47, \text{ and } 54$ ; left to right). Increased GFP/RFP ratio indicates reduced autophagy flux. **K**, Quantification of tumor-infiltrating CD8<sup>+</sup> T cells by flow cytometry ( $n = 8, 8, 8, \text{ and } 5$ ; left to right). **L**, In PDAC cells, surface MHC-I is downregulated by active degradation through the autophagy-lysosome system, contributing to the primary resistance to ICB. NBR1 binds to MHC-I, facilitating its trafficking to autophagosomes (left). Inhibition of autophagy or the lysosome restores surface MHC-I expression, leading to enhanced anti-tumor T cell immunity and improved response to ICB (right). Data are mean  $\pm$  s.e.m. (**C, D, G, K**) or s.d. (**J**).  $n$  indicates individual mice (**C, D, G, K**) or individual 20x fields (**J**). All experiments were performed twice and representative data of one experiment are shown.  $P$  values were determined by unpaired two-tailed  $t$ -tests.



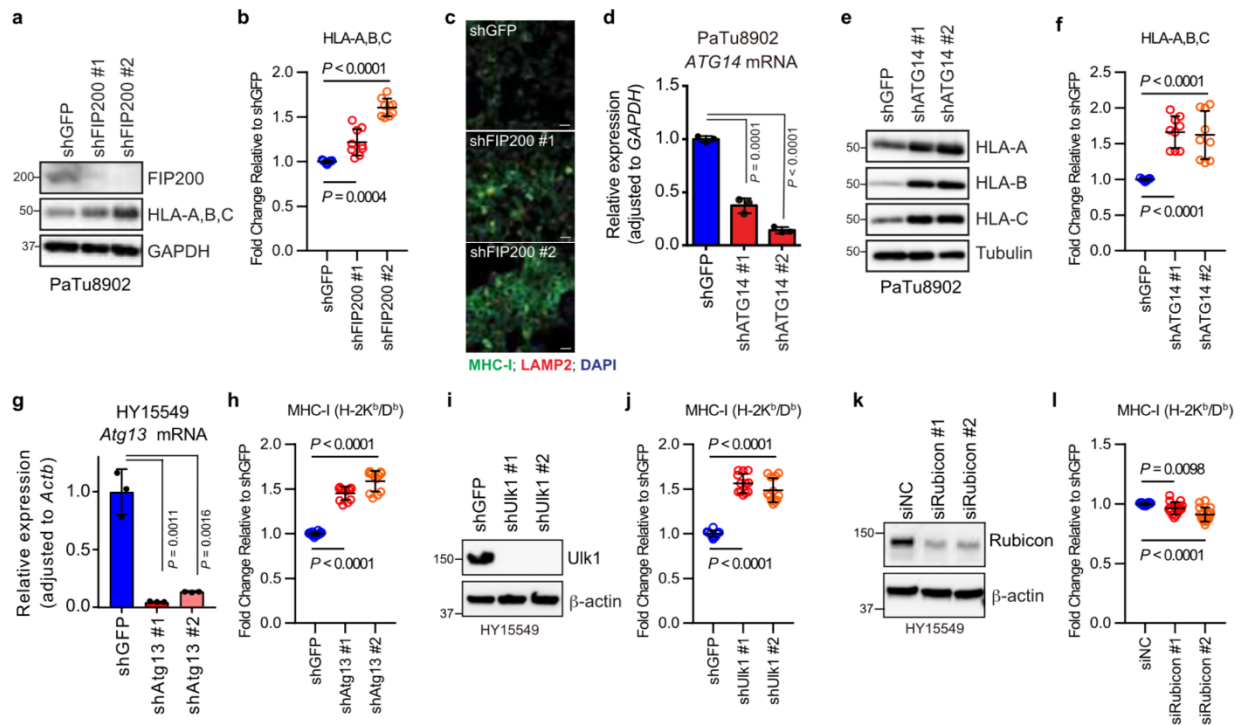
**Extended Data Figure 2.1e. Heterogeneous distribution of MHC-I in KRAS-mutant cancers.** **A**, Immuno-isolation of intact lysosomes from HPDE and PDAC cell lines showing absence of non-lysosome markers as indicated. EE, early endosome; ER, endoplasmic reticulum; lyso, lysosome; mito, mitochondria. **B**, High-power images showing MHC-I-positive, LAMP1-positive (arrowheads), MHC-I-positive, LAMP1-negative (arrows) and MHC-I-negative, LAMP1-positive (asterisk) puncta. Scale bars, 5  $\mu$ m. **C**, **D**, Top, localization of MHC-I (green) relative to LAMP1-positive (red) lysosomes (BEAS-2B,  $n = 14$ ; A549,  $n = 17$ ; H441,  $n = 15$ ; H358,  $n = 13$ ; HCT116,  $n = 13$ ) (c) or LC3B-positive (red) autophagosomes (BEAS-2B,  $n = 18$ ; A549,  $n = 17$ ; H441,  $n = 20$ ; H358,  $n = 12$ ; HCT116,  $n = 15$ ) (D) in the indicated cell lines. Bottom, quantification of percentage co-localization.

Cell lines indicated in red show significantly increased co-localization relative to BEAS-2B cells, and cell lines indicated in blue show a modest increase (H358) or no difference (HCT116). Data are mean  $\pm$  s.d. (**C**, **D**). Scale bars, 20  $\mu$ m and 10  $\mu$ m (inset). **E**, Flow cytometry-based analysis of surface MHC-I (H-2) in mouse normal pancreas (C57Bl/6) and mouse PDAC cells grown as organoids. Top, isotype-subtracted geometric MFI. Each dot represents different mice ( $n = 4$ ). Data are mean  $\pm$  s.e.m. Middle, representative flow cytometry plots. Bottom, representative images of organoids. **F**, Immunofluorescent staining images from a patient in Figure 1G showing intracellular localization of MHC-I (green) in CK29-positive (red) ducts. Scale bar, 20  $\mu$ m. A representative of at least two independent experiments is show in **A** and **E**. *P* values determined by unpaired two-tailed *t*-tests (**C-E**). See Supplementary Figure 1 for gel source data.

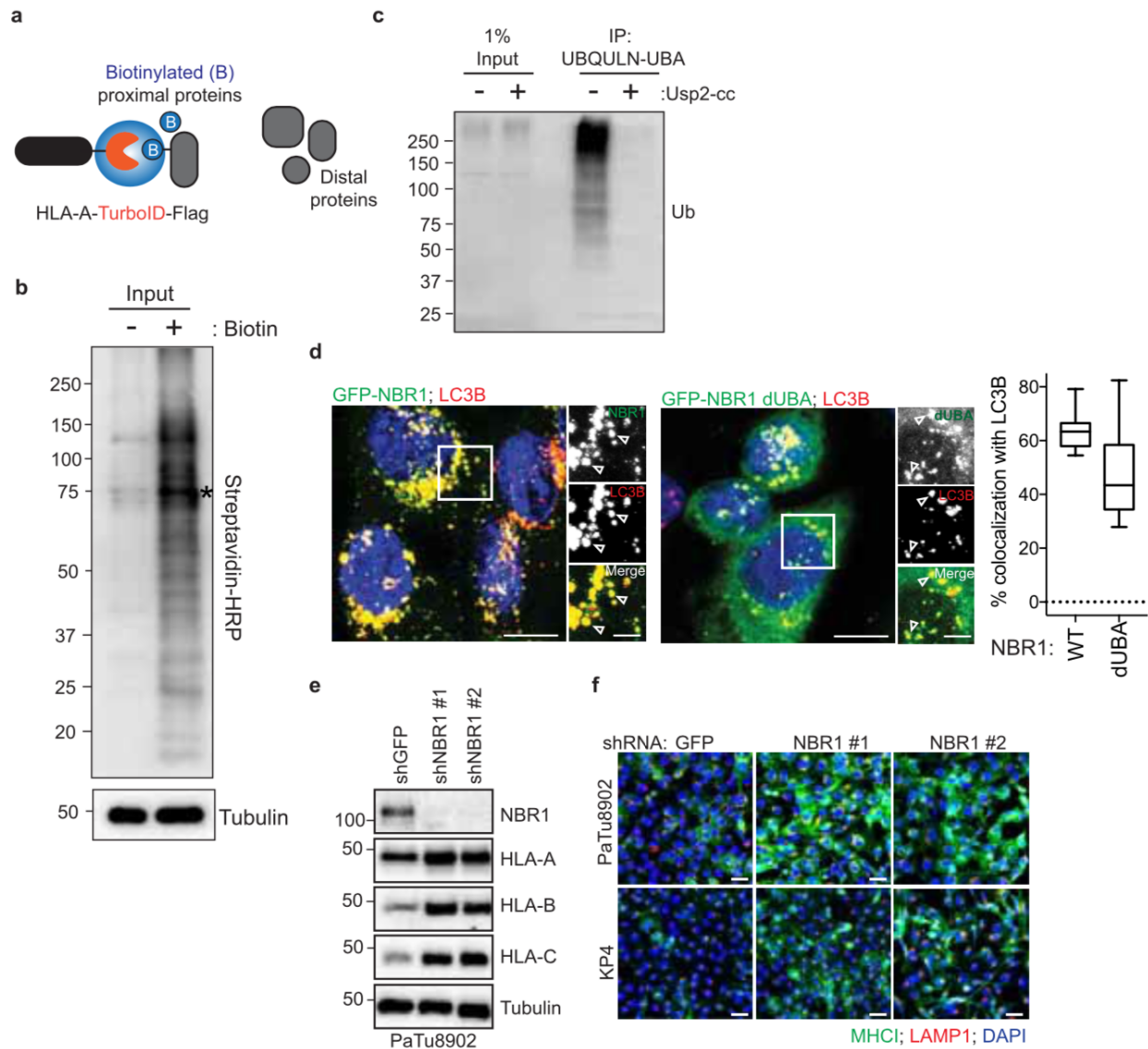


**Extended Data Figure 2.2e. Inhibition of autophagy and lysosomes restores MHC-I levels and plasma membrane localization.** **A**, Immunofluorescence staining of MHC-I after shRNA-mediated ATG3 knockdown. Scale bars, 50  $\mu$ m. **B**, Representative flow cytometry plots for PaTu8902 cells after knockdown of ATG3 (related to Fig. 2b) and ATG7 (see also **D**). Representative plots from **D** and Fig. 2b are shown. **C**, Effect of ATG7 knockdown on MHC-I (HLA-A, -B, -C) expression in PaTu8902 cells. **D**, Flow cytometry-based quantification of plasma membrane levels of MHC-I (HLA-A, -B, -C) after ATG7 knockdown ( $n = 9$  replicates from three independent experiments). **E**, Immunofluorescence staining of MHC-I following ATG7 knockdown. Scale bars, 50  $\mu$ m. **F**, **G**, Surface MHC-I levels after knockdown of ATG3 (**F**) or ATG7 (**G**) in mouse PDAC cells. Left, knockdown efficiency was confirmed by immunoblots. Middle, cell surface levels of MHC-I (H-2K<sup>b</sup>,D<sup>b</sup>) measured by flow cytometry ( $n = 8$  replicates from two independent experiments). Right, representative flow cytometry plots are shown. **H**, Treatment of KP4 cells with 150 nM BafA1 for the indicated times causes an increase in levels of HLA-A, -B. **I**, Flow cytometry-based quantification of plasma membrane MHC-I in the indicated cell lines after treatment with BafA1 for 16 h ( $n = 9$  replicates from three independent experiments). **J**, Surface MHC-I (H-2) levels measured by flow cytometry. Mouse PDAC organoids were established from *Atg5*<sup>+/+</sup> and *Atg5*<sup>-/-</sup> KPC cells.  $n = 4$  biological replicates. Data are representative of three independent experiments. Right, representative flow cytometry plots. **K**, Effect of BafA1 treatment on the expression levels of antigen presentation machinery. **L**, Quantitative proteomics analysis of Panc1 cells that were treated with chloroquine (10  $\mu$ M) for the indicated periods.  $n = 3$  biological replicates. **M**, Effect of BafA1 treatment on expression levels of MHC-I in the indicated cell lines. Cell lines denoted in green show a significant change across all HLA isoforms after BafA1 treatment. **N**, **O**, Effect of ATG3 knockdown in H441 cells on total MHC-I (**N**) and plasma membrane MHC-I (**O**) as measured by flow cytometry-based quantification ( $n = 9$  replicates from three independent experiments). A representative of at least two independent experiments is shown in **A–C**, **E–H**, **J**, **K**, **M**, **N**. Data are mean  $\pm$  s.d. *P* values were determined by unpaired two-tailed *t*-tests. See Supplementary Figure 1 for gel source data.



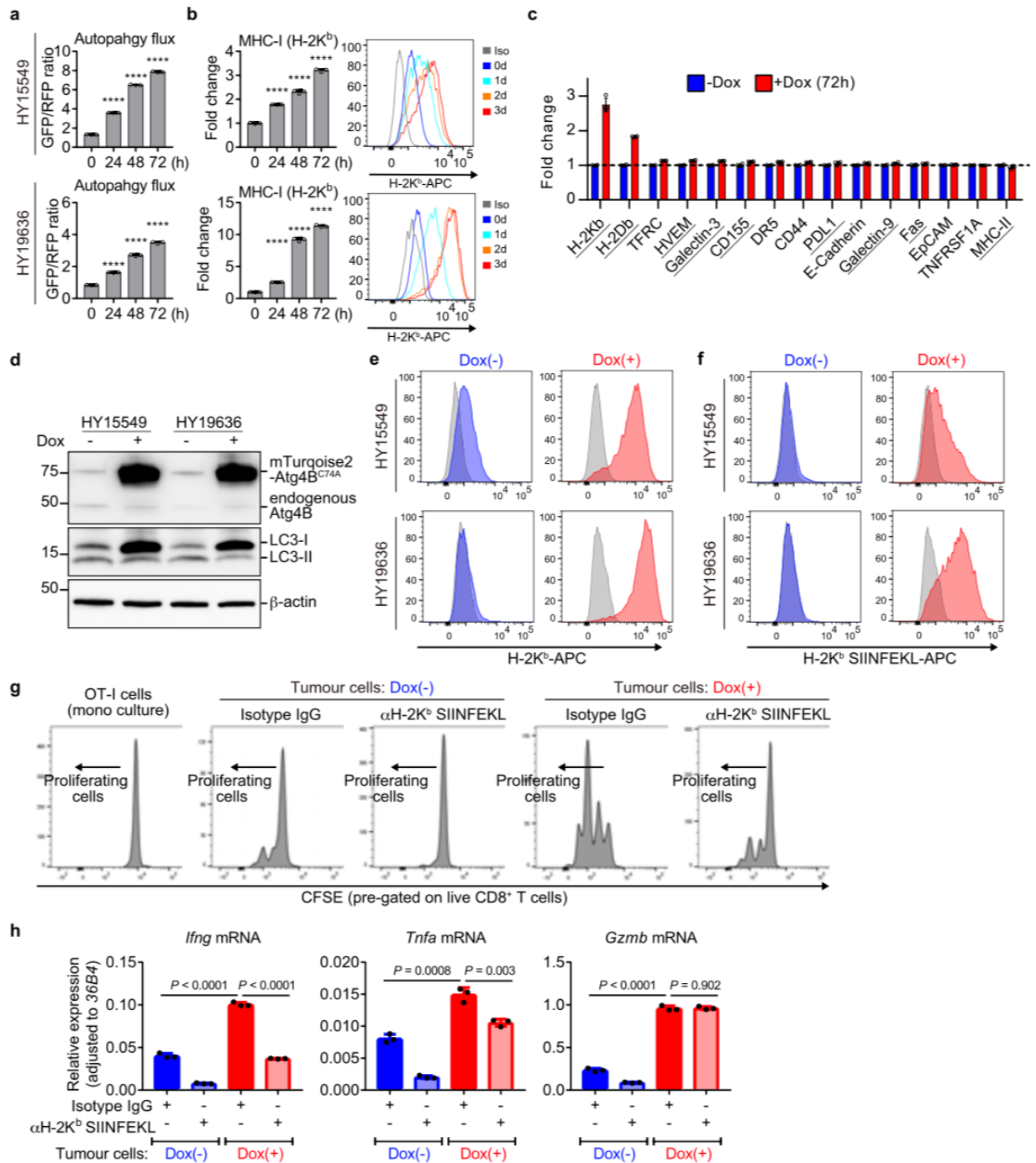


**Extended Data Figure 2.3e. Inhibition of macroautophagy, but not LAP/LANDO, restores MHC-I levels.** Knockdown mediated by shRNA (A–J) or siRNA (K, L) of FIP200, ATG14, ATG13 and ULK1, but not RUBICON, increased MHC-I levels in PDAC cells. **A, D, G, I, K,** Knockdown efficiency was confirmed by immunoblot (A, I, K) and qPCR (D, G). Data are mean  $\pm$  s.d. from three biological replicates per group (D, G). **A, E,** Whole-cell abundance of MHC-I was assessed by immunoblot. **C,** Immunofluorescence staining of MHC-I (green) and LAMP2 (red). Scale bars, 50  $\mu$ m. **B, F, H, J, L,** Cell-surface MHC-I levels were measured by flow cytometry (B, F,  $n = 9$ ; H, J,  $n = 12$ ; L,  $n = 16$ ). Data are pooled from at least three independent experiments. Data are mean  $\pm$  s.d. **A–F,** PaTu8902 cells (human). **G–L,** HY15549 cells (mouse). A representative of at least two independent experiments is shown in A, C, E, I and K.  $P$  values determined by unpaired two-tailed  $t$ -tests. See Supplementary Figure 1 for gel source data.



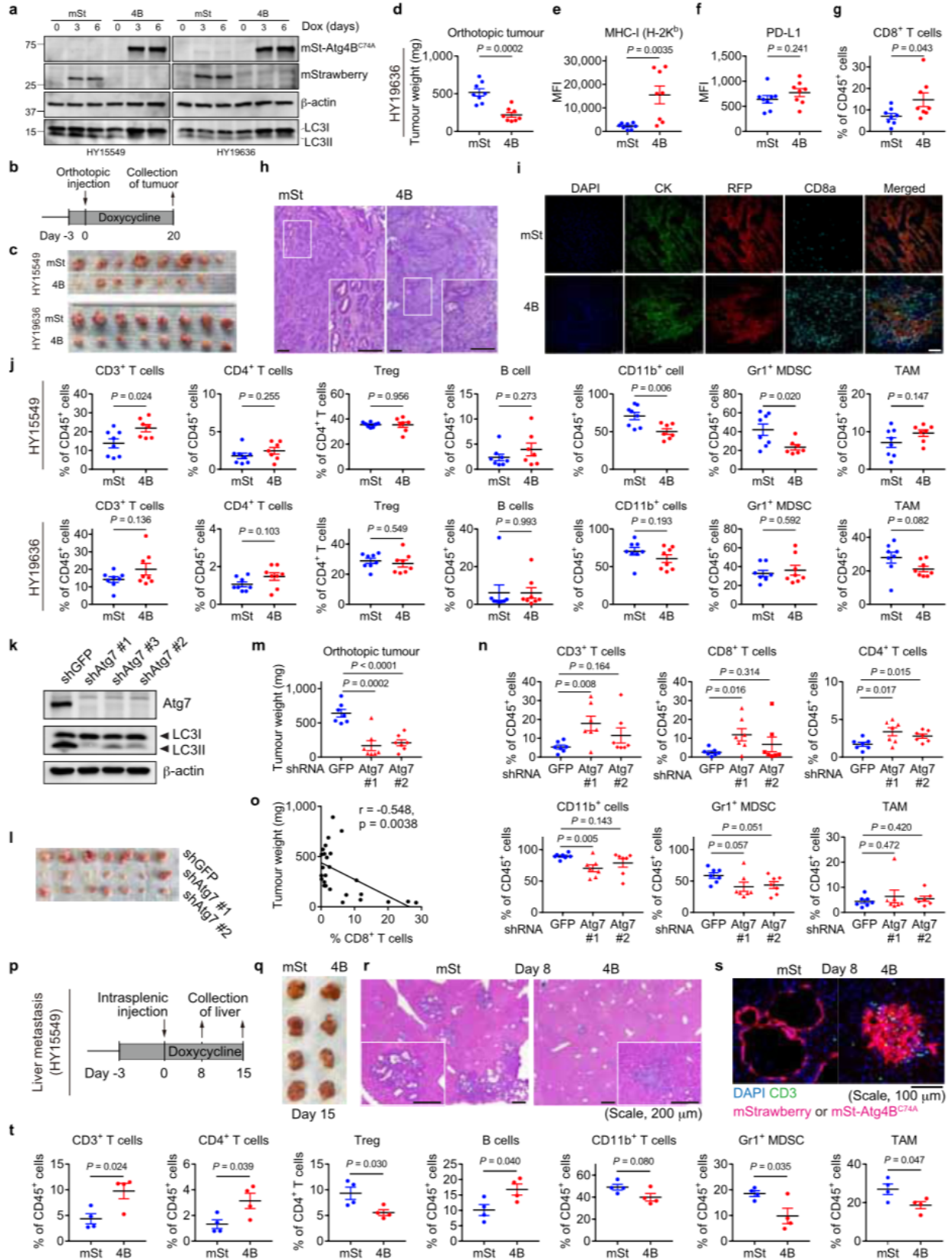
**Extended Data Figure 2.4e. The UBA domain of NBR1 is required for interaction with MHC-I.** **A**, Proximity-dependent biotinylation catalyzed by HLA-A-TrID. After addition of biotin, TurboID catalyzes the formation of biotin-5'-AMP anhydride, which enables covalent tagging of endogenous proteins with biotin within a few nanometers of the ligase. Related to Figure 2c. **B**, HLA-A-TrID was stably expressed in KP4 cells. Cells were treated with 10  $\mu$ M of exogenous biotin for 30 min. After labelling, cells were lysed and biotinylated proteins were enriched with streptavidin conjugated beads. Biotinylated proteins were detected using streptavidin-HRP (**B**) or with antibodies against the indicated proteins (see Fig. 2c). Asterisks indicates ligase self-biotinylation. **C**, Endogenous ubiquitylated proteins were affinity captured from PaTu8902 cells with UBQLN1 UBA conjugated beads. Treatment of affinity captured samples for 1 h with

purified Usp2-cc (+) to induce deubiquitylation leads to loss of ubiquitylation. Related to Figure 2e. **D**, PaTu8902 cells stably expressing wild-type NBR1 (GFP–NBR1,  $n = 19$  fields) or lacking the UBA domain (GFP–NBR1 dUBA,  $n = 16$  fields) were co-stained for endogenous LC3B. Graph shows quantification of the percentage co-localization. Box-and-whisker plots as in Fig. 1. Scale bars, 20  $\mu\text{m}$  (inset 10  $\mu\text{m}$ ). Related to Figure 2f. **E**, Effect of NBR1 knockdown on respective HLA-A, -B and -C levels in PaTu8902 cells. Note that blotting images for NBR1 and tubulin are the same as in Figure 2g. **F**, Immunofluorescence staining of MHC-I after NBR1 knockdown. Scale bars, 50  $\mu\text{m}$ . A representative of at least three independent experiments is shown in **B**, **C**, **E**, **F**. See Supplementary Fig. 1 for gel source data.

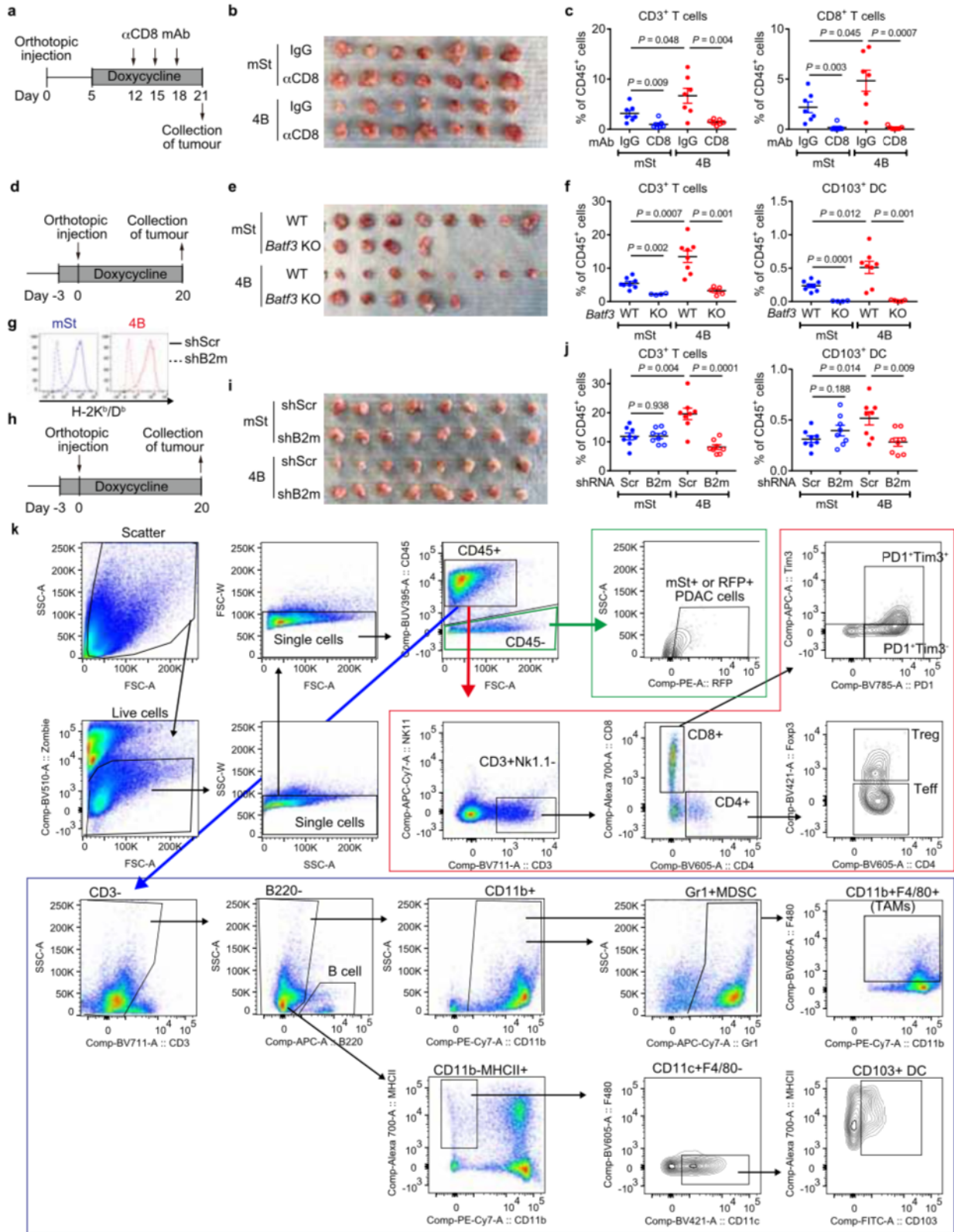


**Extended Data Figure 2.5e. Autophagy inhibition restores MHC-I expression, leading to enhanced anti-tumor T cell response in vitro.** **A, B,** Autophagy flux (**A**) and cell-surface MHC-I levels (**B**) in PDAC cells measured by flow cytometry. Mouse PDAC cells expressing the GFP–LC3–RFP reporter and Dox-inducible mTurquoise2-ATG4B(C74A) were grown as organoids for 8 days and treated with Dox (1  $\mu\text{g ml}^{-1}$ ) for the indicated hours. **A,** Autophagy flux represented by GFP/RFP ratio. Note that

increased GFP/RFP ratio indicates reduced autophagy flux. **B**, Cell surface MHC-I (H-2K<sup>b</sup>) levels. Representative flow cytometry plots are shown. Data are mean  $\pm$  s.d.  $n = 3$  biological replicates. Data are representative of at least four independent experiments. **C**, Fold changes of respective molecules on the cell surface quantified by flow cytometry. HY15549 cells expressing Dox-inducible mTurquoise2-tagged ATG4B(C74A) were grown as organoids for 8 days and treated with or without Dox ( $1 \mu\text{g ml}^{-1}$ ) for 72 h. Positive surface expression of each molecule was confirmed using respective isotype controls. Molecules found in immunological synapses are underlined. TFRC, transferrin receptor. independent experiments are shown. **D–F**, Mouse PDAC cells expressing OVA and carrying Dox-inducible mTurquoise2-ATG4B(C74A) were grown as organoids and treated with or without Dox ( $1 \mu\text{g ml}^{-1}$ ) for 96 h. Related to Figure 3a, b. **D**, Autophagy inhibition was confirmed by immunoblot. mTurquoise2-ATG4B(C74A) or endogenous ATG4B were detected by anti-ATG4B antibody. **E, F**, Flow cytometry plots for H-2K<sup>b</sup> (**E**) and H-2K<sup>b</sup>-SIINFEKL (**F**). Representative plots from Figures 3a, b are shown. Grey, isotype control. **G**, Representative flow cytometry plots of the OT-I cells co-cultured with mouse PDAC cells from Figure 3c. **H**, Quantitative reverse transcription PCR (qRT-PCR) analysis of OT-I cells that were co-cultured with PDAC cells for 48 h. Related to Figure 3c. Data are mean  $\pm$  s.d.  $n = 3$  biological replicates. For **G** and **H**, Dox(+) or Dox(-) indicates that PDAC cells were grown with or without Dox ( $1 \mu\text{g ml}^{-1}$ ) before co-culture. Dox was not added in co-culture. A representative of at least three independent experiments is shown in **D–G**. \*\*\*\* $P < 0.0001$ , unpaired two-tailed  $t$ -tests. See Supplementary Figure 1 for gel source data.

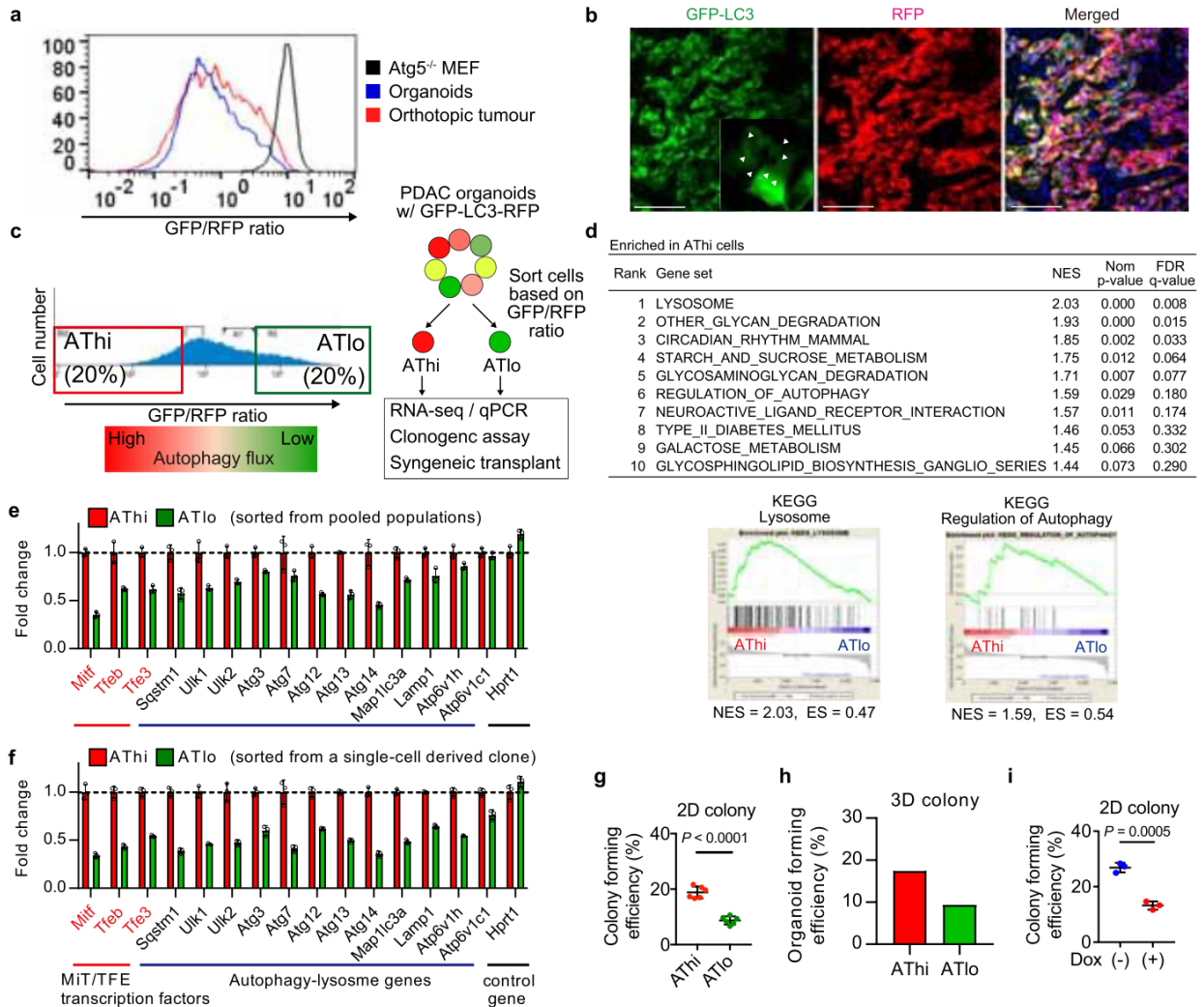


**Extended Data Figure 2.6e. Autophagy inhibition modulates anti-tumor immunity in both orthotopic and liver metastasis.** **A**, Immunoblots showing autophagy inhibition in mSt-ATG4B(C74A)-expressing cells. Mouse PDAC cells carrying Dox-inducible mSt or 4B were treated with Dox ( $1 \mu\text{g ml}^{-1}$ ) for the indicated days. mSt or mSt-ATG4B(C74A) was detected by anti-RFP antibody. A representative of two independent experiments is shown. **B–J**, Related to Figure 3e–h. Mouse PDAC cells shown in **A** were orthotopically transplanted into syngeneic (C57BL/6) mice. HY15549 cells (mSt,  $n = 8$ ; 4B,  $n = 7$ ) and HY19636 cells ( $n = 8$  per group) were injected. **B**, Study design. **C**, Images of tumors at end point. **D–G**, HY19636 tumor weight (**D**), cell surface MHC-I levels (**E**) and PD-L1 levels (**F**) on PDAC cells and tumor-infiltrating CD8<sup>+</sup> T cells (**G**) measured by flow cytometry. **H, I**, Representative H&E staining (**H**) and immunofluorescent staining (**I**) of HY15549 tumors (mSt,  $n = 8$ ; 4B,  $n = 7$ ). Scale bars, 100  $\mu\text{m}$ . **J**, Quantification of tumor-infiltrating immune cells by flow cytometry (HY15549,  $n = 8$  and 7; HY19636,  $n = 8$  per group). Gating strategies are shown in Extended Data Figure 7k and Supplementary Table 2. MDSC, myeloid-derived suppressor cells; Treg, T regulatory cells; TAM, tumor-associated macrophages. **K–O**, Autophagy-inhibition by shRNA-mediated ATG7 knockdown elicits similar anti-tumor T cell responses. **K**, Immunoblots for ATG7, LC3 and  $\beta$ -actin in PDAC cells (HY15549) expressing shRNAs against GFP or ATG7. A representative of at least two independent experiments is shown. **L–O**, Mouse PDAC cells shown in **K** were orthotopically transplanted into syngeneic mice ( $n = 7$  per group). **L**, Images of tumors collected on day 22. **M**, Tumor weight. **N**, Tumor-infiltrating immune cells as measured by flow cytometry. **O**, Correlation between CD8<sup>+</sup> T cell frequency among CD45<sup>+</sup> cells and tumor weight. **P–T**, Related to Figure 3i–l. Autophagy inhibition modulates anti-tumor immunity in metastatic tumors in the liver. Mouse PDAC cells (HY15549) carrying Dox-inducible mSt or 4B were injected into the spleen of syngeneic (C57BL/6) mice that were pre-fed with a Dox-containing diet ( $n = 4$  per group). PDAC cells were pre-treated with Dox ( $1 \mu\text{g ml}^{-1}$ ) for 7 days before injection. **P**, Study design. **Q**, Images of the liver. **R, S**, Representative images of H&E staining (**R**) and immunofluorescent staining (**S**) ( $n = 4$  per group). Scale bars, 200  $\mu\text{m}$  (**R**) and 100  $\mu\text{m}$  (**S**). **T**, Quantification of immune cells in the liver metastasis as measured by flow cytometry. Data are mean  $\pm$  s.e.m.  $n$  indicates individual mice.  $P$  values were determined by unpaired two-tailed  $t$ -tests (**D–G, J, M, N, T**) and Pearson correlation analysis (**O**). See Supplementary Figure 1 for gel source data.



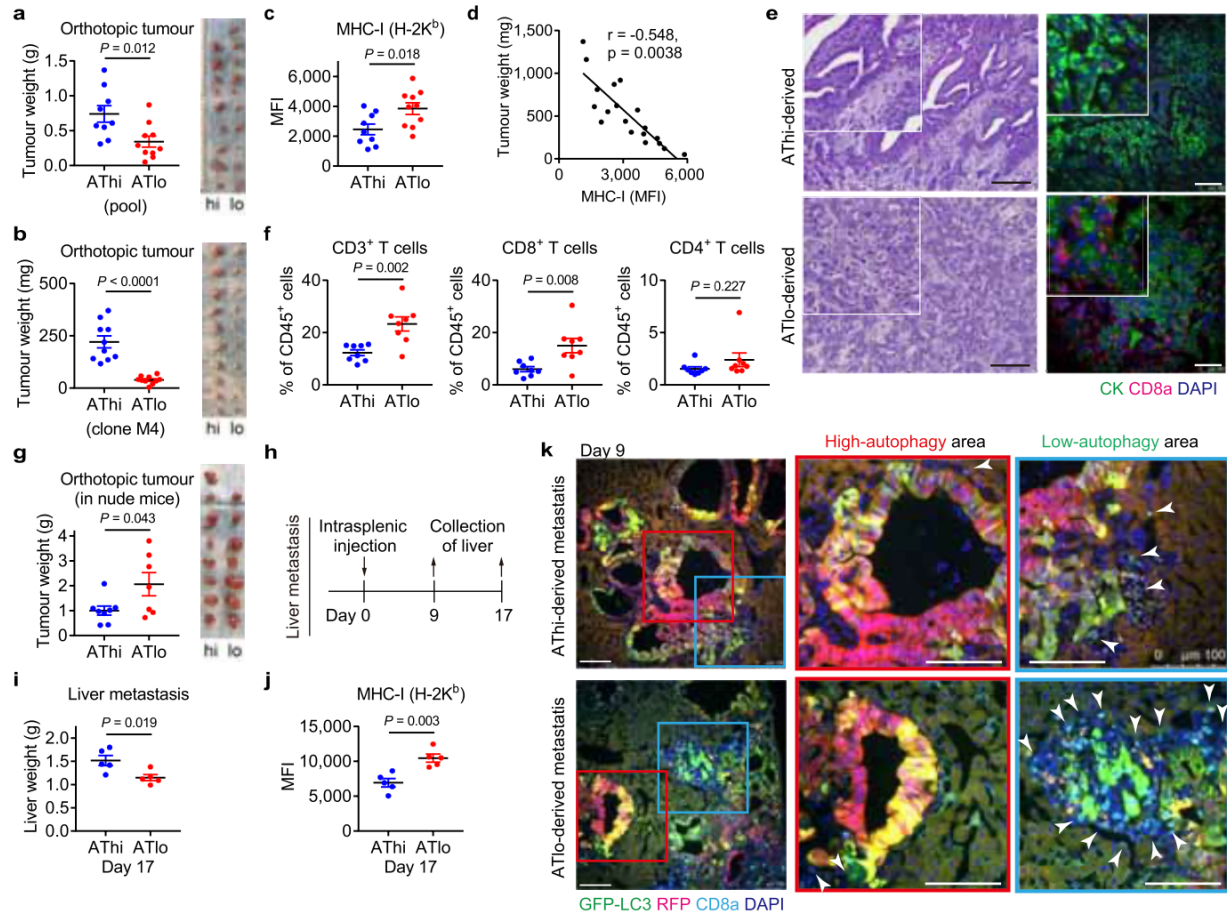


**Extended Data Figure 2.7e. Tumor regression after autophagy inhibition is rescued by depletion of CD8+ T cells or ablation of cell surface MHC-I.** **A–C**, Related to Figure 3m. HY15549 cells with Dox-inducible mSt or 4B were orthotopically injected into C57BL/6 mice and fed with Dox-containing diet starting on day 5, and then received intraperitoneal injection of anti-CD8 or isotype control IgG ( $n = 7$  per group). **A**, Study design. **B**, Images of tumors. **C**, Tumor-infiltrating leukocytes as quantified by flow cytometry. **D–F**, Related to Figure 3n, o. HY15549 cells with Dox-inducible mSt or 4B were orthotopically injected into C57BL/6 mice (WT) or *Batf3*<sup>-/-</sup> mice (KO) ( $n = 8, 4, 8$  and 5). **D**, Study design. **E**, Images of tumors. **F**, Quantification of tumor-infiltrating leukocytes by flow cytometry. **G–J**, Related to Figure 3p–r. HY15549 cells carrying Dox-inducible mSt or 4B were stably transfected with lentiviral vectors expressing control shRNA (shScr, solid line) or shRNA against B2m (shB2m, dashed line). **G**, Cell surface MHC-I as measured by flow cytometry. Cells were treated with IFN $\gamma$  (200 U ml<sup>-1</sup>) for 24 hours before flow cytometry analysis. Representative data from three independent experiments are shown. **H–J**, Cells shown in **G** ( $4 \times 10^4$  cells) were orthotopically transplanted into syngeneic (C57BL/6) mice that were pre-fed with Dox diet ( $n = 8$  per group). **H**, Study design. **I**, Images of tumors. **J**, Tumor-infiltrating leukocytes as quantified by flow cytometry. **K**, Gating strategies for flow cytometry analysis of tumors used in this study. See also Supplementary Table 2. Data are mean  $\pm$  s.e.m.  $n$  indicates individual mice.  $P$  values determined by unpaired two-tailed  $t$ -tests.



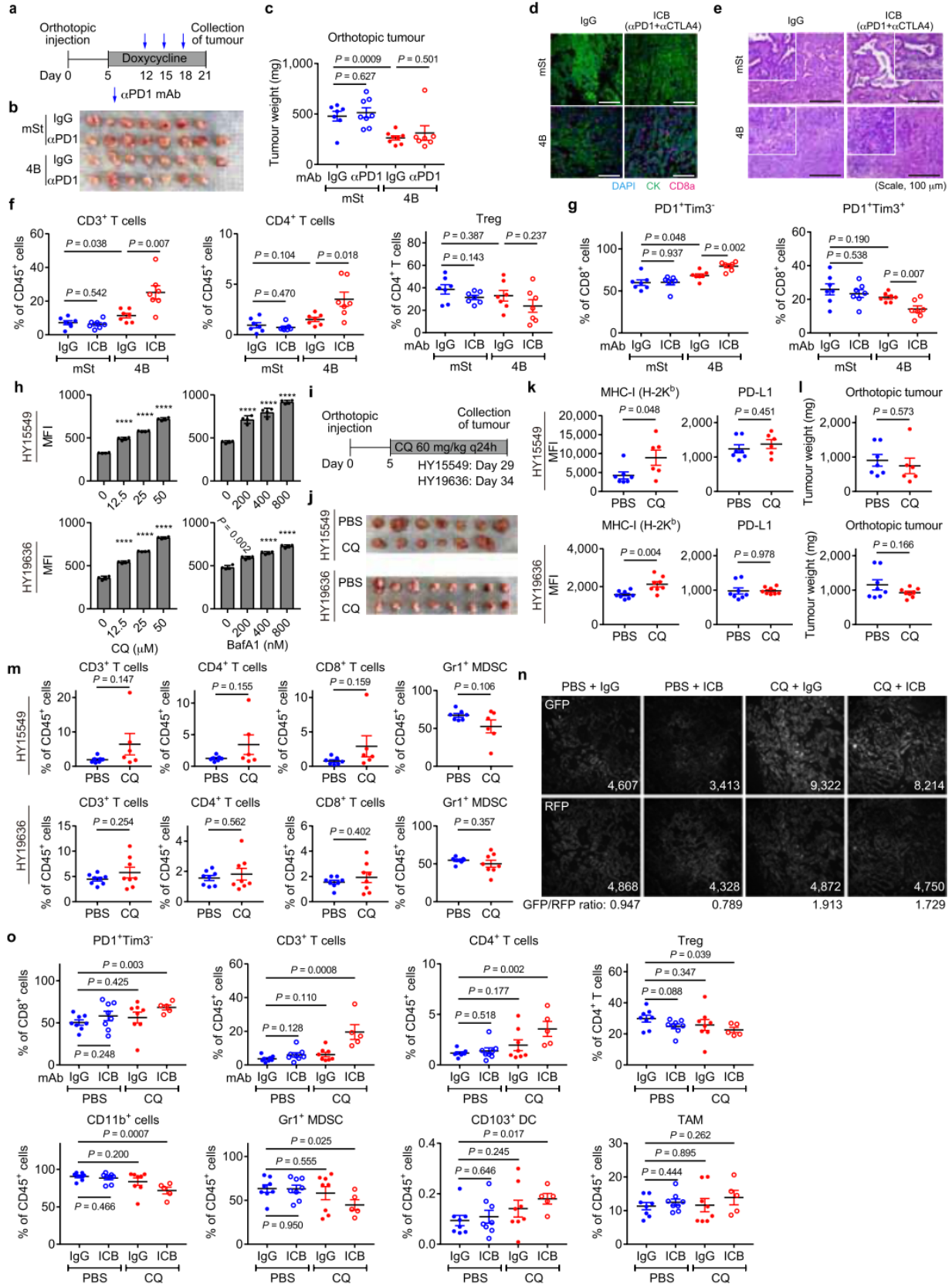
**Extended Data Figure 2.8e. Separation of PDAC cells with distinct autophagy flux using the GFP-LC3-RFP reporter.** Heterogeneity in basal autophagy flux was explored using mouse PDAC cells (HY15549) expressing the GFP-LC3-RFP reporter. **A, B**, HY15549 cells were grown as organoids or transplanted into C57BL/6 mice to form orthotopic tumors. **A**, Autophagy flux, as represented by GFP/RFP ratio, was measured by flow cytometry. *Atg5*<sup>-/-</sup> mouse embryonic fibroblasts (MEF) with the GFP-LC3-RFP reporter (black) was used as a control. Representative flow plots from three independent experiments are shown. **B**, Representative fluorescent images of orthotopic tumors. Cells with high autophagy flux show GFP-LC3 puncta formation (inset, arrowhead) and a decrease in total GFP-fluorescent signals, displaying red appearance in the merged image. Scale bars, 100  $\mu$ m. **C-H**, Mouse PDAC organoids were dissociated into single cells and sorted into autophagy-high (ATHi) or -low (ATLo) cells according to the GFP/RFP ratio. **C**, Sorting strategies. **D**, Top KEGG pathways enriched in ATHi cells compared to ATLo cells. Gene set enrichment analysis (GSEA) was performed using RNA sequencing (RNA-seq) data from sorted ATHi and ATLo cells ( $n = 2$  and 3 biologically independent

samples), showing enrichment of the autophagy–lysosome gene signatures in AThi cells as compared with the ATlo cells. FDR, false discovery rate; NES, normalized enrichment score; Nom., nominal. **E, F**, Relative mRNA expression of autophagy and lysosome-related genes in the respective populations sorted from pooled populations (**E**) or a single-cell derived clone (**F**).  $n = 3$  technical replicates. Representative results from four (**E**) and two (**F**) independent sorting experiments are shown. **G–I**, Clonogenic potential of sorted AThi and ATlo cells (**G, H**) and PDAC cells with Dox-inducible ATG4B(C74A) (AY6284) (**I**). Representative data from at least two independent experiments are shown.  $n = 4$  (**G**) and  $n = 3$  (**I**) per group. Data are mean  $\pm$  s.d. (**E–I**).  $P$  values were determined by unpaired two-tailed  $t$ -tests.



**Extended Data Figure 2.9e. Basal autophagy flux determines immunogenicity of PDAC cells.** Mouse PDAC cells (HY15549) expressing the GFP–LC3–RFP reporter were sorted into ATThi and ATlo cells (Extended Data Fig. 8c) and injected into the pancreas (A–G) or the spleen (H–K) of C57BL/6 mice (A–F, H–K) or nude mice (G). Cells were sorted from pooled populations except for (B). **A, B**, Tumor weight on day 21. ATThi and ATlo cells were sorted from either pooled populations (A) ( $n = 9$  and  $10$ ) or a single-cell derived clone (B) ( $n = 10$  per group). **C–E**, Tumors shown in A were analyzed. **C**, Cell surface MHC-I levels on PDAC cells measured by flow cytometry. **D**, Correlation between MHC-I levels on PDAC cells and tumor weight. **E**, Representative images of H&E (left) and immunofluorescent staining (right). Scale bars,  $100 \mu\text{m}$ . **F**, Quantification of tumor-infiltrating immune cells by flow cytometry ( $n = 8$  per group). Orthotopic tumors obtained on day 21 were analyzed. **G**, Orthotopic tumors in nude mice obtained on day 19 ( $n = 8$  and  $7$ ). **H–K**, Liver metastasis model. **H**, Study design. **I, J**, Weight of livers (i) and cell surface MHC-I levels on PDAC cells measured by flow cytometry (J) on day 17 ( $n = 5$  per group). **K**, Representative immunofluorescence images of livers obtained on day 9 ( $n = 3$  per group). Frozen sections were stained with anti-CD8a antibody and DAPI. In these merged images, cells with high autophagy flux appear as red, reflecting the relative loss of GFP-fluorescence and lower GFP/RFP ratio, whereas cells with low autophagy flux

appear as yellow to green, reflecting high GFP/RFP ratio. In the enlarged images, CD8a<sup>+</sup> cells were indicated by white arrowheads. Scale bars, 100  $\mu$ m. For **A**, **C–F** and **I–K**, experiments were performed at least twice and representative data of one experiment are shown. Data are mean  $\pm$  s.e.m. (**A–C**, **F**, **G**, **I**, **J**). *n* indicates individual mice. *P* values were determined by unpaired two-tailed *t*-tests (**A–C**, **F**, **G**, **I**, **J**) and Pearson correlation analysis (**D**).



**Extended Data Figure 2.10e. Autophagy inhibition synergizes with dual ICB. A–C,** Anti-PD1 antibody treatment did not affect tumor growth in either control or autophagy-inhibited tumors. Mice bearing orthotopic PDAC tumors (HY15549) carrying Dox-inducible mSt or 4B were treated with Dox beginning on day 5 and received either isotype control IgG or anti-PD1 antibody ( $n = 7, 8, 8$  and  $7$  per group). **A,** Study design. **B, C,** Images (**B**) and weight (**C**) of tumors. **D–G,** Related to Fig. 4a–d. Mice bearing orthotopic PDAC tumors (HY15549) expressing Dox-inducible mSt or 4B were treated with Dox beginning on day 5 and received either isotype control IgG or dual ICB (anti-PD1 and CTLA4 antibodies) ( $n = 7$  per group). **D, E,** Representative images of immunofluorescence staining (**D**) and H&E staining **E**. Scale bars,  $100 \mu\text{m}$ . **F, G,** Quantification of tumor-infiltrating immune cells by flow cytometry. **H,** Cell surface MHC-I (H-2K<sup>b</sup>,D<sup>b</sup>) levels measured by flow cytometry. Mouse PDAC cells were treated with chloroquine or BafA1 at the indicated concentrations for 48 h ( $n = 4$ ). Mouse PDAC cells were grown in 2D culture (chloroquine) or as organoids (BafA1). Representative results from at least three independent experiments are shown. **i–m,** Mice bearing orthotopic PDAC tumors expressing the GFP–LC3–RFP reporter were treated with PBS or chloroquine beginning on day 5 ( $n = 7$  vs  $6$  for HY15549 and  $n = 8$  vs  $8$  for HY19636). **i,** Study design. **j,** Images of tumors. **k,** Cell surface MHC-I and PD-L1 levels on PDAC cells measured by flow cytometry. **l,** Tumor weight. **m,** Quantification of tumor-infiltrating immune cells by flow cytometry. **n,** Representative fluorescence images of tumors expressing the GFP–LC3–RFP reporter from Fig. 4j. Numerical values represent mean fluorescent intensity of each field. **o,** Quantification of tumor-infiltrating immune cells by flow cytometry ( $n = 8, 8, 8$  and  $5$ ; left to right). Tumors in Fig. 4k were analyzed. Data are mean  $\pm$  s.e.m. (**c, f, g, k–m, o**) or  $\pm$  s.d. (**h**).  $n$  indicates individual mice (**c, f, g, k–m, o**) or biological replicates (**h**). Except for the orthotopic implantation of HY19636 cells (**j–m**), all experiments were performed at least twice and representative data of one experiment are shown. \*\*\*\* $P < 0.0001$ , unpaired two-tailed  $t$ -tests.

## Materials and Methods

### Cell culture

The cell lines PaTu-8988T, KP4, MiaPaca2, Panc 2.03, PaTu-8902, Panc1, AsPc1, HupT3 and A549 were obtained from the American Type Culture Collection (ATCC) or the DSMZ. H441, H358, HCT116 and BEAS-2B were provided by E. Collisson. HPDE was provided by M. Tsao (Liu et al., 1998). Cells were cultured in the following media: PaTu-8988T, KP4, MiaPaca2, PaTu-8902, Panc1, AsPc1 and BEAS-2B in DMEM supplemented with 10% FBS; Panc 2.03 and HupT3 in RPMI with 10% FBS; HPDE cells were cultured in keratinocyte serum-free (KSF) medium supplemented by epidermal growth factor and bovine pituitary extract (Life Technologies, Inc.), supplemented with 1% penicillin and streptomycin (Gibco). Cell lines were regularly tested and verified to be mycoplasma negative using Myco- Alert Detection Kit (Lonza) or via PCR.

Primary mouse PDAC cell lines were established from pancreatic tumors in respective GEMMs as described previously (Yang et al., 2018). HY15549 and HY19636 cells were established from female KPC mice ( $p48\text{-cre}^+$  ( $p48$  is also known as  $Ptf1a$ )  $Kras^{LSL-G12D/+}$ ,  $Trp53^{lox/+}$ ) (Bardeesy et al., 2006) that were fully back-crossed into a C57BL/6 background. The other cell lines were derived from the following mice (Yang et al., 2014, 2018):  $Atg5^{+/+}$  KPC cells,  $Pdx1\text{-cre}^+$ ,  $Kras^{LSL-G12D/+}$ ,  $Trp53^{lox/+}$ ,  $Atg5^{+/+}$  mice;  $Atg5^{-/-}$  KPC cells,  $Pdx1\text{-cre}^+$ ,  $Kras^{LSL-G12D/+}$ ,  $Trp53^{lox/+}$ ,  $Atg5^{lox/lox}$  mice; AY6284 cells,  $p48\text{-cre}^+$ ,  $Kras^{LSL-G12D/+}$ ,  $Trp53^{lox/+}$ ,  $Rosa^{LSL-rtTA}$ , mSt-ATG4B(C74A) mice (Yang et al., 2018). All mouse PDAC cells were maintained in DMEM (Corning) supplemented with 10% FBS (Atlanta Biologicals, S11550H) and 1% penicillin and streptomycin (Gibco).



Cells were grown in a humidified incubator with 5% CO<sub>2</sub> at 37° C. Cultures were routinely verified to be negative for mycoplasma. Cell lines were authenticated by fingerprinting, and low passage cultures were carefully maintained in a central lab cell bank.

## **Constructs**

GFP–NBR1 and GFP–NBR1 dUBA were provided by J. Debnath. LysoTag TMEM192-mRFP-3xHA (TMRHA) was generated by subcloning the cDNA of TMEM192 (Origene) together with monomeric red fluorescent protein (mRFP) and 3× haemagglutinin (HA) tag into the NheI and EcoRI sites of pLJM1 lentiviral vector. HLA-A-TurboID-Flag (HLA-A–TrID) was generated by subcloning the cDNA of HLA-A (Addgene plasmid, 85162) into the EcoRI and NotI sites of the TurboID pLVX vector (gift from R. Zoncu). pMXs GFP–LC3–RFP was a gift from N. Mizushima (Addgene, plasmid 117413). For Dox-inducible expression of ATG4B(C74A), mTur-quoise2 or mStrawberry was fused to ATG4B(C74A) and inserted into either pSLIK-Hygro (used for in vitro studies) (Addgene, plasmid 25737) or pINDUCER20 (used for in vivo studies) (Addgene, plasmid 44012), using the Gateway Cloning system (Thermo Fisher Science). For the generation of OVA-expressing cells, the cOVA fragment was cloned from pCI-neo-cOVA (Addgene, plasmid 25097), fused with 2A peptide and mStrawberry sequences using NEBuilder HiFi DNA Assembly Cloning Kit (New England BioLabs) according to manufacturer’s instruction, and inserted into the EcoRI and Sall sites of pBabe-zeo (Addgene, plasmid 1766) to generate pBabe-cOVA-2A-mStrawberry. Stable cOVA expression was confirmed and monitored with mStrawberry fluorescence.

## shRNAs

shRNA vectors (pLKO.1 puro) were obtained from the Sigma MISSION TRC shRNA library. The sequences and RNAi Consortium clone IDs for the shRNAs used are as follows:

shATG3#1 (human): 5'-GATGTGACCATTGACCATATT-3' (TRCN00001 48120);  
shATG3#2 (human): 5'-GCTGTCATTCCAACAATAGAA-3' (TRCN0000147381);  
shATG7#1 (human): 5'-CCCAGCTATTGGAACAC TGTA-3' (TRCN0000007587);  
shATG7#2 (human): 5'-GCCTGCTGAG GAGCTCTCCAT-3'(TRCN0000007584);  
shNRB1#1(human):5'-GCTTCAT AGTTATTTGGCATT-3' (TRCN0000123159);  
shNBR1#2 (human): 5'-GCAGCATTTGTGGATGAGAAT-3' (TRCN0000123160);  
shNBR1#3 (human): 5'GCCAGGAACCAAGTTTATCAA-3' (TRCN0000123161);  
shFIP200#1 (human): 5'- GCACTCTTTAACACATTCTTT-3' (TRCN0000 013523);  
shFIP200#2 (human): 5'- GCTGTGAATGAGTTTGTAATA-3' (TRCN0000013524);  
shATG14#1 (human): 5'-CCATAGAACTTGGTCA TGTTT-3' (TRCN0000144080);  
shATG14#2 (human): 5'-GATCAATTAC AACCACTGCAT-3' (TRCN0000145367);  
shAtg3#1 (mouse): 5'-CATATCA CAACACAGGTATTA-3' (TRCN0000247440);  
shAtg3#2 (mouse): 5'- GTACATCACTTACGACAAATA-3' (TRCN0000247442);  
shAtg7#1 (mouse): 5'-TTCTGTCACGGTTCGATAATG-3' (TRCN0000305991);  
shAtg7#2 (mouse): 5'- GCCAACATCCCTGGATACAAG-3' (TRCN0000 375444);  
shAtg7#3 (mouse): 5'- TCTTACCCTGCTCCATCAAGA-3' (TRCN0000375421);  
shB2m (mouse): 5'-CCAGTTTCTAATATGCTATAC-3' (TRCN0000295705);  
shAtg13#1 (mouse): 5'-TGAAGTCTCTTCTCGCT ATTA-3' (TRCN0000277121);

shAtg13#2 (mouse): 5'-GACATACCTTTTCG CCATGTTT-3' (TRCN0000176029);  
shUlk1#1 (mouse): 5'-CGCTTCTTT CTGGACAAACAA-3' (TRCN0000319764),  
shUlk1#2 (mouse): 5'-CGCTT CTTTCTGGACAAACAA-3' (TRCN0000028768);  
shGFP: 5'-TGCCCGACA ACCACTACCTGA-3' (TRCN0000072186). shGFP and shScr  
(Addgene, plasmid #17920) were used as controls.

### **siRNAs**

The short interfering RNAs (siRNAs) used in this study are: siNC (silencer negative control #1 siRNA, Thermo, 13778030), siRubicon #1 (s104762, Ambion), and siRubicon #2 (s104763, Ambion). Cells were transfected with siRNAs using Lipofectamine RNAi Max Transfection Reagent (Life Technologies).

### **Retroviral and lentiviral transduction**

For the transfection of pMXs GFP-LC3-RFP (Zaizuka et al., 2016) and pBabe-cOVA- 2A-mStrawberry, retrovirus was produced by co-transfection of HEK293FT cells with a retroviral vector and the packaging plasmids pHit60 and VSVG at a 0.5:0.25:0.25 ratio. For the transfection of lentiviral vectors (pSLIK-hygro, pINDUCER20 and pLKO.1-puro), lentivirus was produced by co-transfection of HEK293FT cells with a lentiviral vector and the packaging plasmids psPAX2 (Addgene, plasmid 12260) and pMD2.G (Addgene, plasmid 12259) at a 0.5:0.25:0.25 ratio. Transfection was performed using Lipofectamine 3000 Reagent (Thermo Fisher Scientific) according to manufacturer's instructions. The viral supernatant was collected 48 h after transfection, filtered through a 0.45- $\mu$ m filter, and used for infection together with Polybrene reagent (EMD Millipore). Cells expressing

Dox-inducible constructs were sorted for positive fluorescent expression after Dox treatment to select inducible cells, and then sorted for no fluorescent expression after Dox withdrawal to remove cells with leaking expression, as described previously (Pommier et al., 2018).

### **Immunofluorescence**

Human cell lines were cultured for two days on coverslips coated with fibronectin. After two PBS washes, cells were fixed and permeabilized with 4% paraformaldehyde in PBS for 15 min at room temperature or ice-cold methanol for 5 min at  $-20^{\circ}$  C. Paraformaldehyde-fixed cells were permeabilized with 0.1% saponin in PBS. Samples were then blocked with 5% normal goat serum for 15 min at room temperature before incubation with primary antibodies (Supplementary Table 1) overnight at  $4^{\circ}$  C. After washing three times with PBS, cells were incubated in secondary antibody at room temperature for 20 min. Slides were mounted on glass slides using DAPI Fluoromount-G (0100-20, SouthernBiotech) and imaged on a Zeiss Laser Scanning Microscope (LSM) 710 using a 63 $\times$  objective. Image processing and quantification were performed using ImageJ.

### **Lysosome immunoprecipitation**

For lysosome immunoprecipitation experiments, HPDE and human PDAC cell lines stably expressing TMRHA were ruptured and intact lysosomes from 1–2 mg of total protein per sample was immunoprecipitated using HA-conjugated Dynabeads as previously described (Zoncu et al., 2011; Abu-Remaileh et al., 2017).

### **Poly-ubiquilin UBA affinity capture**

Cells were washed twice with ice-cold PBS and lysed in lysis buffer (50 mM Tris-HCl pH 7.5, 150 mM NaCl, 1% NP-40, 10 mM *N*-ethylmaleimide) supplemented fresh with protease inhibitor cocktail. Lysates were incubated at 4° C for 15 min and clarified by centrifugation at 20,000 x g at 4° C for 15 min. Samples were quantified by BCA Protein Assay Kit and diluted to 1 mg ml<sup>-1</sup> with dilution buffer (50 mM Tris-HCl, pH 7.5, 150 mM NaCl, 5 mM EDTA, protease inhibitor). Approximately 1–1.5 mg of protein lysates were incubated with 50 µl of Ubiquilin 1 Tandem UBA Agarose (BostonBiochem AM-130) overnight at 4° C. Samples were then washed three times in High Salt Wash Buffer (50 mM Tris-HCl pH 7.5, 250 mM NaCl, 0.5% NP-40) and once with 10 mM Tris-HCl, pH 7.5. Samples were eluted by adding Laemmli buffer and incubating at 65° C for 15–20 min.

For DUB digestions, affinity captured material was washed once with DUB digestion buffer (50 mM Tris-HCl, pH 7.5, 150 mM NaCl, 20 mM dithiothreitol). Liquid was removed and beads were resuspended in 20 ml of DUB digestion buffer and 5 mg of USP2 catalytic domain (Usp2cc; BostonBiochem E-506) for 1 h with gentle shaking at 30° C. Beads were washed once in high-salt wash buffer and once with 10 mM Tris-HCl, pH 7.5, before eluting affinity captured material by adding Laemmli buffer and incubating at 65° C for 15 min.

### **Proximity biotinylation**

Human PDAC cells stably expressing HLA-A–TrID were cultured in DMEM supplemented with 10% dialyzed FBS (DMEM + dFBS) for 48 h. Cells were incubated with 10 µM biotin

(Sigma) and incubated at 37° C for 30 min. Media was replaced with DMEM + dFBS and incubated at 37° C for a further 2–3 h. For negative controls, we omitted exogenous biotin. Cells were then washed twice in ice-cold PBS and lysed in ice-cold lysis buffer (1% Triton X-100, 130 mM NaCl, 2.5 mM MgCl<sub>2</sub>, 2 mM EGTA, 25 mM HEPES pH 7.4, supplemented fresh with protease inhibitor cocktail) for 30 min on ice. Samples were clarified by centrifugation at 13,300 rpm for 10 min at 4° C. Protein content was measured using BCA Protein Assay Kit (Life Technologies 23227). Then, 1–2 mg of protein lysates were incubated with 50 µl of Dynabeads MyOne Streptavidin C1 (Life Technologies) overnight. The beads were washed twice in wash buffer 1 (2% SDS in distilled H<sub>2</sub>O), once in wash buffer 2 (0.1% deoxycholate, 1% Triton X-100, 500 mM NaCl, 1 mM EDTA, and 50 mM HEPES, pH 7.5), once in wash buffer 3 (250 mM LiCl, 0.5% NP-40, 0.5% deoxycholate, 1 mM EDTA, and 10 mM Tris, pH 8.1), and twice in wash buffer 4 (50 mM Tris, pH 7.4, and 50 mM NaCl). Washes were performed at room temperature for 5 min with gentle agitation. Samples were eluted in Laemmli buffer and boiled at 95° C. Quantification of biotinylation activity was measured as intensity of each lane in the ±biotin immune-precipitation condition divided by the corresponding intensity of the ligase expression band in the input. The +biotin ratios were then normalized to the –biotin control ratio and to background.

### **Organoid culture**

Normal pancreatic organoids from mice were established as previously described (Boj et al., 2015; Matsuura et al., 2019) with slight modifications. In brief, pancreas was harvested from female C57BL/6 mice (4–10 weeks of age), mechanically minced with

scissors, and digested with 1 mg ml<sup>-1</sup> collagenase P (Sigma), 4 mg ml<sup>-1</sup> Dispase II (Sigma), 10 mM HEPES (Thermo Fisher Scientific), 1% FBS, 1 mg ml<sup>-1</sup> Trypsin Inhibitor from Soybean (Sigma) in DMEM for 20 min at 37° C. Digested tissues were embedded in Matrigel (Corning, 356231) and cultured in Advanced DMEM (Thermo Fisher Scientific) supplemented with 200 mM l-glutamine (Thermo Fisher Scientific), 10 mM HEPES (Thermo Fisher Scientific), 1% Antibiotic-Antimycotic (Thermo Fisher Scientific), 500 ng ml<sup>-1</sup> recombinant mouse r-spondin-1 (Peprotech), 50 ng ml<sup>-1</sup> recombinant murine EGF (Peprotech), 100 ng ml<sup>-1</sup> recombinant mouse noggin (Peprotech), 1 μM jagged-1 (188-204) (AnaSpec, AS-61298), 100 μg ml<sup>-1</sup> trypsin inhibitor from soybean (Sigma), and 10 μM Y-27632 (Enzo). Two days before analysis, culture media was replaced with DMEM supplemented with 10% FBS. PDAC organoids were generated by embedding mouse PDAC cell lines in Matrigel and were grown in DMEM with 10% FBS. For the dissociation of organoids for further assays, organoids were digested with TrypLE (Thermo Fisher, A1217701) solution at a 2× concentration for 20 min at 37° C, followed by filtration through a 40-μm nylon strainer.

### **Quantitative proteomics**

Quantitative mass spectrometry-based proteomics was performed as previously described (Paulo et al., 2015; Biancur et al., 2017) based on the SL-TMT workflow (Navarrete-Perea et al., 2018). In brief, cells were lysed in a lysis buffer (200 mM HEPES pH 8.5, 8 M urea, 1x Complete Protease Inhibitor Cocktail (Roche), 1 × PhosStop (Roche)) and homogenized by passing through a 21-gauge needle. Lysates were collected by centrifuging at 20,000 x g for 5 min at 4° C, followed by disulfide bond

reduction with 5 mM dithiothreitol at 37° C for 25 min and alkylation with 10 mM iodoacetamide at room temperature for 30 min in the dark. Chloroform–methanol precipitation of protein was performed, followed by protease digestion in HEPES buffer (200 mM, pH 8.5). Each sample containing 100 µg protein was digested at a 1:100 protease-to-protein ratio with LysC protease at room temperature overnight, followed by digestion with trypsin at 37° C for 6 h. Approximately 50 µg of peptides from each sample was labelled with 100 µg TMT reagent which were dissolved in anhydrous acetonitrile to achieve a final concentration of 30% (v/v). TMT-labelled samples were acidified, vacuum centrifuged to near dryness and subjected to C18 SPE (Sep-Pak, Waters). Samples were subjected to basic pH reversed-phase HPLC. Data were obtained with Orbitrap Fusion mass spectrometer (Thermo Fisher Scientific) coupled with a Proxeon EASY-nLC 1000 LC pump (Thermo Fisher Scientific). Peptide separation was done using a custom Accucore C18 resin (2.6 µm, 100 Å, Thermo Fisher Scientific) column for 3 h using a gradient of 6–30% acetonitrile in 0.125% formic acid with a flow rate of 300 nl min<sup>-1</sup>. All analysis involved an MS<sup>3</sup>-based TMT method as previously mentioned (McAlister et al., 2014) and mass spectra were processed as described earlier (Paulo et al., 2015).

### **Tumor cell and OT-I cell co-culture experiment**

Mouse PDAC cells stably expressing OVA and carrying Dox-inducible mTurquoise2-ATG4B(C74A) were grown as organoids, treated with or without Dox (1 µg ml<sup>-1</sup>) for 96 h. Organoids were dissociated into single cells, which were then incubated with either anti-H-2K<sup>b</sup>-SIINFEKL antibody (clone 25-D1.16, BioXCell, BE0207) or isotype control (clone MOPC-21, BioXCell, BE0083) at 100 µg ml<sup>-1</sup> for 30 min at 4° C. Total splenocytes were



harvested from OT-I mice and CD8<sup>+</sup> T cells were enriched using Dynabeads Untouched Mouse CD8 Cells (Invitrogen, 11417D) following manufacturer's instructions. Isolated CD8<sup>+</sup> T cells were labelled with 10 μM CFSE (BioLegend) for 10 min at room temperature in the dark, washed three times with RPMI-1640 supplemented with 10% FBS. Ten thousand PDAC cells and forty thousand CD8<sup>+</sup> cells were seeded in 96-well plates and cultured in 100 μl 50% DMEM and 50% RPMI-1640 supplemented with 10% FBS, 10 ng ml<sup>-1</sup> recombinant murine IL-2 (Peprotech), 27.5 μM 2-mercaptoethanol (Gibco), and 100 μg ml<sup>-1</sup> of respective antibodies. After 48 h, CD8<sup>+</sup> T cells were harvested and stained with anti-CD8a antibody (AF647, clone 53-6.7, BioLegend) and DAPI, and proliferation was analyzed by CFSE dilution using flow cytometry. After removal of CD8<sup>+</sup> T cells, the viability of remaining PDAC cells was measured by CellTiter-Glo (Promega).

### **Clonogenic assay**

For 2D clonogenic assays (Yang et al., 2011), cells were plated in 6-well plates at 300 cells per well in 2 ml DMEM supplemented with 10% FBS. After 7 days, colonies were fixed with 80% methanol, stained with 0.2% crystal violet, and counted. For 3D clonogenic assay, single cells were sorted directly into 384-well round bottom Ultra-Low Attachment plates (Corning 3830) and grown in DMEM supplemented with 10% FBS and 2% Matrigel (Corning 356231). After 10 days, the number of wells with spheroids was counted.

### **Mice**

Female 8–10-week-old C57BL/6 mice or NCr nude (B6NTac, Taconic) mice were used for allograft experiments. OT-I transgenic mice (003831) and *Batf3*<sup>-/-</sup> mice (013755) were

purchased from Jackson Laboratory. All mice were bred and maintained in the animal facility of the New York University School of Medicine. All animal procedures were approved by the New York University School of Medicine Institutional Animal Care and Use Committee (IACUC) under protocol numbers IA16-00507 and IA16-01331.

### **Mouse experiments**

Orthotopic and intrasplenic injections of PDAC cells were performed as described previously (Sousa et al., 2016; Soares et al., 2014). In brief, mice were anaesthetized by an intraperitoneal injection of ketamine and xylazine. A small incision was made on the upper left quadrant of the abdomen, and either the pancreas or the spleen was externalized. For orthotopic injection, cells were suspended in 20  $\mu$ l of Matrigel (Corning 356231):HBSS (1:1) solution and injected into the pancreatic tail with insulin syringes (29-gauge needle, BD 324702). Approximately  $1 \times 10^4$  HY15549 cells or  $2 \times 10^4$  HY19636 cells were injected unless otherwise indicated. For intrasplenic injection,  $1 \times 10^6$  cells were suspended in 100  $\mu$ l HBSS and then drawn into an insulin syringe (28-gauge needle, BD 329461), which was pre-loaded with 200  $\mu$ l HBSS. The externalized spleen was divided by ligating clips (Teleflex, 002200), and cells were injected into the hemispleen. After injection, splenic vein was ligated with ligating clips (Teleflex, 001200) at the hilum of the spleen, and then the hemispleen was removed. After the procedures, the peritoneum was closed with a 3-0 VICRYL VIOLET suture (Ethicon, J311H), and the skin was closed using the BD AutoClip Wound Closing System (BD). For some experiments, mice were fed with Dox-containing diet ( $625 \text{ mg kg}^{-1}$ ) for the indicated period. Mice were

euthanized at the indicated time points and tumors or the liver were collected after trans-cardiac perfusion with PBS.

For CD8<sup>+</sup> T cell depletion, mice received intraperitoneal injection of anti-mouse CD8a antibody (200 µg, clone 53-6.7, BE0004-1) or isotype control (200 µg, clone 2A3, BE0089). For immune checkpoint blockade experiments, mice received intraperitoneal injection of anti-mouse PD-1 antibody (200 µg, clone RMP1-14, BE0146) and anti-mouse CTLA-4 antibody (200 µg, BE0131), or rat IgG2a isotype-matched control (200 µg, clone 2A3, BE0089) and polyclonal Syrian hamster IgG (200 µg, BE0087). All antibodies used in in vivo experiments were obtained from BioXCell. For chloroquine treatment, mice received intraperitoneal injection of chloroquine solution in PBS at 60 mg kg<sup>-1</sup> or PBS every day starting day 4 or 5 after tumor cell implantation. Mice were randomly assigned to specific treatment groups at the beginning of treatment.

All experiments were carried out in a clean conventional facility, where mice were housed in pre-packaged disposable irradiated cages, and fed with irradiated diet and acidified water. Microisolator cages were located on ventilated racks. No tumors in the mice exceeded IACUC-defined maximum diameters of >2 cm. Sample sizes were determined based on our preliminary experiments and no sample size calculation was done. Blinding was not performed as the investigator needed to know the treatment groups in order to perform study. Tumor weights (an objective measurement) were measured only at the study endpoints after mice were euthanized and tumors were harvested.

## Flow cytometry

For surface and intracellular MHC-I staining of human cell lines, cells were stained with Alexa Fluor 488-conjugated anti-human HLA-A, -B, -C antibody (BioLegend, clone W6/32) at a 1:75 dilution for 45 min at 4° C in the dark and washed with PBS plus 2% FBS and 2 mM EDTA (FACS buffer). Cells were then fixed and permeabilized before staining with phycoerythrin (PE)-conjugated anti-human HLA-A,-B,-C antibody (BioLegend, clone W6/32) at a 1:75 dilution for 45 min at room temperature and washed with FACS buffer. For cell surface molecule staining of mouse cells, single-cell suspensions were prepared as described above. Cells were washed with FCM buffer (HBSS containing 1% FBS, 1 mM EDTA, and 10 mM HEPES) and stained with antibodies (Supplementary Table 1) at 4° C in the dark for 20 min. Dead cells were depleted by DAPI staining.

For the immunophenotyping of tumors, tissues were mechanically minced with scissors, and then digested in DMEM containing 1 mg ml<sup>-1</sup> collagenase IV (Gibco), 100 µg ml<sup>-1</sup> DNase I (Roche), 1% FBS, 10 mM HEPES, 2% Antibiotic-Antimycotic (Thermo Fisher Scientific) for 40 min at 37° C in the dark with gentle agitation every 10 min. Digested tissues were then washed twice in DMEM containing 10% FBS, filtered through a 40-µm nylon mesh strainer (Corning). Cells were suspended in ACK Lysing Buffer (Thermo Fisher Scientific), incubated for 10 min at 4° C in the dark to remove red blood cells. Cells were washed twice in FCM buffer and counted. Cells were stained with Zombie Aqua Fixable Viability Kit (BioLegend) and blocked with anti-mouse CD16 and CD32 antibody (mouse BD Fc Block, clone 2.4G2, BD Bioscience). One million cells were incubated with

appropriate antibodies (Supplementary Table 1) diluted in FCM buffer at 4° C in the dark for 40 min. Cells were then washed twice with FCM buffer and analyzed or further fixed in 2% PL solution (PBS containing 0.1 M l-lysine (Sigma) and 2% paraformaldehyde (Ted Pella)) (Hirata et al., 2018) at 4° C in the dark overnight. Intracellular staining was performed using Foxp3/Transcription Factor Staining Buffer Set (eBioscience). Cells were analyzed on a BD LSR Fortessa or a BD LSR-II UV and analyzed by FlowJo software (FlowJo, LLC, v.10.4). Gating strategies were described in Extended Data Fig. 7k and Supplementary Table 2.

### **Cell sorting**

Mouse PDAC cells (HY15549) expressing the GFP–LC3–RFP reporter were grown as organoids for 8 days, collected and dissociated into single cells as mentioned above. Cells were sorted on MoFlo XDP (Beckman Coulter) based on the GFP/RFP ratio as described in detail elsewhere (Gump et al., 2014a; 2014b). The purity of cells after sorting was confirmed by post-sort analyses and was usually >90%.

### **Histology and immunohistochemistry**

For formalin-fixed paraffin-embedded (FFPE) sections, tissues were fixed in 10% buffered formalin, and embedded in paraffin. Five-micrometer-thick FFPE sections were used for H&E staining. For immunohistochemical staining, FFPE sections were deparaffinized, rehydrated and incubated in boiling 10 mM pH 6.0 citrate buffer for 20 min for antigen retrieval. To visualize the GFP–LC3–RFP reporter signal or mStrawberry/mSt-ATG4B(C74A) expression in PDAC cells, tissues were fixed in 2% PL solution at 4° C

overnight, incubated in PBS containing 30% sucrose, and embedded in Tissu-Tek OCT compound (Sakura Finetek) on dry ice (Hirata et al., 2018). For immunohistochemical staining, 7- $\mu$ m frozen sections were washed with Tris-buffered saline (pH 7.4) containing 0.05% Tween-20 (TBS-T), blocked with TBS-T containing 5% goat serum for 1 hr at room temperature, and stained with primary antibodies (Supplementary Table 1) at 4° C overnight, followed by incubation with fluorescent-conjugated secondary antibodies (1:400, Supplementary Table 1) at room temperature for 1 h. Sections were counter stained with 4  $\mu$ g ml<sup>-1</sup> Hoechst 33342 (Thermo Fisher) and mounted in ProLong Diamond Antifade Mountant (Thermo Fisher Scientific, P36970). Fluorescent images were obtained with Leica DM6 and analyzed using LAS X software (v.2.0.0.14332.2). Bright light images were obtained with a Leica DM2000 bright-field microscope.

For the measurement of the GFP/RFP signal ratio, frozen sections as prepared above were washed with TBS-T three times and coverslips were mounted with ProLong Diamond Antifade Mountant. Slides were dried at 4° C overnight. Fluorescence images were obtained from at least four random fields per tumor with a 20 $\times$  objective lens. Greyscale, raw-image files (16-bit) were analyzed using ImageJ Software to obtain mean intensities of GFP and RFP signals.

Primary human PDAC specimens (Supplementary Table 3) were generated under Institutional Review Board (IRB)-approved protocol 18-25787 at UCSF. Sections were co-stained with antibodies against CK-19 (1:300) and HLA-A,B (1:300) (Supplementary Table 1). An average of 28 ducts per sample from 9 patient specimens was imaged based on expression of CK-19 to ensure analysis of tumor epithelia. The corresponding MHC-I

localization per CK-19 positive ductal structure was classified as intracellular if greater than 50% of the staining displayed a non-membrane, punctate distribution.

### **Quantitative reverse-transcription PCR**

Total RNA was extracted using TRIzol (Thermo Fisher Scientific) and PureLink RNA Mini Kit (Thermo Fisher Scientific), and then reversed transcribed using Superscript Vilo IV (Thermo Fisher Scientific) with oligo-dT primers. Quantitative PCR was performed with SYBR Green Supermix (Bio-Rad) on the CFX96 real-time PCR machine (Bio-Rad). The quantity of mRNA was calculated using the  $\Delta C_t$  method and normalized by the *GAPDH*, *Actb*, or *36B4* (also known as *Rplp0*) genes for humans or mice, respectively. Sequences for qPCR primers are listed in Supplementary Table 4.

### **Transcriptome analysis**

RNA-seq libraries were prepared using the Illumina TruSeq Stranded mRNA library preparation kit according to manufacturer's instructions by the NYU Genome Technology Center. The libraries were pooled and sequenced as 50-base, single-end reads on an Illumina HiSeq 4000 using high output mode (v4 chemistry). The raw fastq reads were aligned to mm10 mouse reference genome using STAR aligner (Dobin et al., 2013). Fastq Screen was used to check for any contaminations in the samples and Picard RnaSeqMetrics was used to obtain the metrics of all aligned RNA-seq reads. featureCounts was used to quantify the gene expression levels (Lioa et al., 2014). FPKM (fragments per kilobase of transcript per million fragments mapped) data were used as input for gene set enrichment analysis (GSEA) (Subramanian et al., 2005).

## **Immunoblotting**

Cells were lysed in cell lysis buffer (Cell Signaling Technology, 9803) supplemented with protease inhibitor (Thermo Fisher Scientific, A32953) and phosphatase inhibitor (PhosSTOP, Sigma Aldrich, 04906837001). Proteins were separated on 12% or 4–20% Mini-PROTEAN TGX Precast Protein Gels by SDS PAGE electrophoresis and transferred to onto PVDF membranes (IPVH00010, EMD Millipore) or nitrocellulose membranes (GE Healthcare Amersham Protran NC Rolls, Fisher, 10600000). Membranes were blocked in 5% non-fat dry milk (Blotting-Grade Blocker, Bio-Rad, 1706404) dissolved in TBS-T for 1 h and incubated overnight at 4° C with primary antibodies (Supplementary Table 1). Membranes were washed three times with TBS-T and incubated with secondary antibodies for 1 h at room temperature: anti-rabbit IgG, horseradish peroxidase (HRP)-linked (Cell Signaling Technology, 7074), anti-mouse IgG, HRP-linked (Cell Signaling Technology, 7076). Images were obtained by chemiluminescence (Bio-Rad 1705061) using a ChemiDoc (Bio-Rad).

## **Statistical analysis**

Statistical analysis was performed using Graphpad Prism 7.0 (Graph-Pad). Results are expressed as mean  $\pm$  s.d. unless otherwise indicated. For each box-and-whisker plot, center line is the median and whiskers represent the minimum and maximum values.

## **Data availability**

RNA-seq data have been deposited to the Gene Expression Omnibus (GEO) data repository with accession number GSE145766. Source Data are provided for all



experiments. Other data that support the findings of this study are available on request from the corresponding author upon reasonable request.

## References

- Abu-Remaileh, M. et al. Lysosomal metabolomics reveals V-ATPase- and mTOR-dependent regulation of amino acid efflux from lysosomes. *Science* **358**, 807–813 (2017).
- Algarra, I., Cabrera, T. & Garrido, F. The HLA Crossroad in Tumor Immunology. *Hum. Immunol.* **61**, 65–73 (2000).
- Bardeesy, N. et al. Both p16<sup>Ink4a</sup> and the p19<sup>Arf</sup>-p53 pathway constrain progression of pancreatic adenocarcinoma in the mouse. *Proc. Natl Acad. Sci. USA* **103**, 5947–5952 (2006).
- Beatty, Gregory L., Gladney, W. L. Immune escape mechanisms as a guide for cancer immunotherapy. *Clin Cancer Res.* **21**, 687–692 (2015).
- Biancur, D. E. et al. Compensatory metabolic networks in pancreatic cancers upon perturbation of glutamine metabolism. *Nat. Commun.* **8**, 15965 (2017).
- Boj, S. F. et al. Organoid models of human and mouse ductal pancreatic cancer. *Cell* **160**, 324–338 (2015).
- Branon, T. C. et al. Efficient proximity labeling in living cells and organisms with TurboID. *Nat. Biotechnol.* **36**, 880–887 (2018).

- Broz, M. L. et al. Dissecting the tumor myeloid compartment reveals rare activating antigen-presenting cells critical for T cell immunity. *Cancer Cell* **26**, 638–652 (2014).
- Campoli, M. & Ferrone, S. HLA antigen changes in malignant cells: epigenetic mechanisms and biologic significance. *Oncogene* **27**, 5869–5885 (2008).
- Chang, C. & Campoli, M. *Classical and Nonclassical HLA Class I Antigen and NK Cell-Activating Ligand Changes in Malignant Cells: Current Challenges and Future Directions. Advances in Cancer Research* **93**, (Elsevier Masson SAS, 2005).
- Cunha, L. D. et al. LC3-associated phagocytosis in myeloid cells promotes tumor immune tolerance. *Cell* **175**, 429–441 (2018).
- Dangaj, D. et al. Cooperation between constitutive and inducible chemokines enables T cell engraftment and immune attack in solid tumors. *Cancer Cell* **35**, 885–900 (2019).
- DeVorkin, L. et al. Autophagy regulation of metabolism is required for CD8<sup>+</sup> T cell anti-tumor immunity. *Cell Rep* **27**, 502–513 (2019).
- Dobin, A. et al. STAR: ultrafast universal RNA-seq aligner. *Bioinformatics* **29**, 15–21 (2013).
- Fujita, N. et al. An Atg4B mutant hampers the lipidation of LC3 paralogues and causes defects in autophagosome closure. *Mol. Biol. Cell* **19**, 4651–4659 (2008).

- Gump, J. M. et al. Autophagy variation within a cell population determines cell fate through selective degradation of Fap-1. *Nat. Cell Biol.* **16**, 47–54 (2014).
- Gump, J. M. & Thorburn, A. Sorting cells for basal and induced autophagic flux by quantitative ratiometric flow cytometry. *Autophagy* **10**, 1327–1334 (2014).
- Hanahan, D. & Weinberg, R. A. Review Hallmarks of Cancer : The Next Generation. *Cell* **144**, 646–674 (2011).
- Heckmann, B. L. et al. LC3-associated endocytosis facilitates beta-amyloid clearance and mitigates neurodegeneration in murine Alzheimer's disease. *Cell* **178**, 536–551 (2019).
- Hildner, K. et al. Batf3 deficiency reveals a critical role for CD8 $\alpha^+$  dendritic cells in cytotoxic T cell immunity. *Science* **322**, 1097–1100 (2008).
- Hirata, Y. et al. CD150<sup>high</sup> bone marrow Tregs maintain hematopoietic stem cell quiescence and immune privilege via adenosine. *Cell Stem Cell* **22**, 445–453 (2018).
- Kaizuka, T. et al. An autophagic flux probe that releases an internal control. *Mol. Cell* **64**, 835–849 (2016).
- Karasic, T. B. et al. Effect of gemcitabine and nab-paclitaxel with or without hydroxychloroquine on patients with advanced pancreatic cancer: a phase 2 randomized clinical trial. *JAMA Oncol.* **5**, 993–998 (2019).

- Katheder, N. S. et al. Microenvironmental autophagy promotes tumour growth. *Nature* **541**, 417–420 (2017).
- Kirkin, V., McEwan, D. G., Novak, I. & Dikic, I. A role for ubiquitin in selective autophagy. *Mol. Cell* **34**, 259–269 (2009).
- Kirkin, V. et al. A role for NBR1 in autophagosomal degradation of ubiquitinated substrates. *Mol. Cell* **33**, 505–516 (2009).
- Lee, H. K. et al. In vivo requirement for Atg5 in antigen presentation by dendritic cells. *Immunity* **32**, 227–239 (2010).
- Li, J. et al. Tumor cell-intrinsic factors underlie heterogeneity of immune cell infiltration and response to immunotherapy. *Immunity* **49**, 178–193 (2018).
- Liao, Y., Smyth, G. K. & Shi, W. featureCounts: an efficient general purpose program for assigning sequence reads to genomic features. *Bioinformatics* **30**, 923–930 (2014).
- Liu, N., Furukawa, T., Kobari, M. & Tsao, M. S. Comparative phenotypic studies of duct epithelial cell lines derived from normal human pancreas and pancreatic carcinoma. *Am. J. Pathol.* **153**, 263–269 (1998).
- Loi, M. et al. Macroautophagy proteins control MHC class I levels on dendritic cells and shape anti-viral CD8<sup>+</sup> T cell responses. *Cell Rep.* **15**, 1076–1087 (2016).

- Markosyan, N. et al. Tumor cell-intrinsic EPHA2 suppresses anti-tumor immunity by regulating PTGS2 (COX-2). *J. Clin. Invest.* **130**, 3594–3609 (2019).
- Matsuura, T. et al. Organoid-based ex vivo reconstitution of Kras-driven pancreatic ductal carcinogenesis. *Carcinogenesis* bgz122 (2019).
- McAlister, G. C. et al. MultiNotch MS3 enables accurate, sensitive, and multiplexed detection of differential expression across cancer cell line proteomes. *Anal. Chem.* **86**, 7150–7158 (2014).
- McGranahan, N. et al. Allele-specific HLA loss and immune escape in lung cancer evolution. *Cell* **171**, 1259–1271 (2017).
- Michaud, M. et al. Autophagy-dependent anticancer immune responses induced by chemotherapeutic agents in mice. *Science* **334**, 1573–1577 (2011).
- Moral, J. A. et al. ILC2s amplify PD-1 blockade by activating tissue-specific cancer immunity. *Nature* **579**, 130–135 (2020).
- Mosesson, Y. et al. Endocytosis of receptor tyrosine kinases is driven by monoubiquitylation, not polyubiquitylation. *J. Biol. Chem.* **278**, 21323–21326 (2003).
- Munster, T. et al. Hydroxychloroquine concentration-response relationships in patients with rheumatoid arthritis. *Arthritis Rheum.* **46**, 1460–1469 (2002).

- Navarrete-Perea, J., Yu, Q., Gygi, S. P. & Paulo, J. A. Streamlined tandem mass tag (SL-TMT) protocol: an efficient strategy for quantitative (phospho)proteome profiling using tandem mass tag-synchronous precursor selection-MS3. *J. Proteome Res.* **17**, 2226–2236 (2018).
- O'Reilly, E. M. et al. Durvalumab with or without tremelimumab for patients with metastatic pancreatic ductal adenocarcinoma: a phase 2 randomized clinical trial. *JAMA Oncol.* **5**, 1431–1438 (2019).
- Pandha, H., Rigg, A., John, J. & Lemoine, N. Loss of expression of antigen-presenting molecules in human pancreatic cancer and pancreatic cancer cell lines. *Clin. Exp. Immunol.* **148**, 127–135 (2007).
- Paulo, J. A., Gaun, A. & Gygi, S. P. Global analysis of protein expression and phosphorylation levels in nicotine-treated pancreatic stellate cells. *J. Proteome Res.* **14**, 4246–4256 (2015).
- Perera, R. M. et al. Transcriptional control of autophagy-lysosome function drives pancreatic cancer metabolism. *Nature* **524**, 361–365 (2015).
- Poillet-Perez, L. et al. Autophagy maintains tumour growth through circulating arginine. *Nature* **563**, 569–573 (2018).
- Pommier, A. et al. Unresolved endoplasmic reticulum stress engenders immune-resistant, latent pancreatic cancer metastases. *Science* **360**, eaao4908 (2018).

- Rodig, S. J. et al. MHC proteins confer differential sensitivity to CTLA-4 and PD-1 blockade in untreated metastatic melanoma. *Sci. Transl. Med.* **10**, eaar3342 (2018).
- Rooney, M. S., Shukla, S. A., Wu, C. J., Getz, G. & Hacohen, N. Molecular and genetic properties of tumors associated with local immune cytolytic activity. *Cell* **160**, 48–61 (2015).
- Ryschich, E. et al. Control of T-cell-mediated immune response by HLA class I in human pancreatic carcinoma. *Clin. Cancer Res.* **11**, 498–504 (2005).
- Sakuishi, K. et al. Targeting Tim-3 and PD-1 pathways to reverse T cell exhaustion and restore anti-tumor immunity. *J Exp Med* **207**, 2187-2194, doi:10.1084/jem.20100643 (2010).
- Schreiber, R. D., Old, L. J. & Smyth, M. J. Cancer Immunoediting: Integrating Suppression and Promotion. *Science (80-. )*. **331**, 1565–1571 (2011).
- Soares, K. C. et al. A preclinical murine model of hepatic metastases. *J. Vis. Exp.* **51677**, 51677 (2014).
- Sousa, C. M. et al. Pancreatic stellate cells support tumour metabolism through autophagic alanine secretion. *Nature* **536**, 479–483 (2016).



Spranger, S., Dai, D., Horton, B. & Gajewski, T. F. Tumor-residing Batf3 dendritic cells are required for effector T cell trafficking and adoptive T cell therapy. *Cancer Cell* **31**, 711–723 (2017).

Spranger, S. & Gajewski, T. F. Mechanisms of Tumor Cell – Intrinsic Immune Evasion. (2018).

Spranger, S., Sivan, A., Corrales, L. & Gajewski, T. F. *Tumor and Host Factors Controlling Antitumor Immunity and Efficacy of Cancer Immunotherapy*. *Tumor Immunology* **130**, (Elsevier Inc., 2016).

Starobinets, H. et al. Antitumor adaptive immunity remains intact following inhibition of autophagy and antimalarial treatment. *J. Clin. Invest.* **126**, 4417–4429 (2016).

Subramanian, A. et al. Gene set enrichment analysis: a knowledge-based approach for interpreting genome-wide expression profiles. *Proc. Natl Acad. Sci. USA* **102**, 15545–15550 (2005).

Xu, X. et al. Autophagy is essential for effector CD8<sup>+</sup> T cell survival and memory formation. *Nat. Immunol.* **15**, 1152–1161 (2014).

Yang, S. et al. Pancreatic cancers require autophagy for tumor growth. *Genes Dev.* **25**, 717–729 (2011).

Yang, A. et al. Autophagy is critical for pancreatic tumor growth and progression in tumors with p53 alterations. *Cancer Discov.* **4**, 905–913 (2014).

Yang, A. et al. Autophagy sustains pancreatic cancer growth through both cell-autonomous and nonautonomous mechanisms. *Cancer Discov.* **8**, 276–287 (2018).

Waddell, N. et al. Whole genomes redefine the mutational landscape of pancreatic cancer. *Nature* **518**, 495–501 (2015).

Ward, J. P., Gubin, M. M. & Schreiber, R. D. The role of neoantigens in naturally occurring and therapeutically induced immune responses to cancer. *Adv. Immunol.* **130**, 25–74 (2016).

Zeh, H. et al. A randomized phase II preoperative study of autophagy inhibition with high-dose hydroxychloroquine and gemcitabine/nab-paclitaxel in pancreatic cancer patients. *Clin. Cancer Res.* <https://doi.org/10.1158/1078-0432.CCR-19-4042> (2020).

Zoncu, R. et al. mTORC1 senses lysosomal amino acids through an inside-out mechanism that requires the vacuolar H<sup>+</sup>-ATPase. *Science* **334**, 678–683 (2011).

## **Chapter 3: Identifying Novel Regulators of MHC-I in Pancreatic Cancer**

## **Abstract**

Major histocompatibility complex I (MHC-I) is a critical molecule for anti-tumor immunity that is frequently dysregulated in cancer. Endogenous antigen presentation by MHC-I on tumor cells is necessary for recognition by CD8<sup>+</sup> T cells and subsequent clearance. Defects in MHC-I expression leads to impaired antigen presentation, immune evasion and/or resistance to immune checkpoint blockade (ICB) therapy. Pancreatic ductal adenocarcinoma (PDAC), a deadly malignancy with dismal patient prognosis, shows frequent downregulation of MHC-I, abrogating MHC-I expression independent of genetic mutations. Identification of cell autonomous pathways specific to PDAC are necessary to elucidate the underlying biology preventing MHC-I from reaching the plasma membrane to present antigens and elicit an immune response. In this study, we combined a whole-genome CRISPRi screen and Turbo-ID proximity-dependent proteomics to determine regulators and interactors of MHC-I, respectively. 101 overlapping candidates were identified from the two datasets, many of which were related to known pathways of MHC-I expression and others that present novel ways to regulate MHC-I. Interestingly, several hits related to trafficking machinery and post-translational modification were identified, such as ubiquitylation by HERC4, an E3 ligase, that has previously not been reported to regulate MHC-I in cancer. HERC4 overexpression in PDAC was observed across multiple cell lines and knockdown of this gene led to increased expression, validating the screen candidate. Utilizing these two datasets as a resource of MHC-I regulation can identify PDAC-specific mechanisms that facilitate altered trafficking of MHC-I and consequently, modulation of an anti-tumor response. Deeper investigation into the screen hits may

provide novel candidates for which new therapeutic strategies could be developed for combating this deadly disease.

## **Background**

PDAC, a malignancy refractory to most therapies including immune checkpoint blockade (ICB) therapy, utilizes diverse mechanisms to evade immune clearance. One mechanism involves reduced presentation of tumor specific antigens by MHC-I to immune cells. Many cancers alter MHC-I expression via genetic or epigenetic silencing, however changes in MHC-I trafficking can also profoundly influence antigen presentation at the cell surface and is a previously underappreciated mechanism of MHC-I regulation in cancer. Selective targeting of MHC-I molecules for degradation via the autophagy and lysosome pathway has recently been described (Yamamoto, Venida. et al., 2020). High proportions of MHC-I are trapped intracellularly with autophagosomes and lysosomes. Notably, autophagy or lysosome inhibition restores surface MHC-I levels, leading to improved antigen presentation, enhanced anti-tumor T cell response, and reduced tumor growth in syngeneic hosts (Yamamoto, Venida. et al., 2020). These findings add to a growing list of works that support tumor cell intrinsic properties in regulating antigen presentation and promoting immune evasion (DeVorkin et al., 2019; Chen et al., 2018; Yang et al., 2018; Pommier et al., 2018; Frazier et al., 2017; Wei et al., 2016; Karsli-Uzunbas et al., 2014; Baginska et al., 2013; Noman et al., 2014; Pandha et al., 2007).

Post-translational modifications (PTM) have been shown to regulate protein functions involved in cell cycle, survival, and proliferation in cancer cells (Zheng et al., 2019; Sharma, et al., 2019). These critical molecular events alter protein conformation by regulating their localization, stability, interactions with other proteins, hydrophobicity, and

ultimately, their function (Zamaraev et al., 2017). Consequently, these modifications will affect cellular signaling events that serve as regulatory mechanisms involved in tumorigenesis, immune responses, cell cycle progression, DNA repair, and apoptosis (Han et al., 2018). PTM modifications of MHC-I have led to loss of antigen presentation in cancer by various mechanisms, including sterically hindering MHC-I interaction with T cells (Jongsma et al., 2020), altering the peptide-binding groove (Cruz et al., 2017), and causing mislocalization of MHC-I for degradation via endoplasmic-reticulum-associated degradation (Wang et al., 2020).

Technological advances in genetic screening tools, such as CRISPR-Cas9 genome editing, have allowed researchers to uncover novel protein regulators and molecular players in a range of biological processes. The expansion of this toolkit has allowed for the elucidation of gene function in diseased states and permits mechanistic discovery that lead to promising drug targets and therapeutics. With the development of CRISPR interference (CRISPRi), groups have been able to probe genome function in a wide range of diseases, such as cancer and neurodegeneration. CRISPRi fuses a KRAB effector domain, that functions as a transcriptional repressor, with a deactivated Cas9 nuclease (dCas9) to achieve repression of a targeted gene (Gilbert et. al., 2013; Horlbeck et. al., 2016). Pooled genetic screens targeting the entire human genome have been developed to interrogate mechanistic biology.

Here, we used the CRISPRi system to perform a comprehensive genome-wide screen in human PDAC cells to identify novel regulators of MHC-I surface expression. In parallel, we combined a proximity-labeling proteomic approach to identify interactors of MHC-I. By overlaying the two datasets, we were able to narrow the candidates that modulate MHC-

I expression down to 101 and identified several novel regulators in PDAC. Interestingly, enrichment analysis revealed several signaling pathways, protein PTMs, and trafficking machinery as significant pathways controlling surface MHC-I expression. Our data provide a resource for understanding regulation of MHC-I expression and provides new clues how these antigen presenting molecules are diverted from the plasma membrane.

## **Results**

### **Whole genome CRISPRi screen identifies novel regulators of MHC-I in PDAC**

PaTu8902 human PDAC cells were engineered to stably express dCas9 (dCas8902) for a genome-wide CRISPRi-mediated suppression screen. dCas8902 cells were validated to test if the stable line could repress transcription robustly using knockdown of a targeted gene. A lentiviral sgRNA library comprised of five sgRNAs per gene that target ~20,500 human genes and ~10,000 negative control sgRNAs were transduced in dCas8902. Cells were stained with a fluorescently conjugated HLA-A, B, C antibody after lentiviral infection and sorted into the bottom 30% (MHC-I low) and top 30% (MHC-I high) of successfully selected and stained cells (Extended Figure 3.1A-C). Deep sequencing of each sgRNA in a pooled population of knockout cells from the MHC-I low and MHC-I high populations were analyzed to identify novel regulators of MHC-I in PDAC. Cells were divided into two groups: i) negative regulators of genes that suppress antigen presentation via MHC-I (blue); ii) positive regulators of genes required for antigen presentation via MHC-I (orange) (Figure 3.1A).

Gene candidates from the top 25 negative regulators revealed metabolic and transcriptional pathways leading to an MHC-I high phenotype (Figure 3.1B-C). Differentially expressed genes analyzed through Enrichr and DAVID (Kuleshov et al.,

2016; Chen et al., 2013; Huang et al., 2009), web-based tools that provide bioinformatic enrichment analysis organized into gene-set libraries and pathway visualizations, revealed pyrimidine and purine metabolism as regulators of MHC-I. Interestingly, several groups have published that targeting nucleotide metabolism and disrupting the balance of purines and pyrimidines can regulate immune suppression and antigen presentation (Keshet et al., 2020; Mastelic-Gavillet et al., 2019). As expected, pathways related to RNA regulation (spliceosome and RNA degradation) and antigen processing and presentation were among the top enriched terms from the 25 most significant hits from the MHC-I positive regulators (Figures 3.1B, D).

Knockdown of autophagic machinery genes have been shown to increase cell surface expression of MHC-I in PDAC (Yamamoto, Venida et al. Nature 2020). As expected, knockdown of genes related to autophagy led to an MHC-I high phenotype and serve as negative regulators of MHC-I in pancreatic cancer (Figure 3.1E). Analysis from Figure 1E-F takes all gene candidates identified from the CRISPRi screen. Additionally, silencing of antigen presentation genes via CRISPRi led to an MHC-I low phenotype, confirming that this screen is targeting specific genetic modifiers of plasma membrane MHC-I expression rather than non-specific genes. Among the hits from this knockout screen were genes encoding E3 ubiquitin ligases, and signaling pathways related to immune responses, metabolism, DNA damage, and metastasis (Figure 3.1F). Of the ubiquitin ligases and ubiquitin-like modifiers in the CRISPRi screen that were statistically significant as putative MHC-I negative regulators, seven have been implicated in innate immunity, antigen processing and presentation and MHC-I regulation: three members of the MARCH ubiquitin ligases MARCH2, MARCH8, and MARCH9 (Nathan and Lehner, 2008; Eyster



et al., 2011); WWP2 (Alix et al., 2020); PELI2 (Humphries et al., 2018; Hu and Sun 2016); and two members of the small ubiquitin-like modifier (SUMO) pathway SUMO2, UBA2/SAE2 (Loureiro et al., 2006; Lamsoul et al., 2005).

It has been shown that lysosomal targeting of cell surface transmembrane proteins requires their post-translational modification by E3 ubiquitin ligases which conjugate ubiquitin molecules to their cytoplasmic tails, leading to their removal from the cell surface and subsequent degradation in the lysosome (Komander & Rape, 2012). Overexpression of ubiquitin ligases have been observed in patients with pancreatic cancer and contribute to carcinogenesis (Zhang et al., 2008), PDAC cancer growth (Deng et al., 2021), and metastasis (Li et al., 2021). This finding suggests that upregulation of E3 ubiquitin ligases is a potential PDA-specific event which may cooperate with the autophagy/lysosome system to regulate expression of MHC-I on the plasma membrane.

### **Discovery of novel regulators of MHC-I in PDAC using proximity dependent biotinylation proteomics and CRISPRi screening**

Proximity labeling was employed to map out the MHC-I interactome in PDAC. To identify interactors of MHC-I, the C terminus of HLA-A was fused to a Flag tag and TurboID (Branon et al., 2018), an engineered biotin ligase that converts ATP into a reactive intermediate that covalently labels proximal proteins within a 10nm radius (Figure 3.2A). KP4 human PDAC cells were engineered to express the HLA-A-TurboID-Flag (8902 HLA-A-TrID) construct and quantitative mass spectrometry was performed to identify positive proximity interactors. Proteomic analysis revealed 2888 biotinylated proteins as significantly enriched from streptavidin conjugated beads. By overlaying the 633 MHC-I high hits from the CRISPRi screen as regulators with the 2388 candidates identified from

the proximity biotinylation proteomics as interactors, we found 101 overlapping hits (Figure 3.2B). Hierarchical clustering on enriched terms using Metascape revealed enrichment of pathways related to cell cycle, RNA metabolism, translation, cellular transport, and autophagy (Figure 3.2C). In order to infer more biologically interpretable results, Metascape applies an algorithm called MCODE (Bader and Hogue, 2003) to automatically extract protein complexes embedded in the large network as seen in the figure as a network plot. Of particular note were genes related to kinases, trafficking machinery, and E3 ubiquitin ligases – all of which have been generally implicated in MHC-I regulation (Paulsson et al., 2002; Brutkiewicz, 2016; Bartee et al., 2004).

Of the 101 overlapping hits, several known regulators of MHC-I were identified, including trafficking machinery control and kinase regulation of MHC-I surface expression (Figure 3.2D). Given that trafficking of MHC-I molecules within a cell is a dynamically regulated process (Machy et al., 1987; Basha et al., 2008; Wang et al., 2008), it is possible that key regulators of membrane trafficking are preventing plasma membrane expression of MHC-I. Both COPI coat complex subunits (COPA, COPB1, COPB2, COPG2) and Rab GTPases (RAB1A, RABGAP1L) have been identified from the two datasets as regulators of MHC-I. Importantly, both family of proteins have been implicated in MHC-I trafficking. COPI has been shown to mediate retrograde transport of MHC-I molecules from the Golgi apparatus to the endoplasmic reticulum (Paulsson et al., 2002) and Rab GTPases have been identified as MHC-I regulators in trafficking vesicles (Zou et al., 2009; Zerial and McBride, 2001). The complex route of MHC-I trafficking implies that it can be captured at several locations – ER, plasma membrane, endosome – and re-routed to the lysosome for degradation.

Additionally, the MAPK pathway has been established as a negative regulator of MHC-I expression by various groups. In melanoma, esophageal, and gastric cancers, ERK inhibition results in an increase of MHC-I molecules (Brutkiewicz et al., 2016). Additionally, MAPK signaling has been shown in vivo to suppress components of MHC-I and the antigen presentation machinery (Brea et al., 2016). Using two inhibitors that target different parts of the MAPK signaling pathway, we show that inhibition of MEK1/2 and ERK1/2 lead to increased total and plasma membrane protein levels of MHC-I in PDAC after 24 hours of treatment (Figure 3.3 A-C). The ~35 amino acid cytoplasmic-tail of MHC-I contains two conserved phosphorylation sites, Tyrosine-320 and Serine-335, which have been previously linked to MHC-I trafficking in immune cells (Guild and Strominger, 1984; Santos et al., 2004; Lizee et al., 2005). Upon MAPK pathway inhibition induces rapid upregulation of surface MHC-I expression in BRAF mutant melanoma cell lines. A point mutation on the serine-335 phosphorylation site (S335A) of the MHC-I tail abolishes cell surface increase of MHC-I as seen in WT cells (Bradley et al., 2015). Because several kinases involved in the MAPK signaling pathway have been identified in our CRISPRi and proteomic datasets (ARAF, BRAF, MAPK), it's possible that direct phosphorylation by any of these related kinases may regulate MHC-I expression. Generating MHC-I variants with mutations at the two conserved phosphorylation sites, tyrosine-320 and serine-335, or suppressing individual kinases will be critical to address the possibility of kinase regulation of MHC-I protein stability and localization.

### **E3 ubiquitin ligase HERC4 mediates MHC-I plasma membrane expression**

Identification of E3 ubiquitin ligases from the overlapping datasets warrants special attention since we previously showed that MHC-I is post-translationally modified with

ubiquitin, tagging it for capture and degradation via the autophagy-lysosome pathway (Yamamoto and Venida et al., 2020). However, the precise mechanism underlying how and why MHC-I is ubiquitylated in PDAC remains unclear. Ubiquitylation of proteins is mediated by E3 ubiquitin ligases, which directly conjugates ubiquitin molecules to a target substrate. Trafficking of several proteins to the lysosome is facilitated by E3 ligase dependent ubiquitylation (Eyster et al., 2011; Bartee et al., 2004). Over 600 putative E3 ubiquitin ligases have been identified and have key roles in endocytosis, signal transduction, DNA repair, and immune signaling (Komander and Rape, 2012).

Four overlapping E3 ubiquitin ligases were identified from the CRISPRi and Biotinylation datasets (HERC4, WWP2, TRAF2, ZNF598). Using an online analysis tool that queries genes based on a similarity metric to find putative functional paralogs and Gene Ontology pathways (GeneAnalytics, Gene Set Analysis), HERC4 ubiquitin ligase has been putatively linked to immunity, antigen processing and presentation, and regulation of MHC-I or MHC-II. In several tumor types, HERC4 has been shown to regulate protein stability of tumor suppressors via ubiquitylation and control tumorigenic activities (Sala-Gaston et al., 2020). In breast cancer and hepatocellular carcinoma, pro-tumorigenic roles have been described. Knockdown of HERC4 in human breast cancer cells dramatically suppresses their proliferative and migratory capacity, leading to decreased tumor growth (Zhou et al., 2013; Xu et al., 2019). In hepatocellular carcinoma, HERC4 is overexpressed and contributes to the proliferation and migration of these tumor cells (Zheng et al., 2017). We investigated whether HERC4 regulates MHC-I protein stability and surface expression in PDAC.

PDAC cells expressed varying levels of HERC4 at the protein and transcript level compared to the non-transformed human pancreatic ductal epithelial (HPDE) control cell line (Figure 3.4 A). Similar to what was observed from whole cell lysates, KP4, PaTu8902, and Panc1 cells had the highest transcript expression levels relative to HPDE cells (Figure 3.4 B). To validate that HERC4 is a negative regulator of MHC-I from the CRISPRi screen, sgRNAs were designed to silence transcription in dCas8902 cells (Figure 3.4 C). Knockdown of HERC4 using two different guides increased plasma membrane levels of MHC-I (Figure 3.4 D). Additionally, less polyubiquitylation of MHC-I was observed upon HERC4 knockdown (Figure 3.4 E-F). Though not completely absent, ubiquitylation of MHC-I could be controlled by other ubiquitin ligases identified in the CRISPRi screen and TurboID proteomics. Single or simultaneous knockdown of these other E3 ligases or the use of a small-molecule inhibitor against the ubiquitin-activating enzyme (E1) will be important to address the role of ubiquitylation on MHC-I localization.

## **Discussion**

Our results from the whole-genome CRISPRi screen and proximity-labeling proteomics identifies both known and novel MHC-I regulators, many of which were related to signaling pathways, post-translational modifications, and trafficking machinery. A likely hypothesis based on the enrichment analysis between the two datasets is the diversion of MHC-I plasma membrane expression via trafficking machinery and regulation of protein stability through post-translational modifications. It's possible that kinases related to MAPK or mTOR signaling may either directly control MHC-I localization or indirectly through regulation of phosphoproteins involved in MHC-I degradation.

The cytoplasmic tail of MHC-I proteins is highly conserved across HLA-A, B, and C allotypes (Burr et al., 2013). I have identified a maximum of three Lysine residues in the C-terminal tail of HLA-A, which could be ubiquitylated. By employing site-directed mutagenesis, Flag-tagged single and combination Lysine to Arginine mutants of HLA-A expressed in PDAC cells will be critical to determine the extent of ubiquitin regulation of MHC-I protein stability. Alternative ubiquitin conjugation mechanisms are also a possibility. For example, ubiquitin can be conjugated to non-lysine residues such as cysteine via a thioester bond and serine or threonine residues via an ester bond (Komander and Rape, 2013). Systematically mutating conserved cysteine, serine, and threonine residues within the C-terminal tail of MHC-I will address the possibility of ubiquitin conjugation to MHC-I.

As ubiquitylation of proteins via E3 ligases has been described as a primary mechanism to regulate protein stability, it comes as no surprise that several appeared from the screen and proteomic dataset. Overexpression of ubiquitin ligases has been described in cancer, however a broader function for E3 ligase regulation of MHC-I in cancer and PDAC has not been fully explored. Evidence from this study suggests conjugation of ubiquitin molecules to MHC-I for targeted degradation via E3 ligase as a probable possibility. In addition to HERC4 regulation of MHC-I described above, the MARCH family of ligases have been implicated as critical regulators of immune responses by targeting viral proteins and immunoreceptors for polyubiquitylation and degradation in professional antigen-presenting cells (Nathan and Lehner, 2008; Visser Smith et al., 2009). For example, MARCH proteins were previously shown to ubiquitylate MHC-II in dendritic cells (Shin et al., 2006). In the context of cancer, one study showed that MARCH8

overexpression has been linked to growth of esophageal tumors (Singh et al., 2017). My preliminary data suggest that several members of the MARCH ligases are upregulated in a number of PDAC cell lines (FIGURE 4A). Importantly, my preliminary data demonstrate that knockdown of MARCH8 in KP4 and MiaPaca PDA cell lines restored MHC-I surface expression with no effect in HPDE cells. This result suggests that E3 ligase upregulation is a potential PDA-specific event which functions to regulate expression of MHC-I on the plasma membrane.

In line with PTM regulation of MHC-I, several genes related to SUMOylation were significantly enriched from the MHC-I high phenotype in the CRISPRi screen (SAE1, UBA2, SUMO2, SENP7, SENP5). SUMOylation results in the addition of the small protein SUMO to its targeted substrate, regulating protein structure, intracellular localization, and protein-protein interactions (Hendriks and Vertegaal, 2016). In an aggressive PDAC subtype characterized with MYC amplification and several components of the SUMO pathway, it was shown that MYC hyperactivity in PDAC was connected to an increased sensitivity to SUMO inhibition (Biederstadt et al., 2020). In data not shown, UBA2, the SUMO E1 activating enzyme, was shown to be overexpressed in several PDAC cell lines compared to HPDE. Both genetic inhibition of UBA2 and general inhibition of SUMOylation using a small molecule inhibitor resulted in an increase of MHC-I at the plasma membrane. Similar to ubiquitylation, proteins are SUMOylated at lysine residues. The crosstalk between ubiquitylation and SUMOylation may play a critical role in MHC-I regulation by redirecting MHC-I molecules from the plasma membrane to degradative organelles like the lysosome or proteasome. Both post-translational modifications play critical roles in protein trafficking, stability, signaling, and transcriptional regulation. These

processes ultimately control a number of biological processes important in cancer, such as cell migration and survival (Wei and Lin, 2012). Though SUMOylation historically has not been described as an important PTM for degradation, accumulating evidence suggests SUMOylation primes proteins for ubiquitination and subsequent degradation (Kumar et al., 2017). Studying the interplay between both SUMOylation and ubiquitination will be important to determine MHC-I protein fate as deregulation in these two processes may lead to aberrant activity and immune evasion.

Similar to proteins involved in post-translational modification in PDAC, another likely hypothesis is kinase regulation of MHC-I protein stability. Proteins related to signaling pathways such as MAPK and several components of the mTOR complex (mTOR, LAMTOR1, LAMTOR2, LAMTOR3, RPTOR, RagA) were significantly enriched as genes suppressing antigen presentation via MHC-I. While direct regulation of MAPK signaling on the Serine-335 residue on the MHC-I cytoplasmic tail has been described above (Bradley et al., 2015), kinase regulation of phosphoproteins indirectly involved in MHC-I degradation is another possibility. One hypothesis involves regulation of ubiquitin ligase activity by direct phosphorylation. Phosphorylation has been shown to cause allosteric activation on E3 ligases (Gallagher et al., 2006) and can regulate E2 activity (Wood et al., 2005). The second hypothesis focuses on phosphodegrons, a recognition signal for substrate binding of an E3 ligase induced upon phosphorylation (Rogers et al., 1986). Phosphodegron motifs can provide an additional means of control in proteins that are ubiquitylated in a phosphorylation-dependent manner. The final hypothesis is related to phosphorylation-dependent control of substrate localization mediated by interaction with an E3 ligase. Several groups have shown that phosphorylation can regulate subcellular



re-localization of substrates, allowing it to interact with its target E3 ligase for ubiquitylation (Besson et al., 2006; Nakayama and Nakayama, 2006). Phosphorylation of the MHC-I tail by either MAPK or mTOR could re-localize MHC-I to an alternate subcellular compartment, allowing ubiquitylation by an E3 ligase and subsequent degradation. Kinase regulation of MHC-I via phosphorylation-dependent ubiquitination, phosphodegron, or subcellular re-localization in PDAC may play a significant role in protein turnover. Additionally, results from the two datasets can reveal how ubiquitination is regulated – a process that has been historically understudied and poorly understood. This study serves as a resource to identify the underlying biology preventing MHC-I from reaching the plasma membrane and eliciting an anti-tumor response in PDAC cells. While autophagy and lysosome suppression are capable of increasing surface MHC-I, it only remedies the problem and does not tell us why MHC-I is unable to traffic normally. The ability to use unbiased screening and proteomic technologies to understand protein function, probe gene regulation, and study protein-protein interaction has revolutionized our ability to uncover mechanisms and therapeutic strategies for human diseases. Results from these findings help to determine the causes of aberrant intracellular localization of MHC-I in one of the world's most lethal diseases – pancreatic cancer. The ultimate goal is to identify new nodes that can be targeted to more efficiently restore plasma membrane MHC-I. These studies also lay the foundation for understanding mechanisms of immune evasion in other aggressive cancers and highlights the importance of studying tumor-cell intrinsic properties that contribute to a pro-tumorigenic landscape.

# Figures

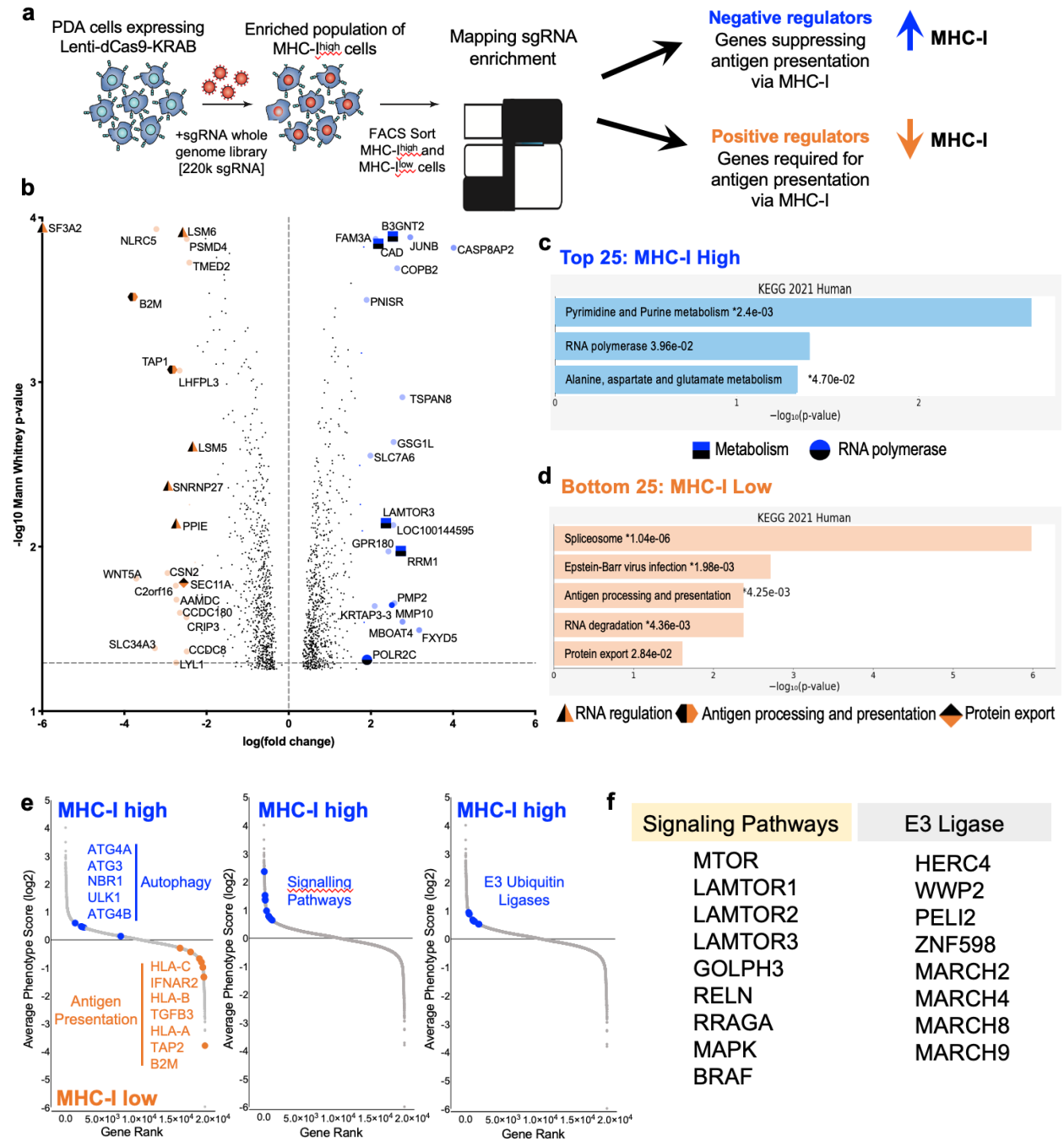


**Figure 3.1. Whole genome CRISPRi screen to identify novel regulators of MHC-I in PDAC.** **A**, Schematic of genome-wide CRISPRi screen in PaTu8902 PDAC cells fluorescently labeled with an MHC-I antibody. Cells were sorted into two groups: top 30% indicated as MHC-I high or negative regulators (blue) and bottom 30% indicated as MHC-I low or positive regulators (orange). **B-D**, Gene candidates from the top 25 negative regulators and bottom 25 positive regulators from the CRISPRi screen. **B**, Volcano plot highlighting the top and bottom 25 significant hits from the MHC-I high and MHC-I low gene candidates, respectively, using the KEGG 2021 PATHWAY Database (human). **C-D**, Enrichment analysis using Enrichr and DAVID (Kuleshov et al., 2016; Chen et al., 2013; Huang et al., 2009) to analyze the 25 gene candidates from the 25 most significant hits in the MHC-I high (**C**) and MHC-I low (**D**) groups. Genes in the volcano plot corresponding to enriched terms related to MHC-I high (metabolism and RNA polymerase) and MHC-I low (RNA regulation, antigen processing and presentation, and protein export) are indicated below the tables. **E**, Enriched pathways taken from all gene candidates identified in the CRISPRi screen. **F**, Candidates from signaling pathways and E3 ubiquitin ligase genes that suppress antigen presentation via MHC-I.

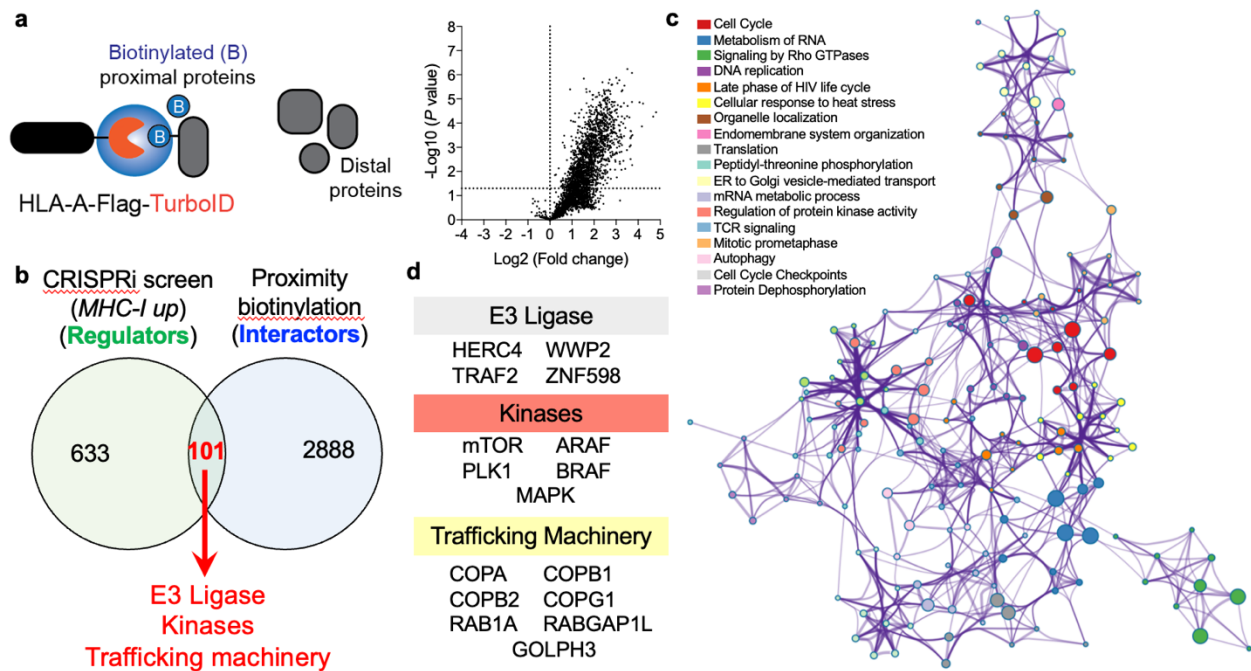


**Figure 3.2. Proximity dependent biotinylation proteomics combined with CRISPRi screening to identify novel regulators of MHC-I in PDAC.** **A**, Proximity-dependent biotinylation catalyzed by HLA-A–TrID. After addition of biotin, TurboID catalyzes the formation of biotin-5'-AMP anhydride, which enables covalent tagging of endogenous proteins with biotin within a few nanometers of the ligase. Biotinylated proteins were enriched with streptavidin conjugated beads and sent off for mass spectrometry. **B**, Venn diagram of statistically significant candidate hits identified from the CRISPRi screen (green) and proximity biotinylation proteomics (blue). 101 candidates were shared between the two datasets. **C**, Visualization of functional enrichment analysis results using Metascape identified 101 gene candidates from the overlaid hits identified in the CRISPRi screen and HLA-A-TrID proteomics. Network of enriched terms are colored by cluster ID, where nodes that share the same cluster ID are typically close to each other. **D**, Candidates from the E3 ligase family, kinase pathways, and trafficking machinery genes that function as negative regulators of MHC-I.

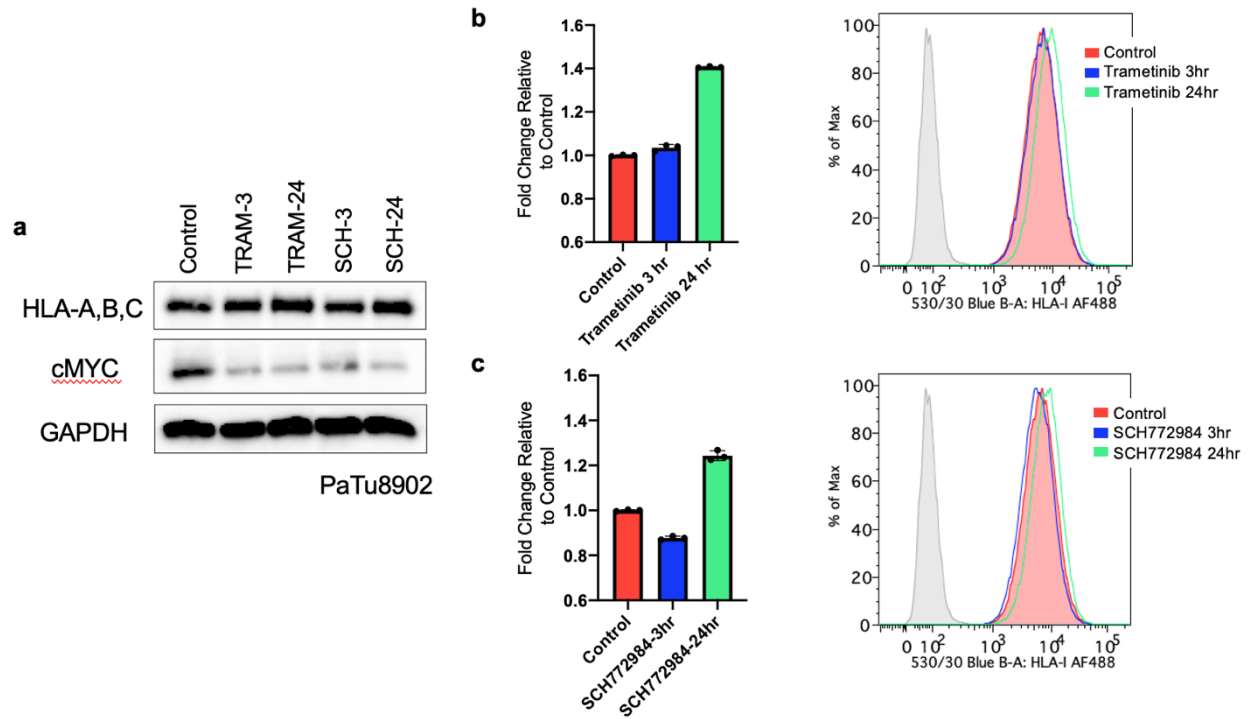


**Figure 3.3. Inhibition of the MAPK signaling pathway restores surface expression of MHC-I 24 hours post-treatment. A**, Total levels of HLA-A, B, C 3- and 24-hours post-treatment with MAPK inhibitors. Trametinib is a kinase inhibitor against MEK1 and MEK2 and SCH772984 is a kinase inhibitor against ERK1 and ERK2. **B-C**, Flow cytometry-based analysis shows treatment with an upstream (**B**) and downstream (**C**) MAPK inhibitor restores MHC-I surface expression at 24 hours.

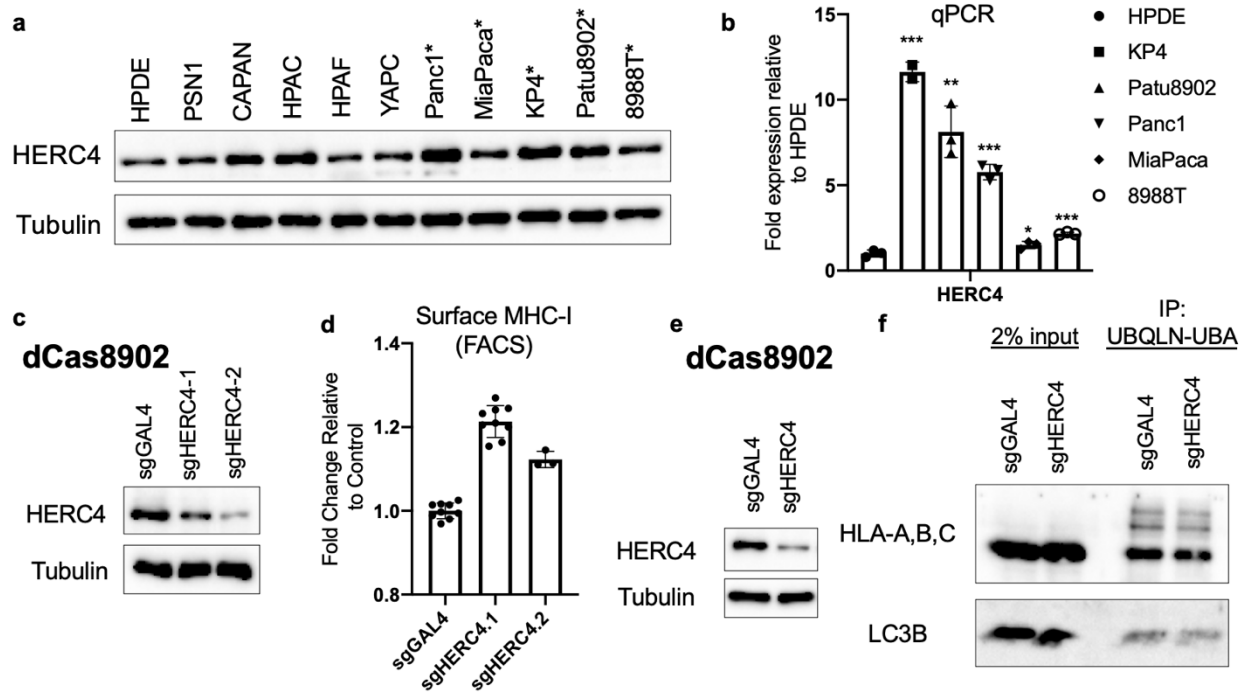
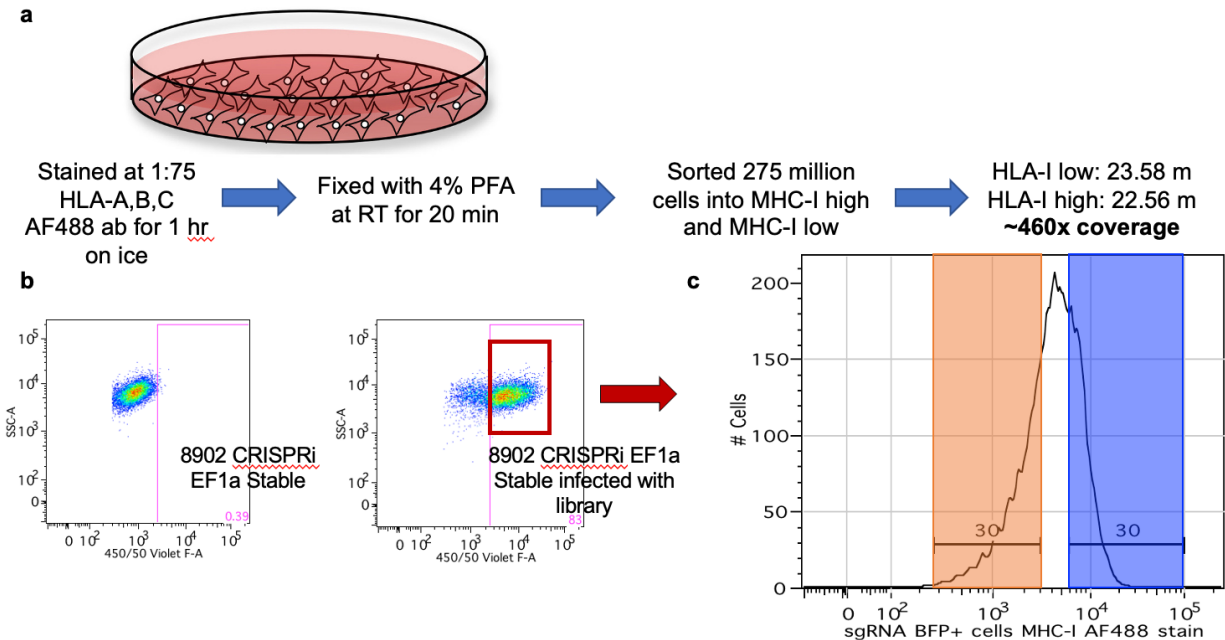


**Figure 3.4. E3 ubiquitin ligase HERC4 is overexpressed in PDAC and mediates plasma membrane expression of MHC-I.** **A**, Protein level of HLA-A, B, C in HPDE and human PDAC cell lines from whole cell lysates. **B**, Transcript levels in HPDE and human PDAC cell lines. **C**, Knockdown levels of HERC4 following CRISPRi mediated knockdown in dCas8902 cell line using two different sgRNAs. **D**, Flow cytometry-based analysis measuring MHC-I levels at the plasma membrane. **E-F**, Knockdown levels following knockdown (**E**). Endogenous ubiquitylated proteins were affinity captured from dCas8902 cells with UBQLN1-UBA-conjugated bead (**F**) and knockdown confirmed in (**E**).



**Extended Figure 3.1e. Cell sorting procedure and layout for whole genome CRISPRi screen in dCas8902 PDAC cells. A**, Schematic of protocol. Cells were stained with an AF488 HLA-A, B, C for one hour, washed, and fixed with 4% PFA. Cells were then sorted on BD LSRFortessa Cell Analyzers. **B**, Control dCas8902 cells vs dCas8902 cells infected with whole genome CRISPRi library five days after puromycin selection (red box). **C**, Histogram showing sorted cell populations based on HLA-A, B, C surface staining. HLA-I low corresponds to the bottom 30% and HLA-I high corresponds to the top 30%.

## **Materials and Methods**

### **Cell culture**

The cell lines PaTu-8988T, KP4, MiaPaca2, PaTu-8902, Panc1, PSN1, CAPAN-I, HPAC, HPAF-II, and YAPC were obtained from the American Type Culture Collection (ATCC) or the DSMZ. HPDE was provided by M. Tsao (Liu et al., 1998). Cells were cultured in the following media: PaTu-8988T, KP4, MiaPaca2, PaTu-8902, Panc1, CAPAN-I, HPAC, and HPAF-II in DMEM supplemented with 10% FBS; Panc 2.03 and HupT3 in RPMI with 10% FBS; PSN-1 and YAPC cells were cultured in RPMI 1640 supplemented with 10% FBS; HPDE cells were cultured in keratinocyte serum-free (KSF) medium supplemented by epidermal growth factor and bovine pituitary extract (Life Technologies, Inc.), supplemented with 1% penicillin and streptomycin (Gibco). Cell lines were regularly tested and verified to be mycoplasma negative using Myco-Alert Detection Kit (Lonza) or via PCR. Cells were grown in a humidified incubator with 5% CO<sub>2</sub> at 37° C.

### **CRISPR vectors**

Lentiviral vectors were utilized to express the sgRNAs and CRISPRi protein in human PDAC cells as described previously (Gilbert et al., 2014). The CRISPRi protein (dCas9-BFP-KRAB) was expressed from the EF-1 $\alpha$  promoter. The sgRNA vector encodes a fluorescent protein (BFP) T2A puromycin N-acetyl transferase gene as well as an sgRNA driven by the mouse U6 promoter driven by the EF-1 $\alpha$  promoter. To generate the lentivirus, HEK293T cells were used. Packaging vectors used were pCMV-dR8.91 and pMD2-G. LT1 transfection reagent (Mirus MIR2300) was used for transfection.



## **Construction of stable cell lines for CRISPRi**

Polyclonal cells expressing dCas9-BFP-KRAB fusion proteins driven from the EF-1 $\alpha$  promoter were generated by viral transduction followed by three rounds of fluorescence-activated cell sorting. PDAC cancer CRISPRi lines are denoted as dCas8902.

## **Whole genome CRISPRi screen**

To perform this CRISPRi screen, the human CRISPRi V2 Top5 sgRNA library was gifted from Luke Gilbert's lab at UCSF (Horlbeck et al., 2016). This whole genome sgRNA library targets 18,905 human genes with five sgRNAs per transcription start site. Cells were grown at a minimum library coverage of 500x for genome-scale screens. Libraries of sgRNA expression constructs are lentivirally transduced into mammalian genomes, using conditions where each cell integrates only one sgRNA construct. Cells were collected five days after puromycin selection and harvested cells were processed for next-generation sequencing. Genomic DNA was isolated from frozen cell pellets. PCR of sgRNA-containing fragments was performed to amplify and append Illumina sequencing adapters. During the amplification, Illumina 5' and Illumina 3' adapters were added to the 3' and 5' end of the sgRNA cassette. To purify the product, PCR clean-up was performed and relative sgRNA abundance was determined by next-generation sequencing as previously described (Gilbert et al., 2014; Horlbeck et al., 2016). Data were analyzed using publicly available code (<https://github.com/mhorlbeck/ScreenProcessing>).

### **Poly-ubiquilin UBA affinity capture**

Cells were washed twice with ice-cold PBS and lysed in lysis buffer (50 mM Tris-HCl pH 7.5, 150 mM NaCl, 1% NP-40, 10 mM *N*-ethylmaleimide) supplemented fresh with protease inhibitor cocktail. Lysates were incubated at 4° C for 15 min and clarified by centrifugation at 20,000 x g at 4° C for 15 min. Samples were quantified by BCA Protein Assay Kit and diluted to 1 mg ml<sup>-1</sup> with dilution buffer (50 mM Tris-HCl, pH 7.5, 150 mM NaCl, 5 mM EDTA, protease inhibitor). Approximately 1–1.5 mg of protein lysates were incubated with 50 µl of Ubiquilin 1 Tandem UBA Agarose (BostonBiochem AM-130) overnight at 4° C. Samples were then washed three times in High Salt Wash Buffer (50 mM Tris-HCl pH 7.5, 250 mM NaCl, 0.5% NP-40) and once with 10 mM Tris-HCl, pH 7.5. Samples were eluted by adding Laemmli buffer and incubating at 65° C for 15–20 min.

For DUB digestions, affinity captured material was washed once with DUB digestion buffer (50 mM Tris-HCl, pH 7.5, 150 mM NaCl, 20 mM dithiothreitol). Liquid was removed and beads were resuspended in 20 ml of DUB digestion buffer and 5 mg of USP2 catalytic domain (Usp2cc; BostonBiochem E-506) for 1 h with gentle shaking at 30° C. Beads were washed once in high-salt wash buffer and once with 10 mM Tris-HCl, pH 7.5, before eluting affinity captured material by adding Laemmli buffer and incubating at 65° C for 15 min.

### **Proximity biotinylation**

Human PDAC cells stably expressing HLA-A–TrID were cultured in DMEM supplemented with 10% dialyzed FBS (DMEM + dFBS) for 48 h. Cells were incubated with 10 µM biotin

(Sigma) and incubated at 37° C for 30 min. Media was replaced with DMEM + dFBS and incubated at 37° C for a further 2–3 hours. For negative controls, we omitted exogenous biotin. Cells were then washed twice in ice-cold PBS and lysed in ice-cold lysis buffer (1% Triton X-100, 130 mM NaCl, 2.5 mM MgCl<sub>2</sub>, 2 mM EGTA, 25 mM HEPES pH 7.4, supplemented fresh with protease inhibitor cocktail) for 30 min on ice. Samples were clarified by centrifugation at 13,300 rpm for 10 min at 4° C. Protein content was measured using BCA Protein Assay Kit (Life Technologies 23227). Then, 1–2 mg of protein lysates were incubated with 50 µl of Dynabeads MyOne Streptavidin C1 (Life Technologies) overnight. The beads were washed twice in wash buffer 1 (2% SDS in dH<sub>2</sub>O), once in wash buffer 2 (0.1% deoxycholate, 1% Triton X-100, 500 mM NaCl, 1 mM EDTA, and 50 mM HEPES, pH 7.5), once in wash buffer 3 (250 mM LiCl, 0.5% NP-40, 0.5% deoxycholate, 1 mM EDTA, and 10 mM Tris, pH 8.1), and twice in wash buffer 4 (50 mM Tris, pH 7.4, and 50 mM NaCl). Washes were performed at room temperature for 5 min with gentle agitation. Samples were eluted in Laemmli buffer and boiled at 95° C. Quantification of biotinylation activity was measured as intensity of each lane in the ±biotin immune-precipitation condition divided by the corresponding intensity of the ligase expression band in the input. The +biotin ratios were then normalized to the –biotin control ratio and to background.

### **Quantitative proteomics**

Quantitative mass spectrometry-based proteomics was performed as previously described (Paulo et al., 2015; Biancur et al., 2017) based on the SL-TMT workflow (Navarrete-Perea et al., 2018). In brief, cells were lysed in a lysis buffer (200 mM HEPES

pH 8.5, 8 M urea, 1x Complete Protease Inhibitor Cocktail (Roche), 1 × PhosStop (Roche)) and homogenized by passing through a 21-gauge needle. Lysates were collected by centrifuging at 20,000g for 5 min at 4° C, followed by disulfide bond reduction with 5 mM dithiothreitol at 37° C for 25 min and alkylation with 10 mM iodoacetamide at room temperature for 30 min in the dark. Chloroform–methanol precipitation of protein was performed, followed by protease digestion in HEPES buffer (200 mM, pH 8.5). Each sample containing 100 µg protein was digested at a 1:100 protease-to-protein ratio with LysC protease at room temperature overnight, followed by digestion with trypsin at 37° C for 6 h. Approximately 50 µg of peptides from each sample was labelled with 100 µg TMT reagent which were dissolved in anhydrous acetonitrile to achieve a final concentration of 30% (v/v). TMT-labelled samples were acidified, vacuum centrifuged to near dryness and subjected to C18 SPE (Sep-Pak, Waters). Samples were subjected to basic pH reversed-phase HPLC. Data were obtained with Orbitrap Fusion mass spectrometer (Thermo Fisher Scientific) coupled with a Proxeon EASY-nLC 1000 LC pump (Thermo Fisher Scientific). Peptide separation was done using a custom Accucore C18 resin (2.6 µm, 100 Å, Thermo Fisher Scientific) column for 3 h using a gradient of 6–30% acetonitrile in 0.125% formic acid with a flow rate of 300 nl min<sup>-1</sup>. All analysis involved an MS<sup>3</sup>-based TMT method as previously mentioned (McAlister et al., 2014) and mass spectra were processed as described earlier (Paulo et al., 2015).

### **Flow cytometry**

For surface and intracellular MHC-I staining of human cell lines, cells were stained with Alexa Fluor 488 anti-human HLA-A, -B, -C antibody (BioLegend, clone W6/32) at a 1:75

dilution for 45 min at 4° C in the dark and washed with PBS plus 2% FBS and 2 mM EDTA (FACS buffer). Cells were then fixed and permeabilized before staining with phycoerythrin (PE)-conjugated anti-human HLA-A, -B, -C anti- body (BioLegend, clone W6/32) at a 1:75 dilution for 45 min at room temperature and washed with FACS buffer. For cell-surface molecule staining of mouse cells, single-cell suspensions were prepared as described above. Cells were washed with FCM buffer (HBSS containing 1% FBS, 1 mM EDTA, and 10 mM HEPES) and stained with antibodies (Supplementary Table 1) at 4° C in the dark for 20 min. Dead cells were depleted by DAPI staining.

### **Cell sorting**

Human dCas8902 expressing dCas9-BFP-KRAB fusion proteins driven from the EF-1 $\alpha$  promoter were grown for 5 days following puromycin selection after infection with the whole-genome library. Cells were dissociated with TryLE, stained with an HLA-A, B, C AF488 antibody, fixed with 4% PFA, and sorted on BD LSRFortessa Cell Analyzers. Two cell populations were collected: MHC-I high (top 30%) and MHC-I low (bottom 30%).

### **Quantitative reverse-transcription PCR**

Total RNA was extracted using PureLink RNA Mini Kit (Thermo Fisher Scientific), and then reversed transcribed using Superscript Vilo IV (Thermo Fisher Scientific) with oligo-dT primers. Quantitative PCR was performed with SYBR Green Supermix (Bio-Rad) on the CFX96 real-time PCR machine (Bio-Rad). The quantity of mRNA was calculated using the  $\Delta C_t$  method and normalized by the *GAPDH*, *Actb*, or *36B4* (also known as *Rplp0*) genes for humans or mice, respectively.

## **Immunoblotting**

Cells were lysed in cell lysis buffer (Cell Signaling Technology, 9803) supplemented with protease inhibitor (Thermo Fisher Scientific, A32953) and phosphatase inhibitor (PhosSTOP, Sigma Aldrich, 04906837001). Proteins were separated on 12% or 4–20% Mini-PROTEAN TGX Precast Protein Gels by SDS PAGE electrophoresis and transferred to onto PVDF membranes (IPVH00010, EMD Millipore) or nitrocellulose membranes (GE Healthcare Amersham Protran NC Rolls, Fisher, 10600000). Membranes were blocked in 5% non-fat dry milk (Blotting-Grade Blocker, Bio-Rad, 1706404) dissolved in TBS-T for 1 h and incubated overnight at 4° C with primary antibodies (Supplementary Table 1). Membranes were washed three times with TBS-T and incubated with secondary antibodies for 1 h at room temperature: anti-rabbit IgG, horseradish peroxidase (HRP)-linked (Cell Signaling Technology, 7074), anti-mouse IgG, HRP-linked (Cell Signaling Technology, 7076). Images were obtained by chemiluminescence (Bio-Rad 1705061) using a ChemiDoc (Bio-Rad).

## References

- Alix, E. *et al.* The Tumor Suppressor TMEM127 is a Nedd4-Family E3 Ligase Adaptor Required by *Salmonella* SteD to Ubiquitinate and Degrade MHC Class II Molecules. *Cell Host and Microbe* **28**, 54-68 (2020).
- Bader, G. D. and Hogue, C. W. An automated method for finding molecular complexes in large protein interaction networks. *BMS Bioinformatics* **4**, 2 (2003).
- Baginska, J. *et al.* Granzyme B degradation by autophagy decreases tumor cell susceptibility to natural killer-mediated lysis under hypoxia. *PNAS* **110**(43), 17450-17455 (2013).
- Bartee, E. Downregulation of Major Histocompatibility Complex Class I by Human Ubiquitin Ligases Related to Viral Immune Evasion Proteins. *J of Virology* **78**, 3 (2004).
- Basha, G. *et. al.* MHC Class I endosomal and lysosomal trafficking coincides with exogenous antigen loading in dendritic cells. *PLoS One* **3**, 3 (2008).
- Besson, A., Gurian-West, M., Chen, X., Kelly-Spratt, K.S., Kemp, C.J., and Roberts, J.M. A pathway in quiescent cells that controls p27Kip1 stability, subcellular localization, and tumor suppression. *Genes Dev.* **20**, 47–64 (2006).
- Biederstadt, A. *et al.* SUMO pathway inhibition targets an aggressive pancreatic cancer subtype. *Gut* **69** (8), 1472-1482 (2020).

- Bradley, S. D. BRAFV600E Co-Opts a Conserved MHC Class I Internalization Pathway to Diminish Antigen Presentation and CD8<sup>+</sup> T-cell Recognition of Melanoma. *Cancer Immunol Res.* **3** (6), 602-609 (2015).
- Branon, T. C. et al. Efficient proximity labeling in living cells and organisms with TurboID. *Nat. Biotechnol.* **36**, 880–887 (2018).
- Brea, E. J. et al. Kinase Regulation of Human MHC Class I Molecule Expression on Cancer Cells. *Cancer Immunol Res.* **4** (11), 936-947 (2016).
- Brutkiewicz, R. R. Cell Signaling Pathways That Regulate Antigen Presentation. *J Immunol.* **197** (8), 2971-2979 (2016).
- Burr, M. L. et al. MHC class I molecules are preferentially ubiquitinated on endoplasmic reticulum luminal residues during HRD1 ubiquitin E3 ligase-mediated dislocation. *PNAS.* 2013; **110**, 35: 14290-5.
- Chen, D. et al. Chloroquine modulates antitumor immune response by resetting tumor-associated macrophages toward M1 phenotype. *Nature Communications* **9**, 873 (2018).
- Chen, E. Y. et al. Enrichr: interactive and collaborative HTML5 gene list enrichment analysis tool. *BMC Bioinformatics* **14**, 128 (2013).
- Cruz, F. M. et al. The Biology and Underlying Mechanisms of Cross-Presentation of Exogenous Antigens on MHC-I Molecules. *Annu Rev Immunol.* **35**, 149-176 (2017).



- Deng, X. *et al.* E3 ubiquitin ligase TRIM29 promotes pancreatic cancer growth and progression via stabilizing Yes-associated protein 1. *Journal of Trans. Med.* **19**, 332 (2021).
- DeVorkin, L. *et al.* Autophagy Regulation of Metabolism is Required for CD8<sup>+</sup> T Cell Anti-Tumor Immunity. *Cell Reports* **27**, 502-513 (2019).
- Eyster, C. A. *et al.* MARCH ubiquitin ligases alter the itinerary of clathrin-independent cargo from recycling to degradation. *Mol. Biol. Cell.* (2011).
- Frazier, J. P. *et al.* Multidrug Analyses in Patients Distinguish Efficacious Cancer Agents Based on Both Tumor Cell Killing and Immunomodulation. *Cancer Research* **77**(11), 2869-2880 (2017).
- Gallagher, E., Gao, M., Liu, Y.C., and Karin, M. Activation of the E3 ubiquitin ligase Itch through a phosphorylation-induced conformational change. *Proc. Natl. Acad. Sci. USA* **103**, 1717–1722 (2006).
- Gilbert, L. A. *et al.* CRISPR-mediated modular RNA-guided regulation of transcription in eukaryotes. *Cell* **154**(2), 442-451 (2013).
- Gilbert, L. A. *et al.* Genome-Scale CRISPR-Mediated Control of Gene Repression and Activation. *Cell* **159**(3), 647-661 (2014).
- Guild, B.C. and Strominger, J. L. Human and murine class I MHC antigens share conserved serine 335, the site of HLA phosphorylation in vivo. *J. Biol. Chem.* **259** (14), 9235-40 (1984).

- Han, Z. *et al.* The post-translational modification, SUMOylation, and cancer (Review). *International Journal of Oncology* **52**, 1081-1094 (2018).
- Hendriks, I. A. and Vertegaal, A. C. O. A comprehensive compilation of SUMO proteomics. *Nat. Rev. Mol Cell Biol.* **17** (9): 581-595 (2016).
- Horlbeck, M. A. *et al.* Compact and highly active next-generation libraries for CRISPR-mediated gene repression and activation. *Elife* **5**, e19760 (2016).
- Hu, H. and Sun, S. Ubiquitin signaling in immune responses. *Cell Research* **26**, 457-483 (2016).
- Huang, D. W. *et al.* Systematic and integrative analysis of large gene lists using DAVID Bioinformatics Resources. *Nature Protoc.* **4**(1), 44-57 (2009).
- Humphries, F. *et al.* The E3 ubiquitin ligase Pellino2 mediates priming of the NLRP3 inflammasome. *Nature Communications* **9**, 1560 (2018).
- Jongsma, M. L. M. *et al.* The SPPL3-Defined Glycosphingolipid Repertoire Orchestrates HLA Class I-Mediated Immune Responses **54**(1), 132-150 (2021).
- Karsli-Uzunbas, G. *et al.* Autophagy is Required for Glucose Homeostasis and Lung Tumor Maintenance. *Cancer Discovery* **4**(8) (2014).
- Keshet, R. *et al.* Targeting purine synthesis in ASS1-expressing tumors enhances the response to immune checkpoint inhibitors. *Nature Cancer* **1**, 894-908 (2020).
- Komander, D. & Rape, M. The Ubiquitin Code. *Annu. Rev. Biochem.* **81**, 203–29 (2012).

- Kuleshov, M. V. *et al.* Enrichr: a comprehensive gene set enrichment analysis web server 2016 update. *Nucleic Acids Res.* **44**(W1), W90-97 (2016).
- Kumar, R. *et al.* The STUbL RNF4 regulates protein group SUMOylation by targeting the SUMO conjugation machinery. *Nature Communications* **8**, 1809 (2017).
- Lamsoul, I. *et al.* Exclusive ubiquitination and sumoylation on overlapping lysine residues mediate NF-kappaB activation by the human T-cell leukemia virus tax oncoprotein. *Mol Cell Biol.* **25**(23), 10391-10406 (2005).
- Li, J. *et al.* E3 Ubiquitin Ligase UBR5 Promotes the Metastasis of Pancreatic Cancer via Destabilizing F-Actin Capping Protein CAPZA1. *Frontiers in Oncology* **11**: 634167 (2021).
- Lizee, G. *et al.* Tails of wonder: endocytic-sorting motifs key for exogenous antigen presentation. *Trends Immunol.* **26** (3), 141-149 (2005).
- Loureiro, J. and Ploegh, H. L. Antigen presentation and the ubiquitin-proteasome system in host-pathogen interactions. *Adv Immunol.* **92**, 225-305 (2006).
- Machy, P. *et al.* Major histocompatibility complex class I molecules internalized via coated pits in T lymphocytes. *Nature* **328** (6132): 724-6 (1987).
- Mastelic-Gavillet, B. *et al.* Adenosine mediates functional and metabolic suppression of peripheral and tumor-infiltrating CD8<sup>+</sup> T cells. *J Immunother. Cancer* **7**(1), 257 (2019).

- Nakayama, K.I., and Nakayama, K. Ubiquitin ligases: cell-cycle control and cancer. *Nat. Rev. Cancer* **6**, 369–381 (2006).
- Nathan, J. A. & Lehner, P. J. The trafficking and regulation of membrane receptors by the RING-CH ubiquitin E3 ligases. *Exp. Cell Res.* **315**, 1593–1600 (2008).
- Noman, M. Z. *et al.* PD-L1 is a novel direct target of HIF-1alpha, and its blockade under hypoxia enhanced MDSC-mediated T cell activation. *J. Exp. Med.* **211**, 781-790 (2014).
- Pandha, H., Rigg, A., John, J. & Lemoine, N. Loss of expression of antigen-presenting molecules in human pancreatic cancer and pancreatic cancer cell lines. *Clin Exp Immunol.* **148**, 127-135 (2007).
- Paulsson, K. M. *et al.* Association of tapasin and COPI provides a mechanism for the retrograde transport of major histocompatibility complex (MHC) class I molecules from the Golgi complex to the endoplasmic reticulum. *J Biol. Chem.* **277** (21), 18266-71 (2002).
- Pommier, A. *et al.* Unresolved endoplasmic reticulum stress engenders immune-resistant, latent pancreatic cancer metastases. *Science* **360**, 6394 (2018).
- Rogers, S., Wells, R., and Rechsteiner, M. Amino acid sequences common to rapidly degraded proteins: the PEST hypothesis. *Science* **234**, 364–368 (1986).
- Sala-Gaston, J. HERC Ubiquitin Ligases in Cancer. *Cancers (Basel)*. **12** (6), 1653 (2020).

- Santos, S. G. Misfolding of major histocompatibility complex class I molecules in activated T cells allows cis-interactions with receptors and signaling molecules and is associated with tyrosine phosphorylation. *J. Biol. Chem.* **279** (51), 53062-70 (2004).
- Sharma, B. S. et al. Post-translational Modifications (PTMs), from a Cancer Perspective: An Overview. *Oncogene* **2**, 3 (2019).
- Shin, J. et al. Surface expression of MHC class II in dendritic cells is controlled by regulated ubiquitination. *Nature*. **444**, 115–118 (2006).
- Singh, S. et al. Increased expression of MARCH8, an E3 ubiquitin ligase, is associated with growth of esophageal tumor. *Cancer Cell Int.* **17**: 116 (2017).
- Visser Smit, G. D. et al. Cbl controls EGFR fate by regulating early endosome fusion. *Sci Signal.* **2**, 102 (2009).
- Wang, Y. et al. Oncoprotein SND1 hijacks nascent MHC-I heavy chain to ER-associated degradation, leading to impaired CD8<sup>+</sup> T cell response in tumor. *Science Advances* **6**, 22 (2020).
- Wang, Z. et al. Activation of CXCR4 Triggers Ubiquitination and Down-regulation of Major Histocompatibility Complex Class I (MHC-I) on Epithelioid Carcinoma HeLa Cells. *J. Biol. Chem.* **283**, 3951–3959 (2008).
- Wei, J. et al. Autophagy enforces functional integrity of regulatory T cells by coupling environmental cues and metabolic homeostasis. **17**(3), 277-285 (2016).

- Wei, W. and Lin H. The key role of ubiquitination and sumoylation in signaling and cancer: a research topic. *Front. Oncol.* **2**, 187 (2012).
- Wood, A., Schneider, J., Dover, J., Johnston, M., and Shilatifard, A. The Bur1/Bur2 complex is required for histone H2B monoubiquitination by Rad6/Bre1 and histone methylation by COMPASS. *Mol. Cell* **20**, 589–599 (2005).
- Xu, Y. A miRNA-HERC4 pathway promotes breast tumorigenesis by inactivating tumor suppressor LATS1. *Protein Cell* **10** (8), 595-605 (2019).
- Yamamoto, K., Venida, A., Yano, J., Biancur, D.E., Kakichu, M., Gupta, S., Sohn, A. S. W., Mukhopadhyay, S., Lin, E. Y., Parker, S. J., Banh, R. S., Paulo, J. A., Wen, K., Debnath, J., Kim, G. E., Mancias, J. D., Fearon, D. T., Perera, R. M., Kimmelman, A. C. Autophagy promotes immune evasion of pancreatic cancer by degrading MHC-I. *Nature* **581**, 100-105 (2020).
- Yang, A. *et al.* Autophagy Sustains Pancreatic Cancer Growth through Both Cell-Autonomous and Nonautonomous Mechanisms. *Cancer Discovery* **8**(3), 276-287 (2018).
- Zamaraev, A. V. *et al.* Post-translational Modification of Caspases: The Other Side of Apoptosis Regulation. *Trends in Cell Biology* **27**, 322-339 (2017).
- Zerial, M. and McBride, H. Rab proteins as membrane organizers. *Nat. Rev. Mol. Cell Biol.* **2** (2), 107-17 (2001).

- Zhang, Q. *et al.* RNF13: a novel RING-type ubiquitin ligase over-expressed in pancreatic cancer. **19**, 348-357 (2009).
- Zheng, W. *et al.* Crosstalk of intracellular post-translational modifications in cancer. *Arch. Biochem. Biophys.* **676**, 108-138 (2019).
- Zheng, Y. *et al.* HERC4 is Overexpressed in Hepatocellular Carcinoma and Contributes to the Proliferation and Migration of Hepatocellular Carcinoma Cells. *DNA and Cell Biology* **36**, 6 (2017).
- Zhou, H. The expression and clinical significance of HERC4 in breast cancer. *Cancer Cell International* **13**, 113 (2013).
- Zou, L. *et al.* The GTPase Rab3b/3c-positive recycling vesicles are involved in cross-presentation in dendritic cells. *PNAS* **106** (37), 15801-15806 (2009).

## Publishing Agreement

It is the policy of the University to encourage open access and broad distribution of all theses, dissertations, and manuscripts. The Graduate Division will facilitate the distribution of UCSF theses, dissertations, and manuscripts to the UCSF Library for open access and distribution. UCSF will make such theses, dissertations, and manuscripts accessible to the public and will take reasonable steps to preserve these works in perpetuity.

I hereby grant the non-exclusive, perpetual right to The Regents of the University of California to reproduce, publicly display, distribute, preserve, and publish copies of my thesis, dissertation, or manuscript in any form or media, now existing or later derived, including access online for teaching, research, and public service purposes.

DocuSigned by:

*Anthony Venida*

E4DCF67F899942C...

Author Signature

12/2/2021

Date